HIGH RESOLUTION STRATIGRAPHY OF THE LOWER SILURIAN (RHUDDANIAN-AERONIAN) PALEOTROPICAL NERITIC CARBONATES, ANTICOSTI ISLAND, QUÉBEC

Pascale Daoust

Thesis submitted to the
Faculty of Graduate and Postdoctoral Studies
in partial fulfillment of the requirements
for the Master's degree in Earth Sciences

Ottawa-Carleton Geoscience Centre
Department of Earth and Environmental Sciences
Faculty of Science
University of Ottawa

Résumé

L'île d'Anticosti située dans l'est du Canada contient une des successions carbonatées des plus complètes, mieux exposées et plus fossilifères au monde à la frontière Ordovicien-Silurien. La présente étude a développé un cadre stratigraphique de haute résolution de strates (~ 260 m en épaisseur) postdatant l'extinction de masse de la fin de l'Ordovicien à partir d'affleurements côtiers et d'un forage (La Loutre #1) dans la partie ouest de l'île. En tout, huit faciès associés à un système carbonaté néritique dominé par les tempêtes, ont été identifiés et organisés en cycles sédimentaires multi-ordres. Une nouvelle courbe isotopique de haute résolution a été construite avec plus de 300 points provenant de la micrite bien préservée s'étalant de la fin de l'Hirnantien au début de l'Aéronien. Cette période de temps correspond aux formations d'Ellis Bay, Becscie, Merrimack et Gun River. Deux excursions isotopiques positives en carbone sont présentes; la première dans la partie de l'Hirnantien tardif de la Formation d'Ellis Bay (+5‰) et la deuxième dans la partie inférieure de la Formation de Gun River au début de l'Aéronien (+2‰). Ces excursions positives fournissent une signature chemostratigraphique distincte nous permettant d'établir des corrélations régionales et mondiales avec d'autres coupes du même âge. Tout comme le signal en $\delta^{18}O$ du Quaternaire, notre signal $\delta^{18}O$ est associé à des changements paléobathymétriques définis par des cycles de faciès à plusieurs ordres. Notre étude démontre l'importance de la glacio-eustasie même après le maximum glaciaire de la fin de l'Ordovicien comme un important facteur pouvant contrôler l'architecture stratigraphique de carbonates néritiques de milieu tropical au début du Silurien.

Abstract

Anticosti Island, located in Eastern Canada, displays one of the most complete, best exposed, and most fossiliferous carbonate successions spanning the Ordovician-Silurian (O/S) Boundary in the World. This study develops a new high-resolution framework for the post End-Ordovician extinction strata (~ 260 m thick) exposed in coastal outcrops and recovered from a continuous drill core (La Loutre #1), both located in the western part of the island. In total, eight facies, all associated with a storm-dominated carbonate system, were recognized and organized into a multi-order depositional cycles. A new high resolution isotopic curve with more than 300 data points from well-preserved bulk micrite samples covers the late Hirnantian to Early Aeronian time interval and corresponds to the upper Ellis Bay, Becscie, Merrimack and lower Gun River formations. Two distinct positive carbon isotope excursions are present in the late Hirnantian part of the Ellis Bay Formation (+5‰) and in the lower Aeronian part of the Gun River Formation (+2‰). These positive isotopic carbon excursions provide a distinctive chemostratigraphic signature for regional and global correlations with other O/S sections. Like the Quaternary $\delta^{18}O$ marine signal, our $\delta^{18}O$ record is largely coupled with multi-order cyclic facies changes. This study demonstrates the importance of glacio-eustasy following the End-Ordovician glacial maxima as one of the primary factors controlling the stratigraphic architecture of paleotropical neritic carbonates during the Early Silurian.

Acknowledgments

This project and thesis were a huge success because of many reasons and people. My supervisor Dr. André Desrochers was a milestone and help throughout my bachelor and master's thesis with his academic and financial support. I am more than grateful for all opportunities and experiences he provided. He was always there from my bachelor's degree to now helping and providing advice. I would like to thank the Natural Sciences and Engineering Research Council of Canada (NSERC Discovery Grant to AD) and the Ontario Graduate Scholarship (OGS) for providing the funding for this project. I would also like to thank all the residents from Anticosti Island that helped us in many ways during the field seasons. Furthermore, many thanks to Mathias Sinnesael, Marili Vincent-Couture and Steven DeDecker in helping with the sampling both in the field and the core library in Québec City. Special thanks to the ministère de l'énergie et des ressources naturelles du Québec for providing acess to La Loutre#1 core. I would also like to show my appreciation to the department lab technicians, Alain Mauviel and George Mrazek for making my thin sections. I would like to acknowledge all the support from Paul Middlestead, Wendi Abdi and Patricia Wickham at the G.G. Hatch Laboratory at the University of Ottawa and Nimal DeSilva at the uOttawa trace element geochemistry laboratory.

Lastly, beyond recognition, I would like to thank André Desrochers, my mother Brigitte, my best friend Anne Chu and my sister Stéphanie for helping with the figures and the correction of my text. Finally, a distinctive thank to my family especially my grandfather who started my passion for science; Marc-Aurèle and friends for their support throughout this project.

Table of content

List of Figures

List of Tables

List of Appendices

1. Introduction

Following the Cambrian explosion, the Ordovician and Silurian periods were marked by three major biotic events: the Great Ordovician Biodiversification Event (GOBE), the End-Ordovician extinction (the first animal extinction and the second largest of the five large-scale mass extinctions of the Phanerozoic), and the Early Silurian post-extinction recovery (Munnecke et al., 2010; Melchin et al. 2012). Apart from the recovery in biodiversity after the end-Ordovician, the Silurian witnessed a highly dynamic climate accentuated by multiple short-lived events, and strong sea level fluctuations and oceanic turnovers, associated with extinctions of moderate scale (Melchin et al., 2012). General convergence of plate tectonic plates and low levels faunal provincialism, closure of Iapetus Ocean, narrowing of the Rheic Ocean and migration of Gondwana over the South Pole also occurred during the Silurian (Scotese, 2014). In the past decades, several authors helped define much more dynamic Silurian Earth Systems than previously thought (Munnecke et al., 2003; Cramer and Saltzman, 2005; Melchin and Holmden, 2006; Calner, 2008; Munnecke and al., 2010; Ogg et al., 2016). These dynamic changes associated with the ocean-atmosphere system were partly expressed by several major positive carbon isotopic excursions throughout the Silurian in association with moderate biotic turnovers that occurred just prior to and/or during the onset of those positive excursions (Cramer et al., 2011; Munnecke et al., 2010). The relationship between the carbon isotopic record and Silurian biotic and global climate events, however, remains a highly contentious issue (Loydell, 2007; Cramer et al., 2011; Munnecke et al., 2010; Melchin et al, 2012). On the other hand, carbon isotope chemostratigraphy can be used as a purely stratigraphic tool. The Silurian carbon isotopic record is the most highly resolved of any period of the Paleozoic with three significant positive excursions during the Lower Silurian (i.e. the early and late Aeronian, and early Telychian excursions; see Cramer et al., 2011 and references therein). These carbon positive excursions are often reported from deep water strata and measured in organic carbon ($\delta^{13}C_{org}$) rather than neritic carbonate facies ($\delta^{13}C_{carb}$) but remain an invaluable tool for establishing global correlations.

The upper 900 m of the >2 km thick Sandbian to Telychian succession in the Anticosti Basin constitutes a comprehensive Upper Ordovician to Lower Silurian record superbly exposed on Anticosti Island in the Gulf of St-Lawrence (Fig.1.1; Long, 2007; Desrochers et al., 2010). In this study, we will focus on the Upper Hirnantian to Lower Aeronian strata both exposed in coastal exposures in the western part of the island and recovered from a recent stratigraphic drill core. This corresponds to the time interval characterized by a rapid recovery in biodiversity after the end-Ordovician mass extinction. The main objectives of this study are to test the presence of the positive carbon, and likely oxygen, excursions in paleotropical neritic carbonate facies for potential global correlations and to establish an integrated high resolution stratigraphic framework incorporating biostratigraphy, carbonate sedimentology, multi-order cyclostratigraphy and chemostratigraphy and for the recognition of stratigraphic signatures left by the dynamic Earth Systems during the Early Silurian.

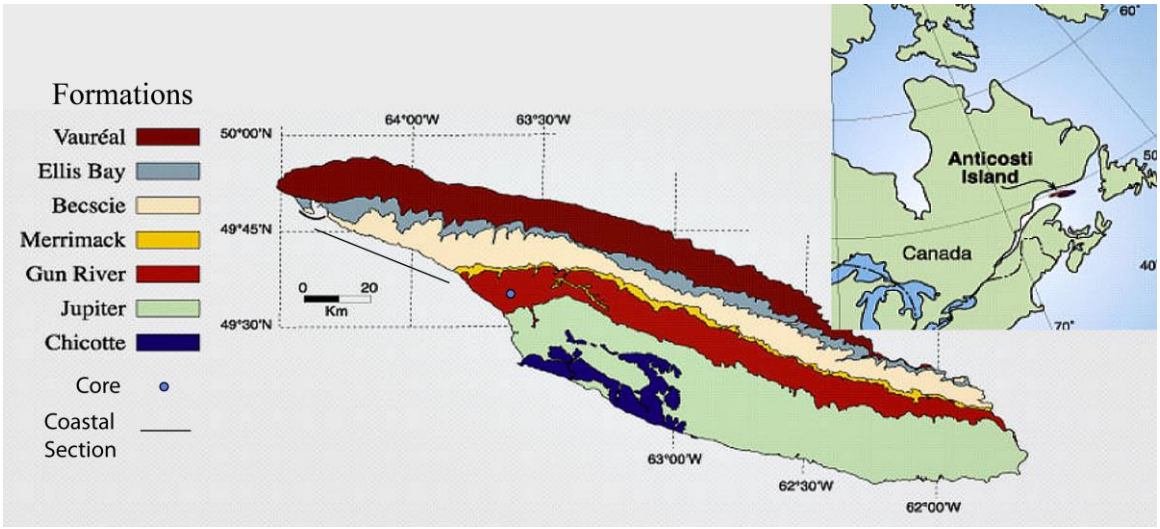

Figure 1.1.Geological map of Anticosti Island, Québec showing the location of La Loutre #1 core and the studied coastal outcrops in the western part of the island (Modified from Desrochers and Gauthier, 2009).

2. Geological Setting

Anticosti Island is located in the Gulf of the St-Lawrence in Eastern Canada (Fig. 1.1). The undeformed, fossiliferous and well exposed succession of Anticosti Island is one of the most complete records spanning the Ordovician-Silurian (O-S) boundary in the world (Achab et al., 2012; Ghienne et al., 2014). The Anticosti succession comprises

mostly storm-deposited sediments deposited on a shallow epeiric carbonate ramp (Long, 2007; Desrochers et al., 2010).

The lower Paleozoic Anticosti Basin formed into three distinct phases: i) a rifting phase, ii) a passive margin phase and iii) a foreland basin phase. Prior to the fragmentation of the Rodinia supercontinent, the study area was located along the eastern margin of Laurentia south of the paleo-equator (Fig. 2.1; Cocks and Torsvik, 2004; Jin et al. 2013). The Anticosti Basin formed after the fragmentation of Rodinia in the Neoproterozoic-Early Cambrian and subsequent development of a passive margin along the eastern seaboard of Laurentia (Allen et al., 2009; Desrochers et al., 2010; Pinet et al., 2012). From the Cambrian to Early Ordovician, the passive margin phase allowed the deposition of extensive shallow water carbonates in the Anticosti Basin (Lavoie et al., 2003; Desrochers et al., 2013). This phase ended by the development of a vast karstic peneplain over the subaerially exposed passive margin carbonates during the Middle Ordovician (Desrochers and James, 1988). This subaerial surface, recognized as the Sauk-Tippecanoe megasequence boundary in the cratonic interior of Laurentia (Sloss, 1963), recorded not only a major sea level fall but also the incipient tectonic movements associated with the early development of the Appalachian foreland basin further east (Lavoie, 2008; Pinet et al. 2012). The Anticosti Basin finally shifted to an active foreland basin during the initial emplacement of the Taconic thrusts in the Middle Ordovician that caused high subsidence rates along the eastern part of Laurentia ((Lavoie, 2008; Pinet et al. 2012). In our study area located in the distal foreland basin, the rates of tectonic subsidence peaked during the Katian at 17.9 cm/ka, subsequently slowed down at about 1 cm/ka during the Hirnantian-Rhuddanian time and finally reactivated at 3.0 cm/ka during the Aeronian (Long, 2007).

The lithostratigraphy of the Anticosti succession (Fig. 2.2) was recently revised including: the Hirnantian Ellis Bay Formation (Copper et al., 2013), the Rhuddanian Becscie and Merrimack formations (Copper and Jin, 2014), and the Aeronian Gun River Formation (Copper and al., 2012). Other recently studied formations include the Aeronian-Telychian Jupiter Formation (Copper and Jin, 2015) and the mid Telychian Chicotte Formation (Desrochers, 2006; James et al., 2015). The older Katian Vauréal Formation is

not yet resolved at the same level of confidence (Long and Copper, 1987). The Anticosti succession forms a depositional gradient across the Island from East to West. Relatively thin, mixed siliciclastic-carbonate units separated by stratigraphic discontinuities at the east end of the island accumulated at the basin margin while more complete thicker storm-dominated carbonate facies at the west end of the island accumulated at the basin centre (Desrochers et al., 2010). This succession is substantially thicker (Sandbian to Katian= ~1600 m, Hirnantian= ~100 m, Rhuddanian to mid-Telychian= ~500 m) when compared to other age-equivalent carbonate shallow water successions either on Laurentia or in other paleocontinents (Ghienne et al., 2014). Integrated high resolution stratigraphy studies have recently examined parts of the Anticosti succession (Desrochers et al., 2010, Desrochers and Jin, 2015; Ghienne et al., 2014; Mauviel, 2016; Mauviel and Desrochers, 2016). These studies integrate chitinozoan biostratigraphy, facies analysis, cyclostratigraphy and $\delta^{13}C$ and $\delta^{18}O$ chemostratigraphy. These latter chemostratigraphic studies demonstrated that both $\delta^{13}C$ and $\delta^{18}O$ signals are largely preserved in the strata spanning the O/S Boundary at the west end of Anticosti Island (Ghienne et al., 2015; Mauviel, 2016; Mauviel and Desrochers, 2014). The $\delta^{13}C$ curve with two distinctive Hirnantian positive excursions provides a signature for regional and global correlations while the Hirnantian $\delta^{18}O$ curve resembles the Pleistocene $\delta^{18}O$ curve largely forced by glacioeustatic fluctuations.

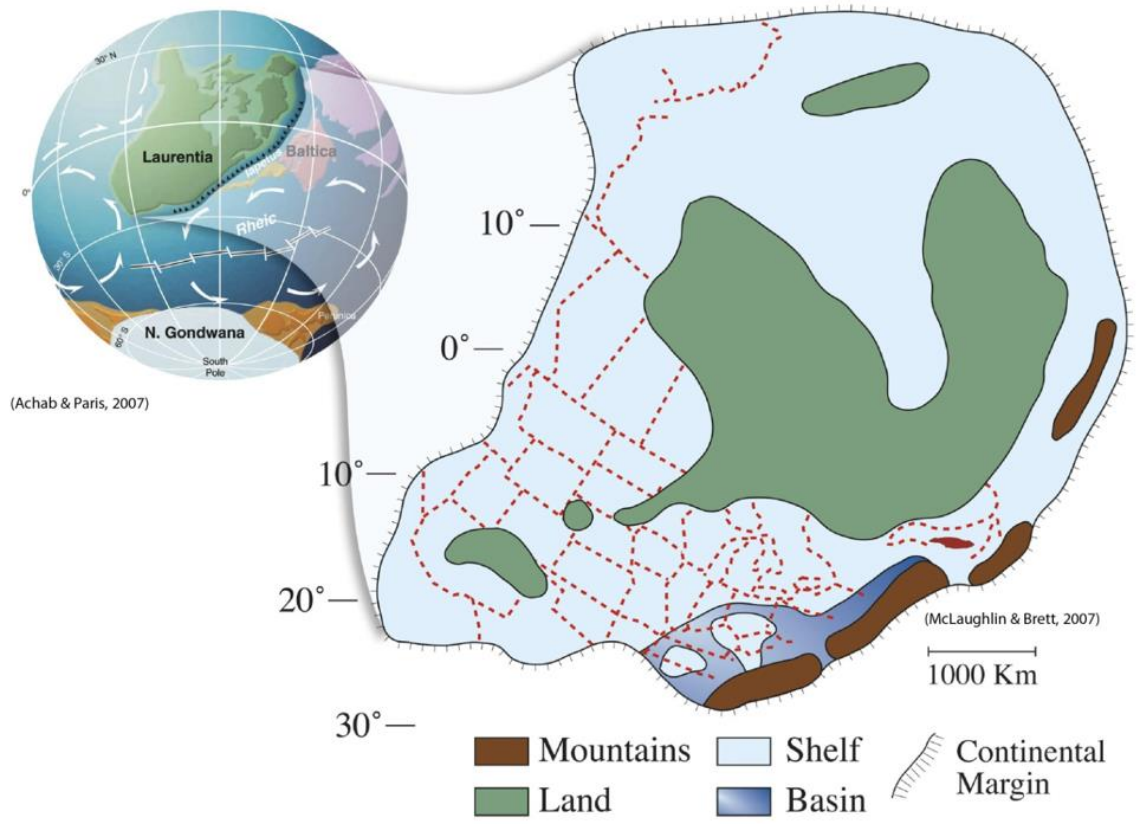

Figure 2.1.Regional and global paleogeographic maps showing the location of Anticosti Island during the end Ordovician (modified from Achab and Paris 2007, McLaughlin and Brett 2007).

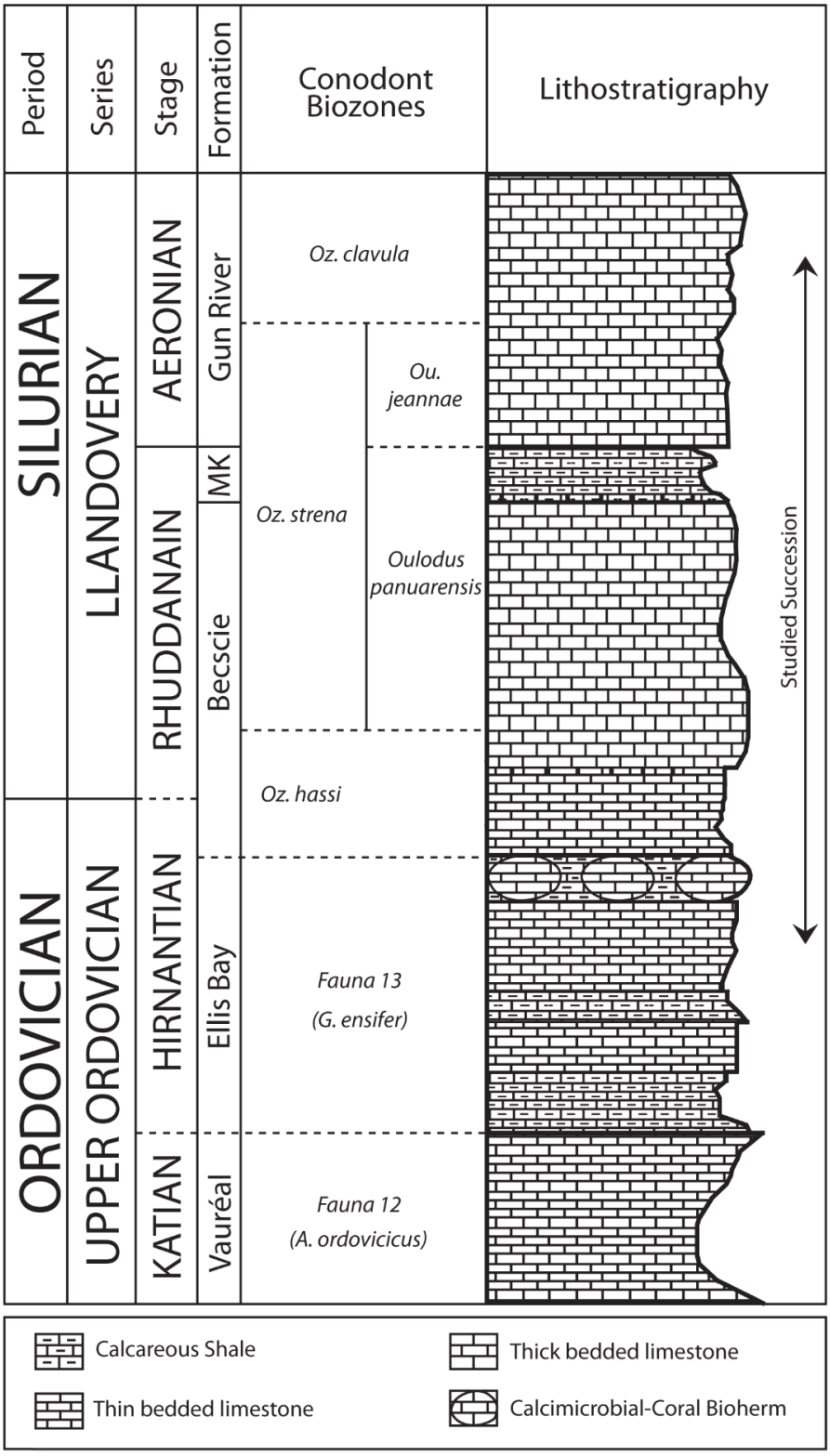

Figure 2.2. Generalized stratigraphic column of the studied Anticosti succession; MK = Merrimack. Conodont biozones are from Zhang and Barnes, 2004.

3. Biostratigraphy and age of the studied formations

The stratigraphic succession exposed on Anticosti Island, in the Gulf of St Lawrence, contains strata ranging in age from the late Katian and Hirnantian (Late Ordovician) to the mid-Telychian (Llandovery, Early Silurian). The age of the studied formations (Fig. 2.2), here, is mainly constrained by conodonts (Zhang and Barnes, 2002) and chitinozoans (Soufiane and Achab, 2000; Achab et al., 2011; Achab et al., 2013). Shelly fauna (brachiopods and corals) are also useful for establishing temporal correlations with Llandovery shelly fauna described from other paleocontinents (Copper and Long, 1989; Copper et al., 2012; Copper et al., 2013; Copper and Jin, 2014). Graptolites, a key early Paleozoic fossil index, are only sparsely distributed in the studied succession; thus, have a limited use (Melchin, 2008).

The Ellis Bay Formation and basal beds of the Becscie Formation are Hirnantian in age (Achab et al., 2013; Copper et al, 2013; Ghienne et al., 2014). The rest of the Becscie Formation is early Rhuddanian (Copper and Jin, 2014) while the Merrimack is late Rhuddanian (Copper and Long, 1989). The Gun River Formation is early Aeronian in age (Copper et al., 2012). The chitinozoans recovered from the Gun River Formation were originally assigned to a late Rhuddanian age (Soufiane and Achab, 2000, Fig. 7) but recent stratigraphic studies (Copper and Jin, 2014; Copper et al., 2012) clearly demonstrated that these strata belong to the upper Becscie and Merrimack formations and are not in conflict with the Aeronian age assigned by conodonts to the Gun River Formation (Zhang and Barnes, 2002).

4. Methods

This study combines both field data at the west end of the Island and subsurface data from a recent stratigraphic drill core (La Loutre #1) (Fig. 2.1). Several field and laboratory techniques were used for this project: i) lithological and petrographic observations, ii) cyclostratigraphic analysis, iii) stable isotope chemostratigraphy, iv) trace element geochemistry and v) cathodoluminescence microscopy.

i) Depositional facies were identified in terms of composition, depositional textures and fabrics, sedimentary structures and levels of bioturbation. The field observations were collected at the Baie des Nabots, Baie des Sarcelles, and at the mouth of the Rivière Becscie. The subsurface observations were collected along a ~300 m long core interval that corresponds to the Upper Ellis Bay, Becscie, Merrimack, and Lower Gun River formations. In total, 125 representative samples were selected from both field and subsurface material for more detailed description. 34 large and 6 small thin sections were prepared and stained with Alizarin Red S and Potassium Ferrycianide (Dickson, 1966) for observations under an Olympus BX41 microscope.

ii) The studied succession was subdivided into metre-scale Transgressive/Regressive (TR) cycles (*sensu* Embry, 2009) using various erosion and deposition surfaces or zones (maximum flooding and regressive surfaces or zones) present in the field or in the core. The metre-scale TR cycles locally display more important facies shifts that can be used to delimit lower order TR cycles at the multi-metre to decametre scale.

iii) We used a "bulk-rock" sampling in order to produce a high-resolution, continuous isotopic stratigraphic record that is not dependent on the distribution of brachiopods in the section. In total, 295 samples were collected with a micro-drill from the core material for $\delta^{13}C$ and $\delta^{18}O$ analyses over a 275 m thick interval comprising the upper Ellis Bay (88 m), Becscie (141 m), Merrimack (20 m) and Lower Gun River (65 m) formations. The finest available micritic (occasionally peloidal) material from each hand sample was microdrilled for $\delta^{13}C$ and $\delta^{18}O$ geochemical analyses. Every sample was taken ~1 m apart except in the Laframboise Member of the Ellis Bay Formation which was sampled at every ~0.5 m. The analyses were performed on a Thermo Finnigan Delta XP mass spectrometer with an analytical precision of +/−0.1 ‰ on a Gas Bench II at the G.G. Hatch Laboratory at the University of Ottawa. The results are given in permil (‰) in respect to the Vienna Pee Dee Belemnite, or VPDB standard.

iv) A subset of 30 samples from the different studied stratigraphic units were selected and analyzed for trace element geochemistry in order to evaluate possible diagenetic

modification of the primary marine isotope signal. The analyses were performed on a Varian (Agilent) Vista-Pro Inductively Coupled Plasma Emission Spectrometer (ICP-ES) that has a CCD detector at the General Geochemistry Laboratory, University of Ottawa. The results are given in parts per million (ppm). The detection limit is 0.016 ppm for Mn and 0.034 ppm for Sr.

v) A subset of 6 muddy limestone samples containing brachiopods were examined under cathodoluminescence (CL) microscopy to evaluate possible diagenetic alteration.

5. Results

An integrated stratigraphic analysis of the Ellis Bay-Gun River succession in both surface and subsurface of the Anticosti Island is presented below. First, the major depositional facies in the studied succession are briefly described and interpreted. Second, the complex, but repetitive nature of these facies is examined to decipher their stratigraphic architecture. Third, new high-resolution carbon and oxygen stable isotope curves are presented at the end of this section.

5.1 Facies Description and Interpretation

Numerous portions of the coastal cliff sections exposed at the west end of Anticosti Island have been previously described (Sami and Desrochers, 1992; Long, 2007; Farley, 2008; Desrochers et al. 2010, Jones et al., 2011; Copper et al. 2013; Copper and Jin 2014; Ghienne et al., 2014; Mauviel, 2016). We revisited the facies description of those previous studies, made additional observations, and more importantly included the subsurface material recovered from La Loutre #1 drill core. A summary of our facies description and environmental interpretation is compiled in **table 1 (see below)**. The facies distribution in the studied succession is shown in Fig. 5.13 (see below). We identified, in total, eight depositional facies (facies 1 to 8; Figs. 5.1 to 5.12) representing sediments that were deposited under the influence of episodic storm events below the fair-weather wave base on a mid to outer carbonate ramp depositional system (Aigner, 1985). Episodic storm deposition is evidenced by

the calcisiltite/calcarenite beds with abundant hummocky and swaley cross-stratification (HCS and SWS) with sharp, locally scoured, basal contact. HCS and SWS form under oscillatory-dominated combined flow during storms (Dumas and Arnott, 2006). The storm beds, called here tempestites, are typically lenticular and interbedded with muddy, bioturbated fair-weather deposits (Facies 1 to 3, 7 and 8). Distinctive calcarenite with wave-ripple laminations (Facies 4) and oncolitic calcirudites (Facies 5) locally overlain metazoan-calcimicrobial bioherms (Facies 6) at the top of the Ellis Bay Formation are, however, shallower inner ramp facies deposited above the fair water wave base. Two notable regional discontinuities are present below and above those oncolitic and reefal Laframboise limestones (Desrochers et al. 2010). The biotic assemblage present in all facies is diverse and dominated by open marine stenohaline taxa including (i.e. brachiopods, bryozoans, corals, stromatoporoids, crinoids, etc.).

Facies 1: Nodular mudstone-wackestone (calcilutite)

Facies 1 is a thinly bedded nodular bioturbated muddy limestone (typically mudstone to wackestone) or calcilutite either divided by anastamosed argillaceous solutions seams or interbedded with dark grey cm-thick fissile shale (Figs. 5.1A to 5.1F; table 1). This facies consists of a dense lime with minor skeletal debris and silt-sized angular quartz particles. The main skeletal debris are crinoids, brachiopods, bryozoans and corals. Non-ferroan sparry calcite cement is locally filling burrows and early burial fractures in nodules (Figs. 5.1A and 5.1G). Hardgrounds are locally present (Fig. 5.1C). This facies is usually interbedded with Facies 2 and 3. Facies 1 represents ~25% in thickness of the entire studied succession (Fig. 5.13) but shale interbeds are only present in the Merrimack (Fig. 5.2) and Lower Gun River portions of the studied succession.

Facies 1 represents fine-grained sediments that were deposited below the storm wave base where the seafloor was rarely affected by storms. They could be considered basinal "tempestites" because the lime mud was delivered down-ramp during episodic storm events. The associated fauna is clearly stenohaline supporting an open marine setting. During the Merrimack time, the fair weather siliciclastic influx significantly increased likely in response to more humid climatic conditions in the adjacent landmasses.

Figure 5.1(next page). Facies 1- Polished slabs of the La Loutre #1 core and thin-section photomicrographs. (A) Polished core slab showing the typical nodular muddy limestone beds separated by argillaceous solution seams; crinoidal material (Cr) and early burial fracture are identified. (B) Polished core slab displaying the bioturbated nature of facies 1. (C) Core sample illustrating the presence of iron-stained hardground. (D and E) Photomicrographs showing a sharp basal contact between cm-scale shale bed and the muddy matrix with a small amount of skeletal debris; brachiopods (Bra) and crinoids and quartz particles. (F) Photomicrograph displaying non-ferroan calcite cement filling burrows with a few skeletal debris scattered in the mud. (G) Photomicrograph displaying non-ferroan calcite cement filling burrows and the mud in the nodules.

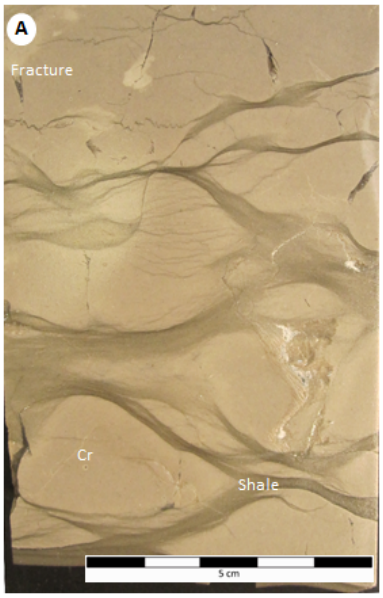
A
Fracture
Cr
Shale
5 cm


B
Coral
Bioturbation
5 cm

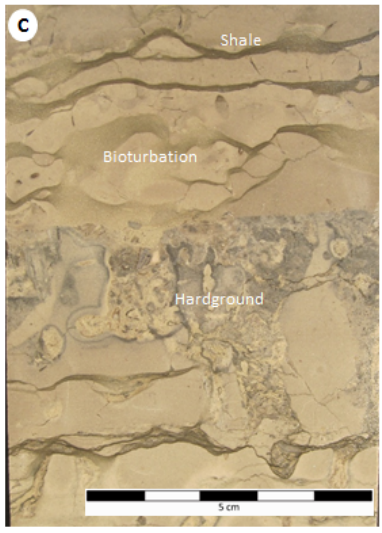
C
Shale
Bioturbation
Hardground
5 cm

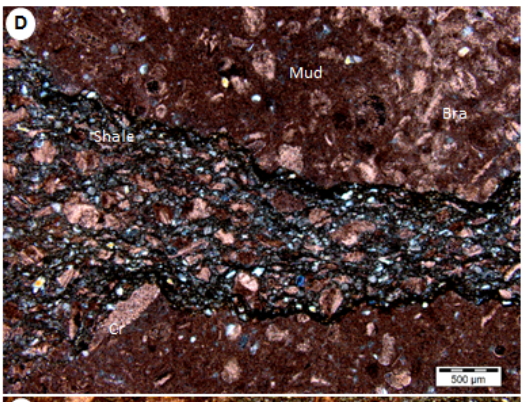
D
Mud
Bra
Shale
Cr
500 µm

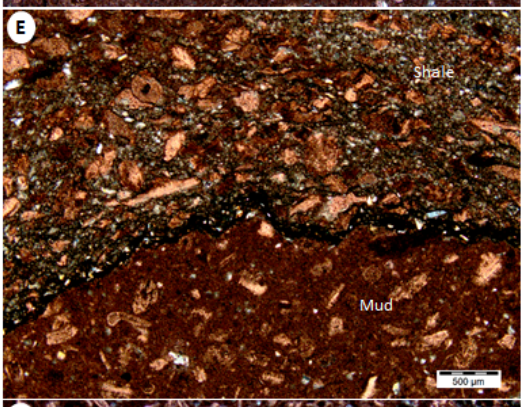
E
Shale
Mud
500 µm

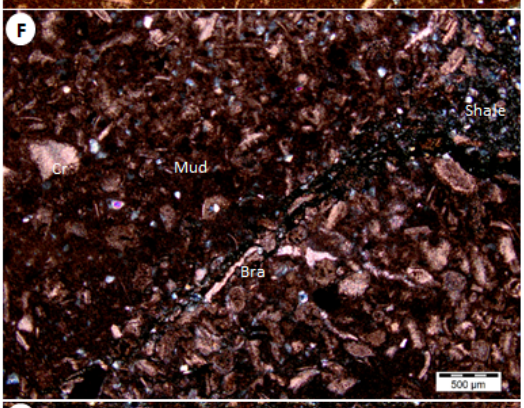
F
Shale
Cr
Mud
Bra
500 µm

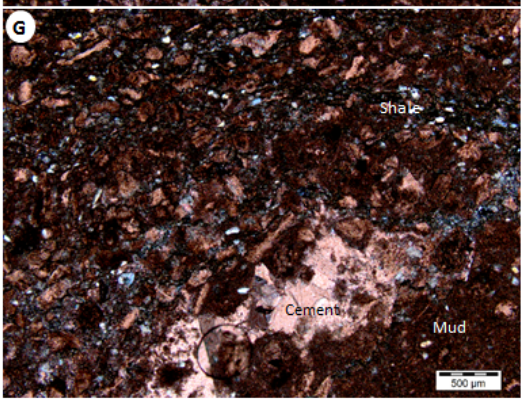
G
Shale
Cement
Mud
500 µm

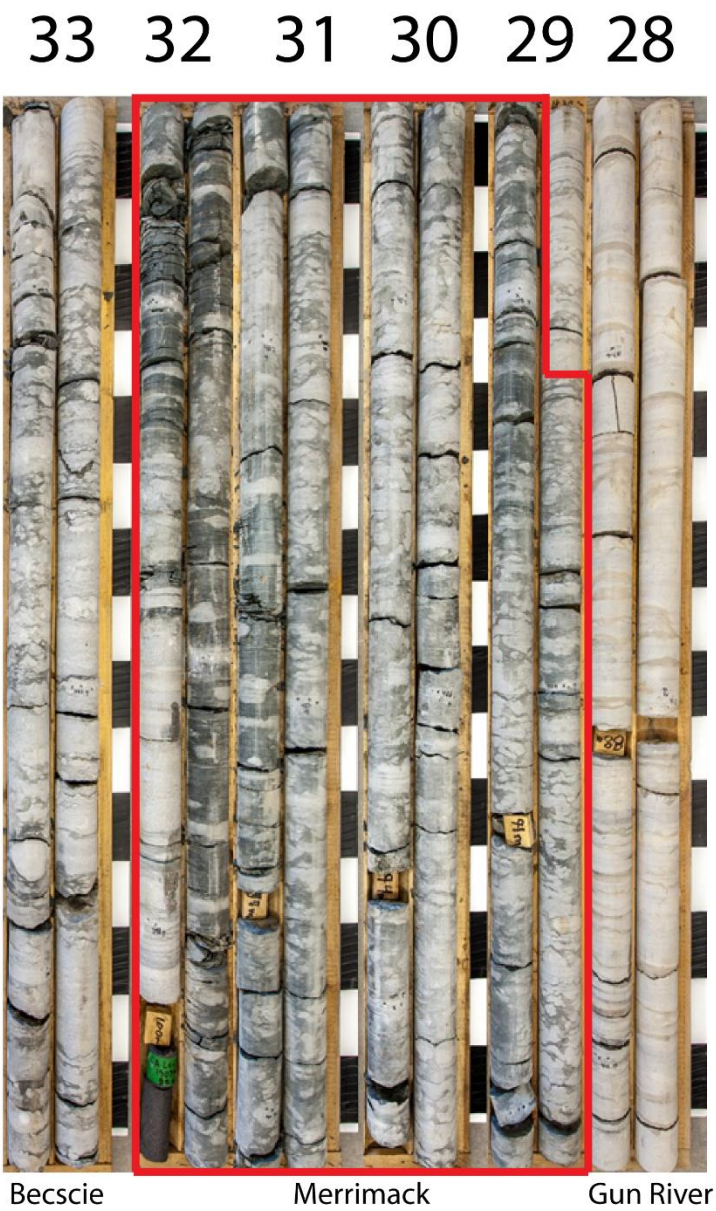

Figure 5.2. Core photograph showing La Loutre #1 boxes # 33 to 28. The Merrimack Formation identified by the red rectangle displays thicker shale interbeds when compared to the underlying Becscie or overlying Gun River formations.

Facies 2: Bioclastic wackestone to packstone

This facies comprises thinly bedded limestone with grey shale interbeds (Fig. 5.3; table 1). The limestone is mainly a bioclastic wackestone to packstone with floating fined-grained angular quartz particles (Fig. 5.3). Individual bed displays a sharp basal contact, a thin graded bioclastic base overlain by a faintly laminated to massive lime mud, and a weakly bioturbated top (Figs. 5.3B, 5.3C and 5.3F). Peloidal grainstone intraclasts are

locally present above the basal scoured surface. Non-ferroan calcite cement is filling original intra-particulate voids, and early burial fractures (Figs. 5.3C, 5.3E and 5.3G). The skeletal debris include brachiopods, crinoids, bivalves, ostracods and trilobites (Figs 5.3A, 5.3C, 5.3D, 5.3E and 5.3F). This facies is typically interbedded with Facies 1 and 3. Facies 2 represents ~20% in thickness of the entire studied succession and is present in all studied formations (Fig. 5.13).

Facies 2 represents fine-to medium-grained storm sediments that formed below the fair-weather wave base but above the storm wave base on distal mid ramp setting. The material was supplied from material that were transported down the ramp during episodic storm events under combined flow regime (Dumas and Arnott, 2006). The diverse stenohaline taxa is clearly indicative of an open marine setting.

Figure 5.3 (next page). Facies 2 - Polished slabs of the La Loutre #1 core and thin-section photomicrographs. (A) Polished core slab showing the presence of peloidal grainstone intraclasts (likely derived from the HCS facies) and skeletal debris (brachiopods and crinoids) within the muddy bioclastic matrix. (B) Polished core slab with abundant bioturbation resulting into a more nodular appearance. (C) Polished core slab showing a sharp basal contact overlying Facies 1 muddy limestone. Note the thin bioclastic grading above the sharp basal contact. Skeletal debris (bivalves, Bi) and calcite cement filling a late stage fracture are present. (D and E) Photomicrograph showing the fine-grained bioclastic muddy material of facies 2; HCS peloidal grainstone intraclast and early burial fractures. (F) Photomicrograph displaying the effects of bioturbation on the original depositional texture. (G) Photomicrograph showing non-ferroan calcite cement in early burial fractures; HCS peloidal grainstone intraclast.

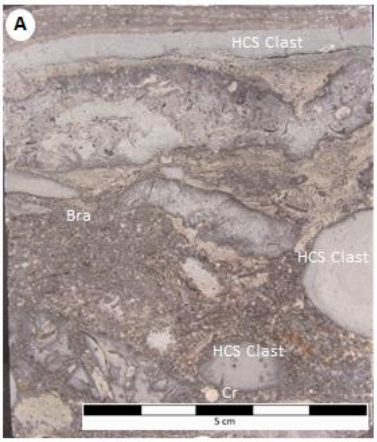
A
HCS Clast
Bra
HCS Clast
HCS Clast
Cr
5 cm


B
Bioturbation
Shale
5 cm

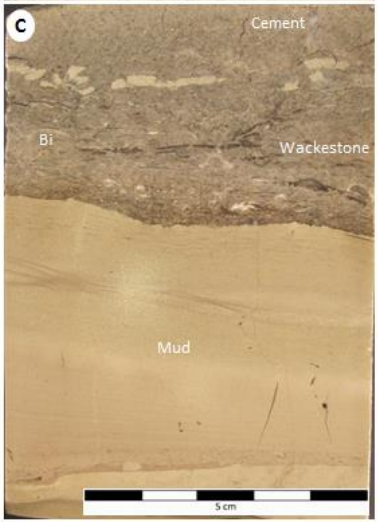
C
Cement
Bi
Wackestone
Mud
5 cm

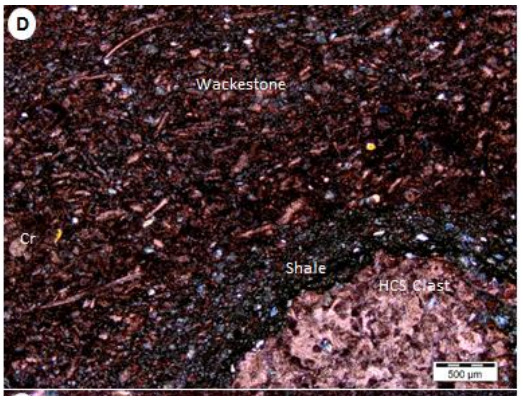
D
Wackestone
Cr
Shale
HCS Clast
500 µm

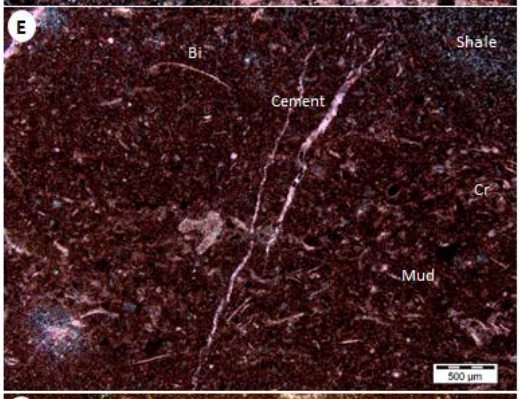
E
Bi
Shale
Cement
Cr
Mud
500 µm

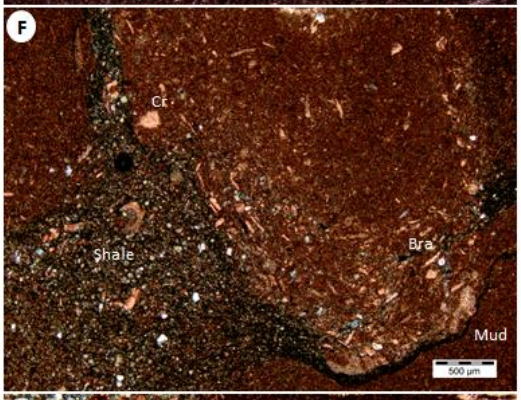
F
Cr
Shale
Bra
Mud
500 µm

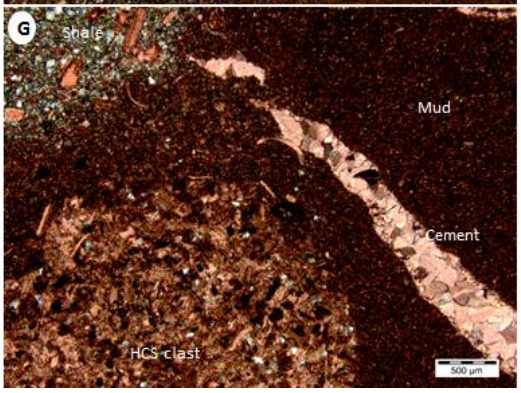
G
Shale
Mud
Cement
HCS clast
500 µm

Facies 3: HCS/SWS grainstone

This facies consists of medium to thick bedded hummocky/swaley cross-bedded (HCS/SWS) peloidal grainstone locally interbedded with calcareous shale but typically amalgamated to form larger bedsets (Fig. 5.4). The grainstone consist of well sorted fine sand-sized peloids with some floating silt-sized angular quartz particles. The basal bed contact is sharp overlain by normal graded bioclastic, locally intraclastic, material (Figs. 5.4F to 5.4I). HCS/SCS beds are locally associated with brachiopod shell bed coquinas. Small gutter casts to meter-wide elongated channels (oriented 200°, n=25) are capping amalgamated HCS/SWS grainstone bedsets. Large transported abraded metazoans (stromatoporoids, tabulate corals), up to 30 cm in size are commonly filling these channels with more disarticulated bioclastic material (e.g. crinoids, brachiopods, bryozoans, trilobites; Fig. 5.4, 5.5B and 5.5D). These channels are at their turn overlain by large symmetrical wave ripple marks (~30-50 cm in wavelength; 5-20 cm in height) oriented roughly E-W (~100°; n=22; Fig. 5.12A). Bioturbation is ubiquitous and shows both syn- and post trace fossil assemblages. Non-ferroan sparry calcite cement fills both intra- and inter-particulate voids. Rare ferroan calcite cement fills late stage fractures. This facies, typically interbedded with either facies 1 or 2, represents ~25% in thickness of the entire studied succession (Fig. 5.13).

Facies 3 represents coarser sediments deposited on a storm dominated shallow mid-ramp. These sediments are considered more proximal tempestites because of the presence of normal grading and fine to medium sized sediments. Furthermore, amalgamated HCS and SWS show that Facies 3 was formed at, or near, the fair-weather wave base (Dumas and Arnott, 2006). The channels likely formed in response to strong rip currents oriented perpendicular to the paleoshoreline while the sand waves recorded shallow water waves running parallel to the paleoshoreline.

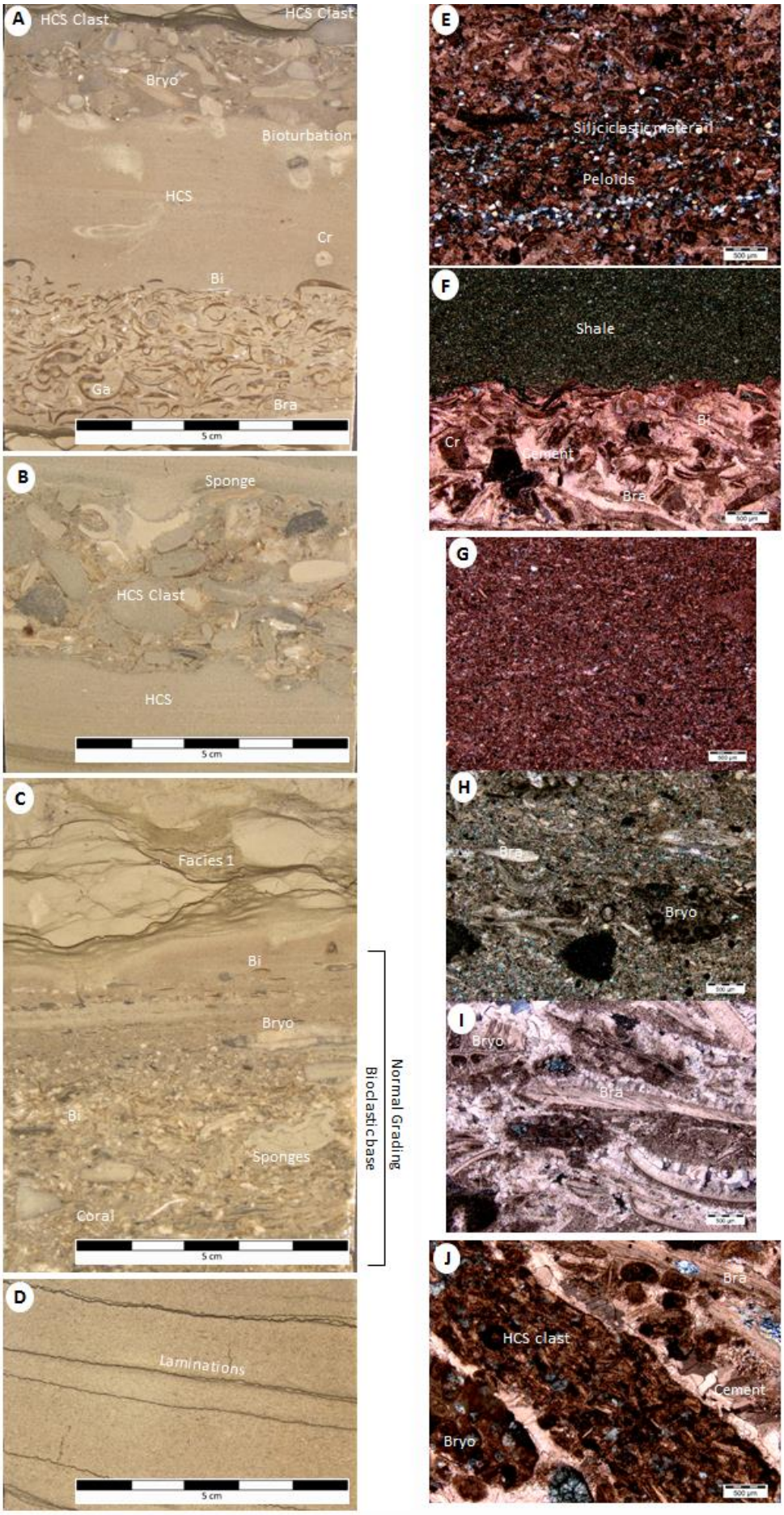
A
HCS Clast
HCS Clast
Bryo
Bioturbation
HCS
Cr
Bi
Ga
Bra
5 cm
B
Sponge
HCS Clast
HCS
5 cm
C
Facies 1
Bi
Bryo
Bi
Sponges
Coral
5 cm
D
Laminations
5 cm
Normal Grading
Bioclastic base
E
Siljciclastic material
Peloids
F
Shale
Cr
Cement
Bra
G
H
Bra
Bryo
I
Bryo
Bra
J
Bra
HCS clast
Cement
Bryo

Figure 5.4 (see previous page). Core slabs and photomicrographs showing the HCS/SWS peloidal grainstone. (A) Core slab displaying amalgamated HCS beds. Bioclasts are gastropods (Ga), brachiopods, bivalves and crinoids. Lighter coloured areas indicate bioturbation. (B) Core sample showing the contact between two amalgamated HCS beds. (C) Facies 3 overlain by muddy limestone of Facies 1. Normal bioclastic grading is present. (D) Core sample showing laminations of siliciclastic material in well sorted peloidal grainstone. (E) Photomicrograph showing internal laminations in HCS peloidal grainstone. (F) Photomicrograph displaying contact with muddy limestone of Facies 1. A bioclastic base is present and composed of cemented crinoids, brachiopods, bryozoans, trilobites and corals. (G to I) Photomicrographs showing normal grading with small to large bioclasts marking the base of some HCS peloidal grainstone beds. (J) Photomicrograph showing HCS intraclasts at the base of a HCS peloidal grainstone bed. Non-ferroan calcite cement fills inter-particles pore spaces.

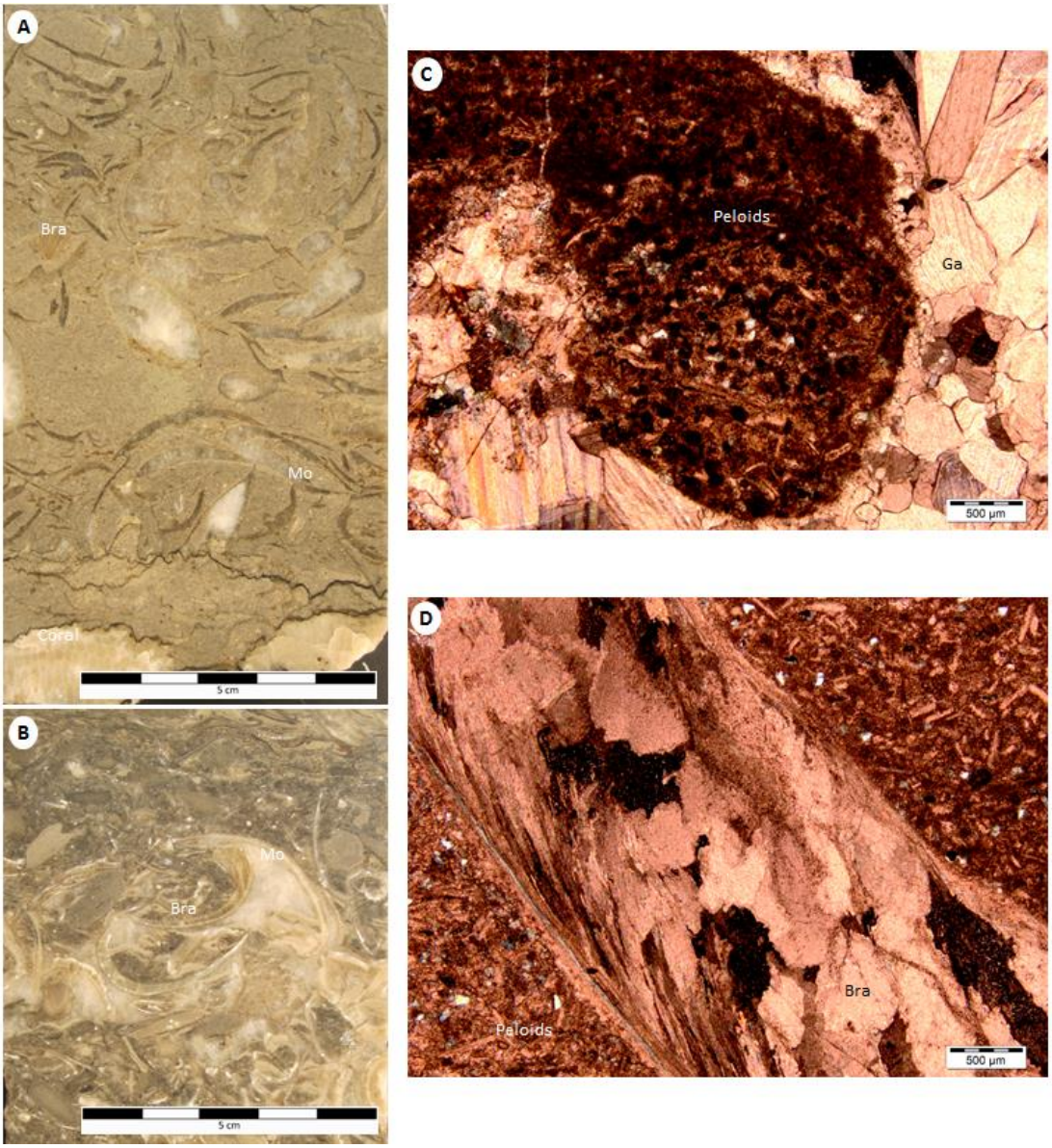

Figure 5.5 (see previous page). Core samples and photomicrographs showing coquinas associated with HCS peloidal grainstone beds. (A) Core sample showing a mollusk (Mo) coquina mostly composed of bivalves, gastropods and some rare brachiopods. (B) Core sample displaying a brachiopod coquina composed of abundant brachiopods and rare mollusks. (C) Photomicrographs showing a mollusk coquina with a large spar-filled gastropod. (D) Photomicrograph displaying a neomorphosed pentamerid brachiopod shell.

Facies 4: Wave Ripple/Small Scale HCS Calcarenite

Facies 4 is composed of a medium to thick bedded wave ripple to amalgamated calcarenite (Mauviel, 2016). It is peloid rich and also contains silt-sized quartz particles (Fig. 5.6C). We can observe wave ripples and small scale HCS with a sub-meter wavelength (Figs. 5.6A and 5.6B). The basal contact is scoured and overlain by a thin coarse bioclastic lag. When present, bioclasts are abraded (Mauviel, 2016). This facies is only present in the Upper Lousy Cove Member of the Ellis Bay Formation and represents ~3% of all the studied succession (Fig. 5.13).

Facies 4 is interpreted to have formed in an inner ramp to shoreface setting above the fair weather wave base because of the wave-ripple and small scale HCS presence. The shallow water depth needed to form those short wavelengths is met in this setting. Also, the lack of calcareous shale shows that the small ripples were not the result of large wave reworking (Dumas and Arnott, 2006).

Figure 5.6 (see next page). Field photographs and photomicrographs showing the wave ripple/Small scale HCS calcarenite. (A) Field picture displaying wave-ripple cross-stratification. (B) Field picture showing wave-ripple cross-stratification (taken form Mauviel, 2016). (C) Photomicrograph displaying the peloid rich calcarenite with silt-sized quartz particles (taken form Mauviel, 2016).

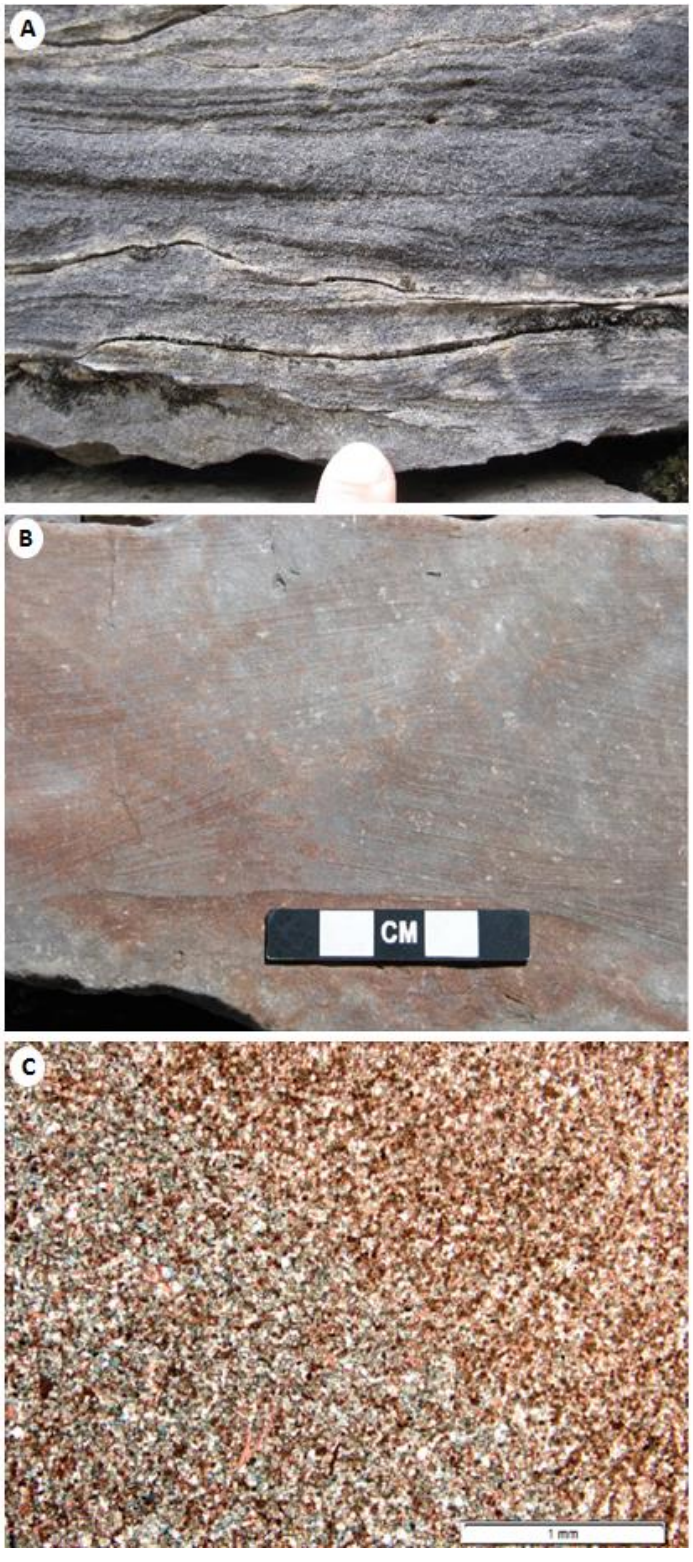
A
B
CM
C
1 mm

Facies 5: Intraclastic rudstone

Facies 5 comprises medium to thick-bedded intraclastic rudstone. The rudstone is formed of peloids, siliciclastic material, calcite cements, small to large bioclasts and rare mud (Fig. 5.7). Infiltration mud can also be seen (Figs. 5.7B and 5.7E). There are three different types of clasts based upon their origin: HCS, mud and bioclasts (Figs. 5.7A to 5.7F). In addition, it contains channels (30 to 50 cm wide; n=33; Fig. 5.12C) filled with thin bioturbated beds and remobilized abraded corals and stromatoporoids. Also, asymmetrical ripples (n=7) are present (Fig. 5.12B). Channels and asymmetrical ripples are roughly oriented N-S (~200°) meaning they are perpendicular to the paleoshoreline. The rudstone shows sharp basal contacts usually with mud and peloid filling (Fig. 5.7E). Non-ferroan calcite cement fills intra-particles voids and ferroan calcite cement generally fills voids. Furthermore, there is presence of abundant remobilized abraded corals and stromatoporoids mostly in the channels. Other bioclasts include crinoids, brachiopods, bryozoans and trilobites. Facies 5b) is really similar to facies 5. It is a thinly to medium bedded bioclastic rudstone (Fig. 5.8). The only difference is that it contains more bioclasts with a larger amount of stromatoporoids. Facies 5 and 5b) are interbedded with facies 1 and 3. Facies 5 and 5b) represent ~15% of all the studied succession (Fig. 5.13) and are present in the Becscie and Lower Gun River formations.

These facies are viewed as medium to coarse grained sediments deposited in a shallow environment above fair weather wave base where the sediments can be reworked by the waves and different currents (MacMahan et al., 2006). They are considered high energy rip current channels because of the presence of large intraclasts and bioclasts that have evidences of remobilization and abrasion in channels. Furthermore, with the presence of stenohaline fauna, it shows that it was deposited in the open marine inner ramp.

Figure 5.7 (see next page). Core photographs and photomicrographs showing the intraclastic rudstone. (A) Core photograph displaying HCS and mud intraclasts with few bioclasts such as sponges and brachiopods. (B) Core photograph showing several clasts (e.g. HCS and mud intraclasts) and bioclasts (e.g. recrystallized sponges and corals). Infiltration mud is also present. (C) Core photograph displaying HCS intraclasts with sponges. Infiltration mud is present at the base and cement fills voids. (D) Photomicrograph showing multiple clasts such as HCS and mud intraclasts with a "matrix" of cement, peloids and large amount of bioclasts. (E) Photomicrograph displaying bioclasts, intraclasts and voids filled by non-ferroan calcite cement. A sharp contact can be seen between the non-ferroan calcite cement and infiltration mud. (F) Photomicrograph showing a large HCS intraclast, some bioclasts and voids filled by non-ferroan calcite cement. (G) Photomicrograph displaying a recrystallized gastropod with peloids, mud and non-ferroan calcite cement.

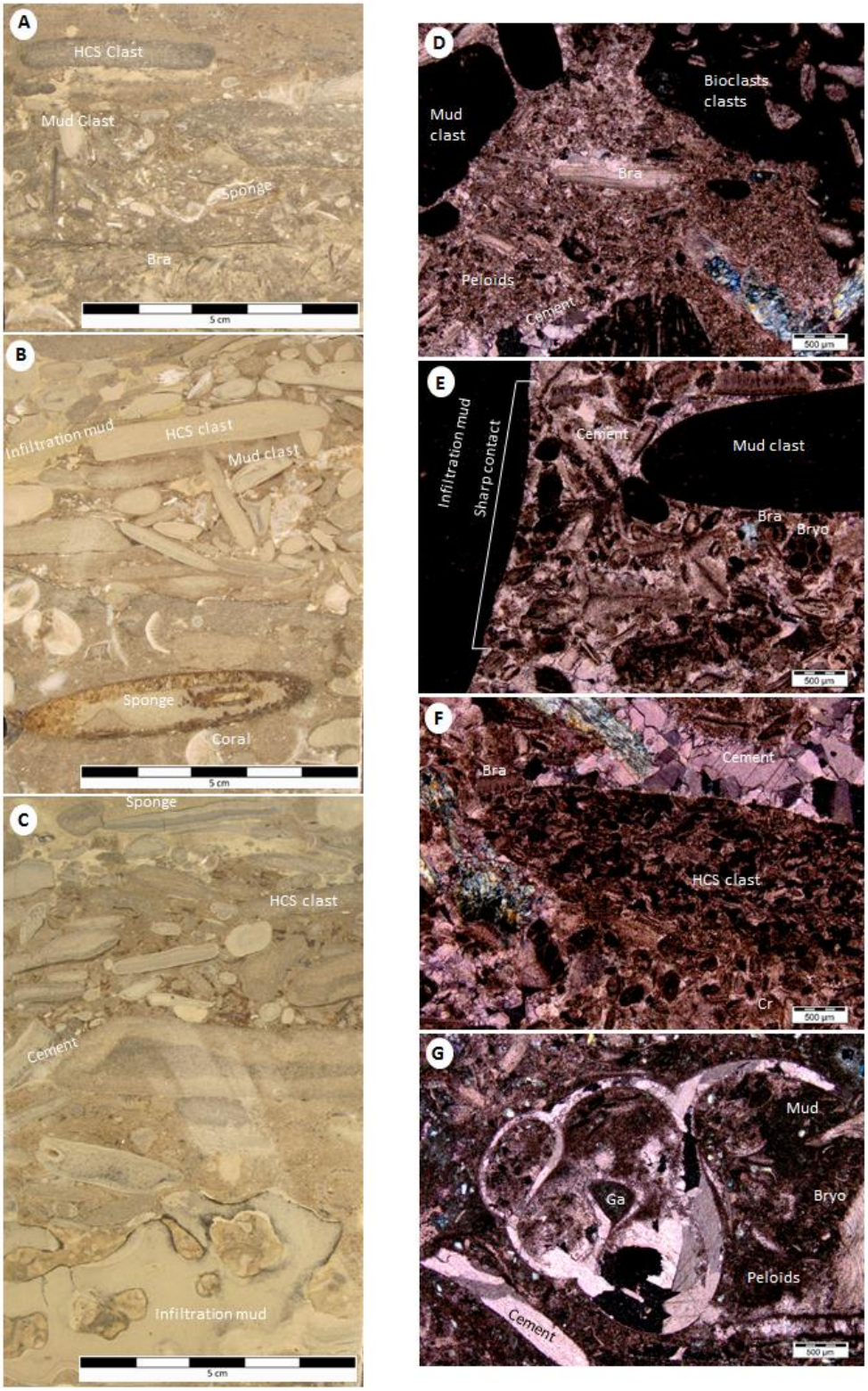
A
HCS Clast
Mud Clast
Sponge
Bra
5 cm
B
Infiltration mud
HCS clast
Mud clast
Sponge
Coral
5 cm
Sponge
C
HCS clast
Cement
Infiltration mud
5 cm
D
Mud clast
Bioclasts clasts
Bra
Peloids
Cement
500 µm
E
Infiltration mud
Sharp contact
Cement
Mud clast
Bra
Bryo
500 µm
F
Bra
Cement
HCS clast
Cr
500 µm
G
Mud
Ga
Bryo
Peloids
Cement
500 µm

Figure 5.8 (see next page). Core and field photographs and photomicrographs showing the bioclastic rudstone. (A) Core photograph displaying a large amount of bioclasts including abundant stromatoporoids, corals and brachiopods with HCS clasts. (B) Core photograph showing abundant stromatoporoids and corals. A sharp basal contact with facies 3 can also be seen. (C) Field photograph showing a medium sized channel oriented perpendicular to the paleoshoreline. (D) Photomicrograph displaying abundant bioclasts such as brachiopods, trilobites (Tri), crinoids and bryozoans with non-ferroan calcite cement and few quartz particles surrounding them. (E) Photomicrograph showing a large amount of bioclasts with peloids and non-ferroan calcite cement enclosing the bioclasts. (F) Photomicrograph displaying a large stromatoporoid. (G) Photomicrograph showing a large recrystallized and remobilized coral.

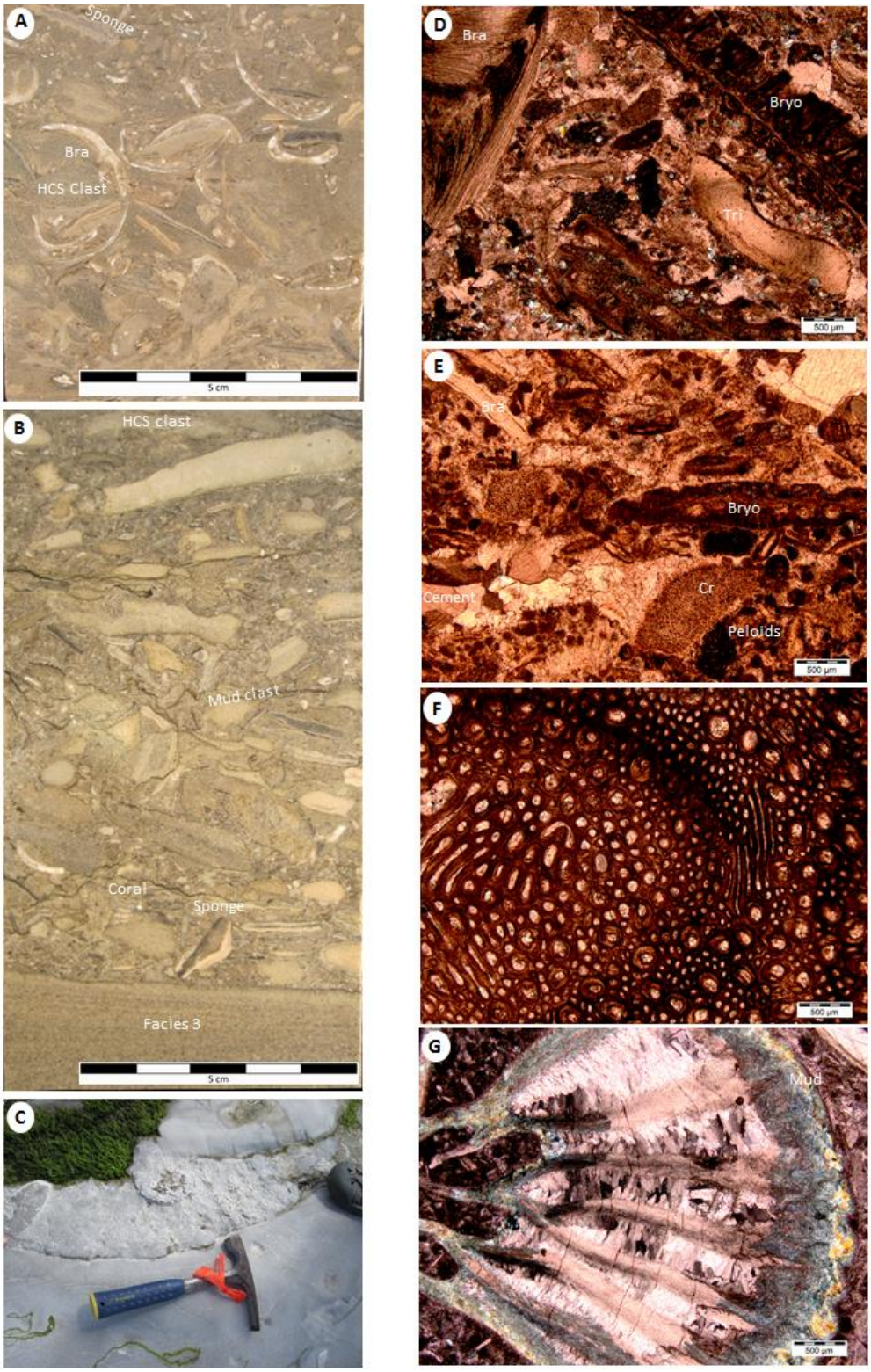
A
Sponge
Bra
HCS Clast
5 cm
B
HCS clast
Mud clast
Coral
Sponge
Facies 3
5 cm
C
D
Bra
Bryo
Tri
500 µm
E
Bra
Bryo
Cement
Cr
Peloids
500 µm
F
500 µm
G
Mud
500 µm

Facies 6: Bioclastic grainstone

Facies 6 is a thin to medium bedded, bioclastic grainstone. This facies consists of mostly coarse bioclastic grains with peloids and few quartz particles (Fig. 5.9). Intraclasts of different compositions are locally present. This facies displays large wave ripple marks (~50-80 cm in wavelength; 15-20 cm in height) with the paleocurrent toward the shoreline with a general direction of 25° (n=7; Fig. 5.12D). Geopetal and umbrella structures are present. Non-ferroan calcite cement fills intra- and inter-particles voids. Bioclasts are abundant and comprised of brachiopods, bryozoans, crinoids, trilobites, corals, stromatoporoids and bivalves (Fig. 5.9). This facies is interbedded with facies 1 and 3 and commonly overlain facies 3 and 5 and represents ~6% of the studied succession (Fig. 5.13). Facies 6 is present in the Becscie and Merrimack formations.

This facies represents shallow water sediments deposited in the inner ramp. Thus, the high energy events can remobilize and transport the particles towards the shoreline above fair weather wave base (Bassetti et al. 2006). They are considered high energy mobile sand bottom because of the presence of large wave ripple. In spite of their inner ramp setting, they were deposited in an open marine setting as evidenced by the presence of a stenohaline dominated fauna.

Figure 5.9 (see next page). Core photographs and photomicrographs showing the bioclastic grainstone. (A) Core photograph displaying abundant aligned bioclasts such as crinoids, bivalves, sponges and corals with HCS intraclasts. (B) Core photograph showing sharp contact of the bioclastic grainstone with facies 3. (C) Core photograph displaying bioclasts and HCS intraclasts. (D) Photomicrograph showing three types of intraclasts: HCS peloidal grainstone, bioclasts, lime mud. (E) Photomicrograph displaying abundant large bioclasts with non-ferroan calcite void-filling cement. (F) Photomicrograph showing abundant large bioclasts and peloids with non-ferroan calcite void-filling cement. (G) Photomicrograph displaying large bioclasts, quartz particles and peloids with non-ferroan void-filling calcite cement.

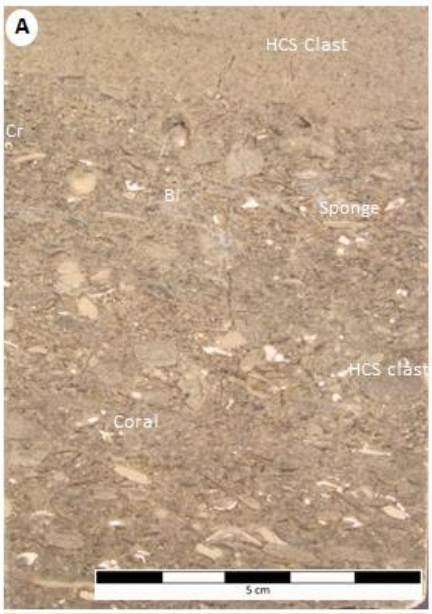
A
HCS Clast
Cr
Bi
Sponge
HCS clast
Coral
5 cm

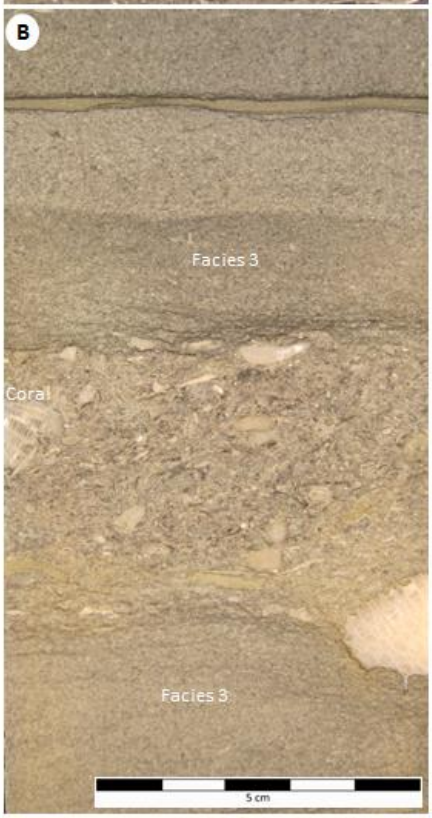
B
Facies 3
Coral
Facies 3
5 cm

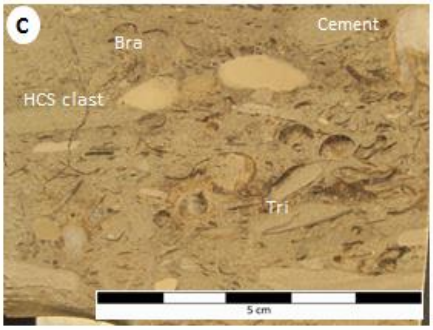
C
Cement
Bra
HCS clast
Tri
5 cm

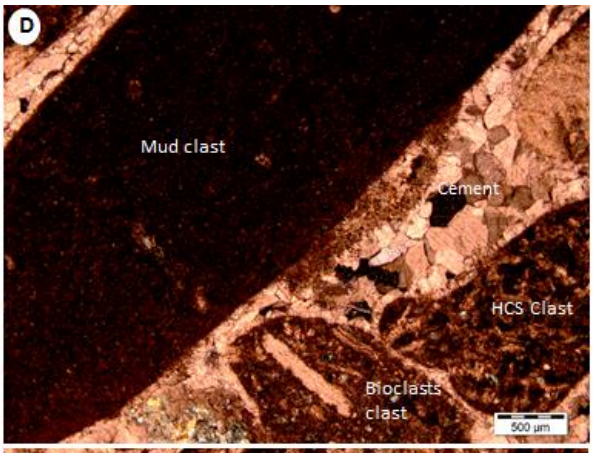
D
Mud clast
Cement
HCS Clast
Bioclasts
clast
500 µm

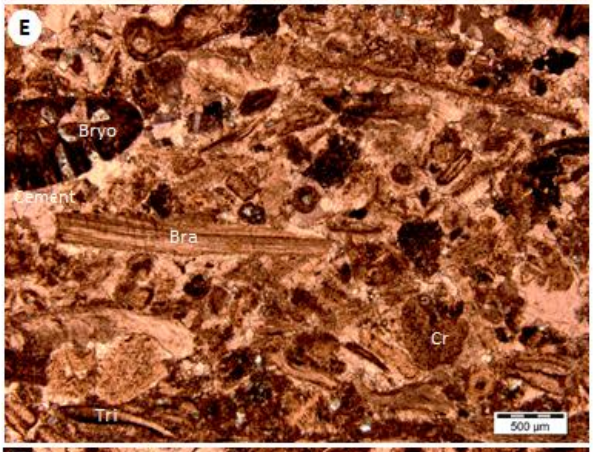
E
Bryo
Cement
Bra
Cr
Tri
500 µm

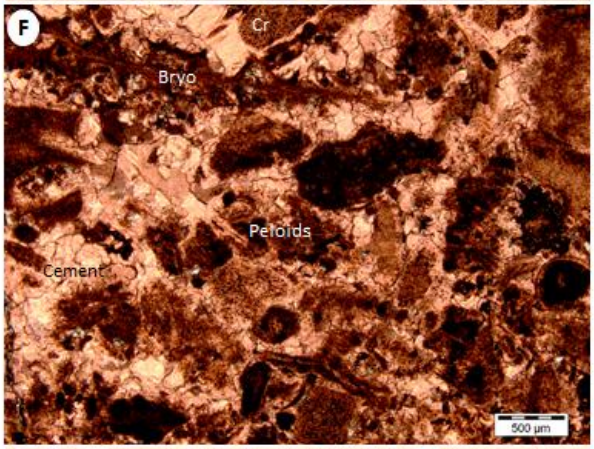
F
Cr
Bryo
Peloids
Cement
500 µm

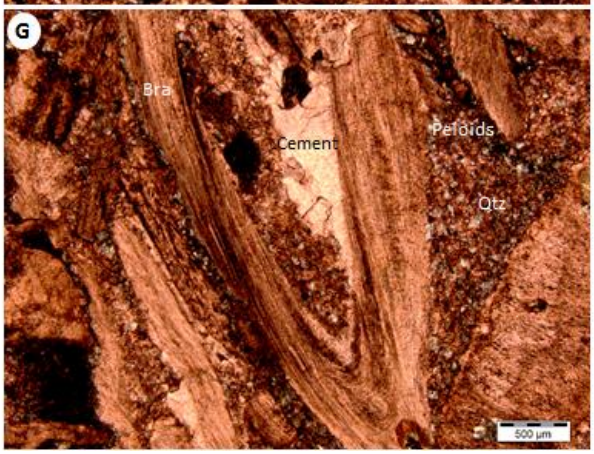
G
Bra
Cement
Peloids
Qtz
500 µm

Facies 7: Oncolitic calcirudite

Facies 7 is a poorly bedded, massive unit (10-100 cm in thickness) oncolitic calcirudite. It is comprised of a high number of calcimicrobial oncoids (Fig. 5.10). This massive unit rests on an erosion surface present at the regional scale with an intraclasts lag deposit. The oncoids are generally aligned and commonly fine upward with cross-bedding to wave-ripple cross-lamination (locally present). Large abraded bioclasts are present including solitary rugose corals, tabulate corals, stromatoporoids, and bryozoans (Farley, 2008; Mauviel, 2016). This facies is only seen at the base of the Laframboise Member in the Ellis Bay Formation. It represents ~2% of the studied succession (Fig. 5.13).

This facies is interpreted to be deposited in a continuously agitated environment above the fair weather wave base since strong waves are needed to create the oncoids. Also the cross-bedding suggests a shallow energetic environment equivalent to the inner ramp and more precisely a beach to shoreface setting (Farley, 2008; Mauviel, 2016). The erosion surface indicates a subaerial exposure and henceforth a sea-level fall (Desrochers et al., 2010).

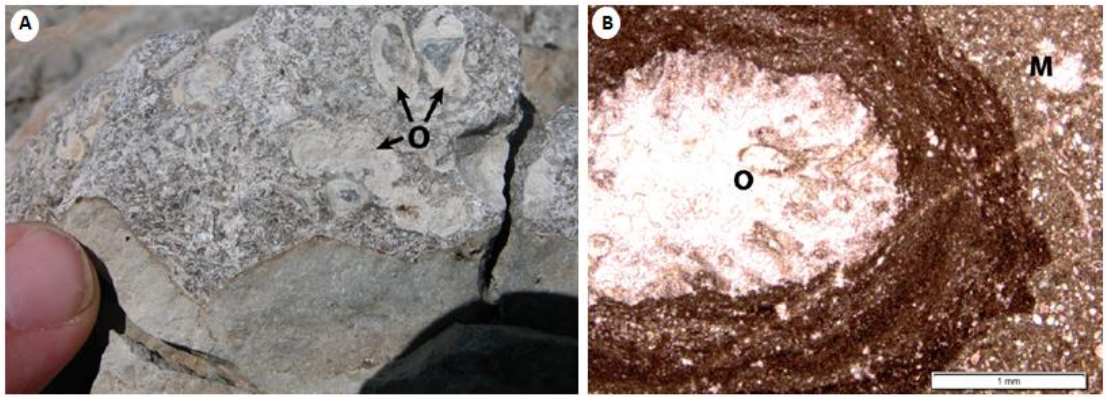

Figure 5.10. (A) Field picture showing cm-scale oncoids (o) disconformably underlain with the facies 4 in the Ellis Bay Formation. (B) Photomicrograph displaying an oncoid (o) in a calcisiltite matrix (m).

Facies 8: Calcimicrobe-Metazoan Reefs

Facies 8 consists of stratigraphic reef with massive biohermal core subfacies, up to 5 m thick, and thin-bedded inter-reef subfacies composed of interbedded mud-supported bioclastic limestone and calcareous shale. Boundstones layers interbedded with shale partings are present in the massive core. These internal 10-30 cm thick boundstone layers are built by a consortium of calcimicrobes, tabulate corals, bryozoans and stromatoporoids (Fig. 5.11). The bioherms are capped by a regional erosion surface with a black pyritic-rich hardground that shows differential erosional topography; massive cores have a more positive topography than the more recessive inter-reef facies (Desrochers et al., 2008; Farley, 2008; Mauviel, 2016). This facies is only present in the Laframboise Member of the Ellis Bay Formation and represents ~2% of the studied succession (Fig. 5.13).

Facies 8 represents patch reef development on an inner to mid ramp setting above fair weather wave base. The composition of the frame builders indicates an open marine setting (for more details see Mauviel, 2016).

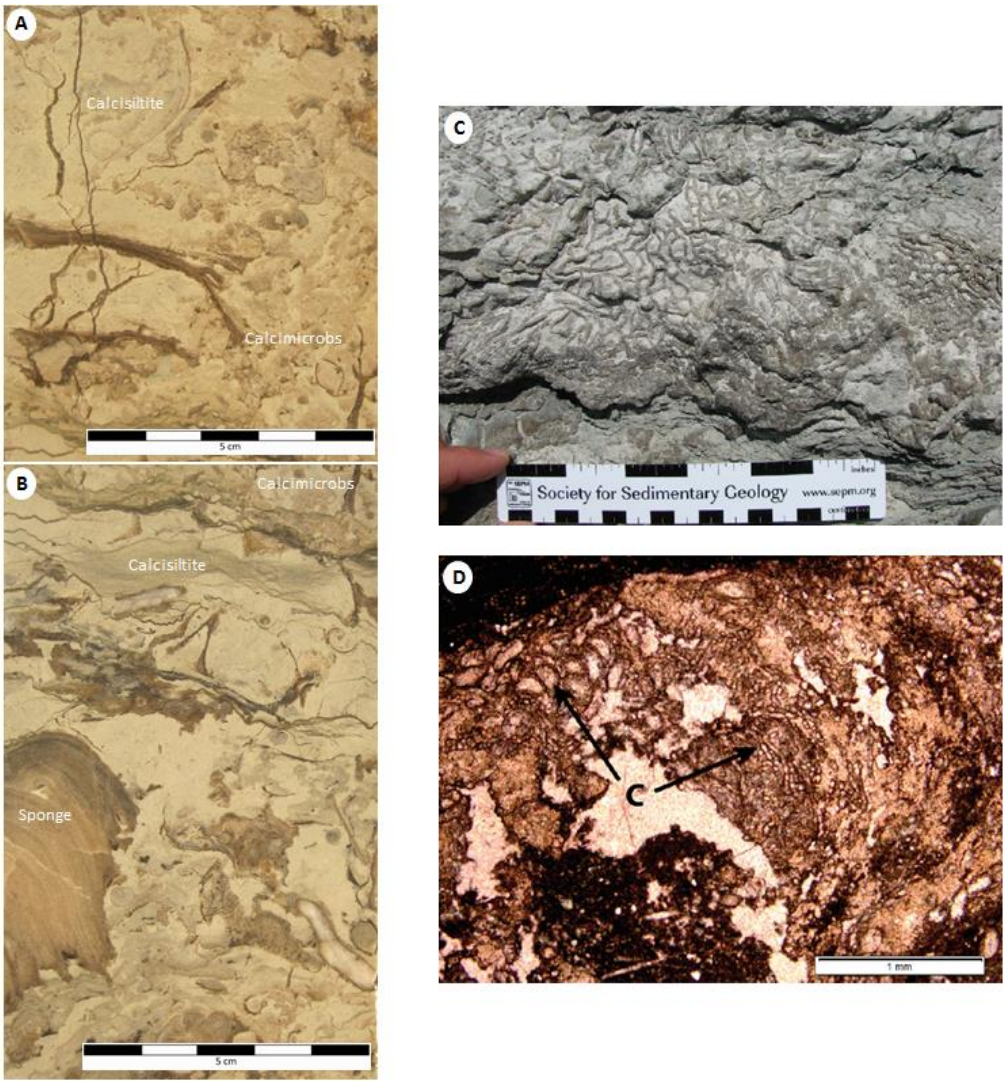

Figure 5.11. Core, field photographs and photomicrograph showing the bioherm core with the different layers that form the framework and the matrix. (A) Core photograph displaying the thrombolitic nature of the calcimicrobes as the main reef builders. (B) Core photograph showing a large stromatoporoid forming the local reef framework in association with calcimicrobes. (C) Field photograph displaying chain corals located above the calcimicrobial crust in the bioherm core in the Laframboise Member. (D) Photomicrograph showing abundant calcimicrobes in the bioherm core of the Laframboise Member.

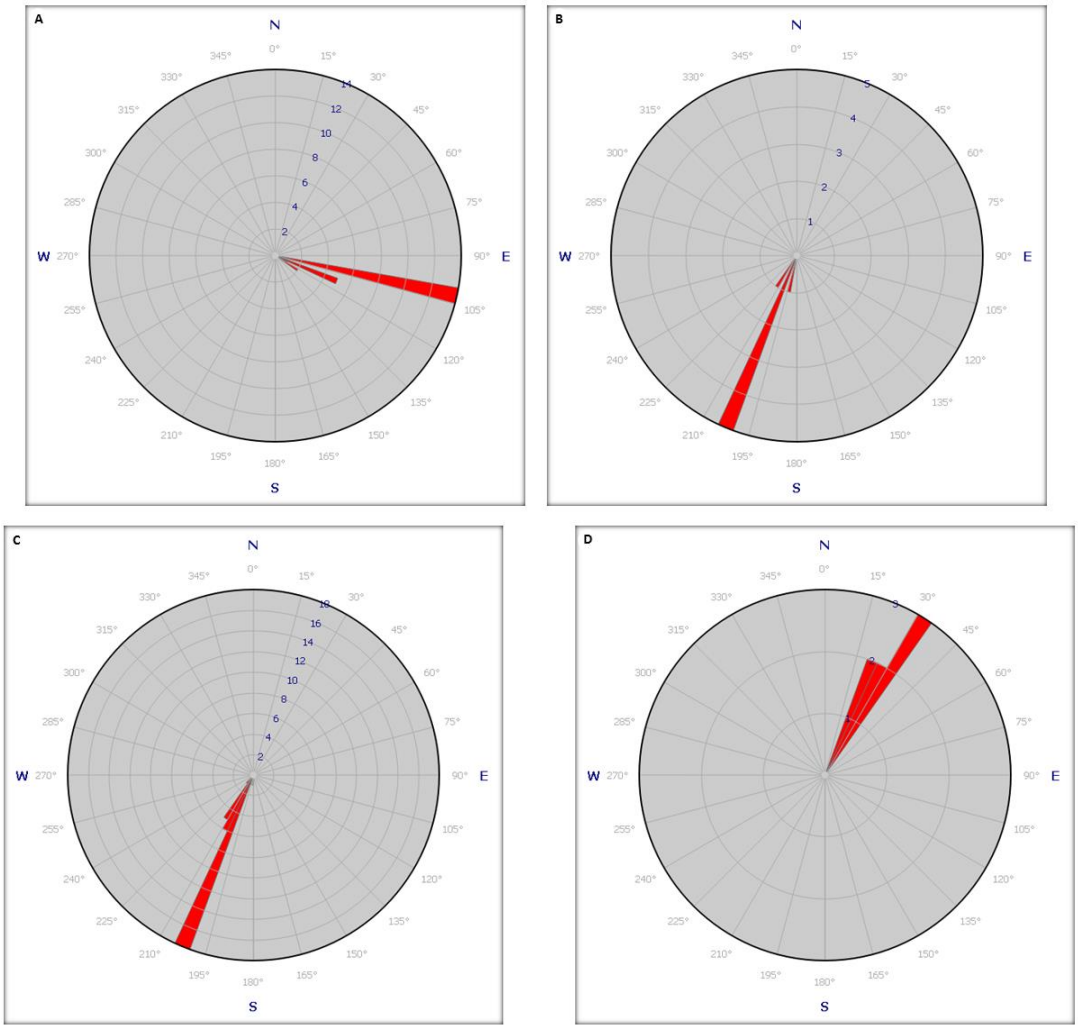

Fig. 5.12. Rose diagrams showing the paleocurrents associated with the different sedimentary structures present in the succession. (A) Rose diagram displaying orientation of the symmetrical ripples seen in Facies 3, n= 22. (B) Rose diagram showing orientation of asymmetrical ripples seen in Facies 5, n= 7. (C) Rose diagram displaying orientation of channels seen in Facies 5, n= 33. (D) Rose diagram showing orientation of cross-stratification seen in Facies 6, n= 7.

Table 1 – Facies seen in the succession (description of Facies 3, 7 and 8 from Mauviel, 2016)

Facies	Description	Interpretation
1	Thin bedded nodular **muddy limestone with calcareous shale interbeds**, variably bioturbated, and diverse fauna with sometimes **anastamosed argillaceous solutions**, bioturbated and scattered fauna. Interbedded with facies 2. Present in every formation except the **anastamosed argillaceous solutions**, present only in the Merrimack and Lower Gun River formations.	Basinal "tempestite"; open marine **outer ramp-deep basin**
2	Thinly bedded, nodular dense **bioclastic wackestone to packstone** with sharp base and graded bioclastic base, local calcareous shale interbeds; variably bioturbated, diverse fauna in micrite and peloids matrix, less nodular than 2. Interbedded with facies 1. Present in every formation.	Distal tempestites; open marine, **storm-dominated deep mid-ramp.**
3	Medium to thick bedded **HCS/SWS grainstone**, well sorted fine sand-size particles mainly peloids, normal grading at the base, sharp basal contacts, bioturbation, bed amalgamation, associated with brachiopod shell beds, gutter casts. Interbedded with almost every facies. Present in every formation. This facies is closely seen with coquinas: 1- **recrystallized and preserved abraded brachiopod** with peloid filling, oriented filling and diverse fauna in micrite and 2- **coquinas** and **recrystallized abraded mollusk coquinas** with peloid filling. Present in Becscie and Lower Gun River formations.	Proximal tempestites; open marine, **storm-dominated shallow mid-ramp.**
4	Medium to thick bedded **Wave Ripple/Small Scale HCS Calcarenite** with abundant siliciclastics and abraded bioclasts. Present only in the Upper Lousy Cove member of the Ellis Bay Formation.	Inner **ramp** to shoreface deposition
5	a) Channelized **intraclastic rudstone**, channels orientated perpendicular to the paleoshoreline, abundant remobilized abraded corals and stromatoporoids. Local dolomitization and filling with quartz particles and peloids. Local sharp base with mud filling. Medium presence of diverse fauna. Clasts: HCS, mud, bioclastic ones. Interbedded mostly with facies 3. Present in Becscie and Lower Gun River formations.	High energy rip current channels, open marine **inner ramp**.
	b) **Same as 5a) but more of a bioclastic rudstone**: peloids as filling and clasts. Also presence of mud and bioclastic clasts. Abundance of diverse fauna. Interbedded mostly with facies 3. Present in Becscie and Lower Gun River formations.	
6	Thin to medium bedded, **bioclastic grainstone** with large wave ripple marks (~50-80 cm in wavelength; 15-20 cm in height), paleocurrent toward the shoreline, diverse fauna. Silicification in bioclasts and as filling by quartz particles. Dolomitization and different types of intraclasts are somewhat present. Also, peloidal material is common in the cements and sometimes in intraclasts. Interbedded mostly with facies 3. Present in Becscie, Merrimack and Lower Gun River formations.	High-energy mobile sand bottom, open marine agitated **inner ramp.**
7	Poorly bedded, massive unit (10-100 cm thick) resting on an erosion surface of regional extent with an intraclasts lag deposit. Abundant **calcimicrobial oncoids,** common fining-upward fabric ranging from calcirudite to fine calcarenite, cross-bedded to wave ripple cross-lamination locally present; associated large, highly abraded megafossils (solitary rugose corals, tabulate corals, stromatoporoids, bryozoans). Only present at the base of the Laframboise member of the Ellis Bay Formation.	Beach to shoreface
8	Up to 5.0 m thick, stratigraphic **reef cores** interfingering with thin-bedded, mud-supported bioclastic limestone and shale. 10-30 cm thick amalgamated boundstone layers separated by shale partings with, in order of importance: calcimicrobes, tabulate corals, bryozoans and stromatoporoids. Bioherm capped by an erosional surface of regional extent exhuming resisting cores and removing partially to totally inter-reef facies. Paleorelief up to 1.5 m drapped by basal Becscie strata. Overlying facies 5 in the Laframboise member of the Ellis Bay Formation.	Inner- mid ramp patch.

Composite Log

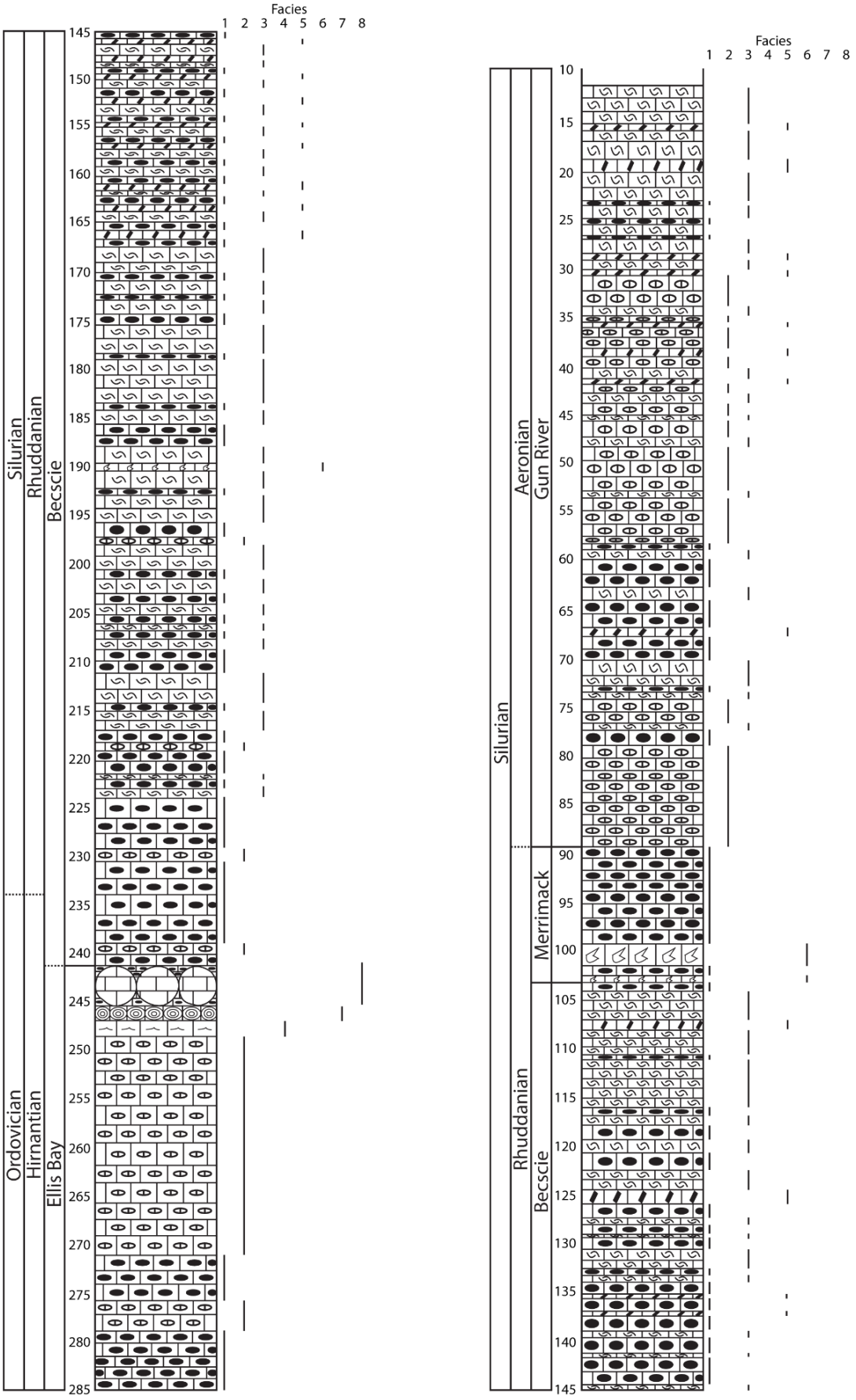

Figure 5.13 (see previous page). Composite log showing the vertical facies distribution in the La Loutre #1 drill core. Facies 1, 2 and 3 are by far the most abundant representing a total of ~70% of the entire thickness of the formations. They are also present in all formations. Facies 3b), 5 and 5b) are only present in the Becscie and Gun River formations. Facies 6 is present in the Becscie and Merrimack formations. Facies 7 and 8 are exclusively present in the Ellis Bay Formation.

5.2 Stratigraphic Architecture

Several stratigraphic tools were used to determine the stratigraphic architecture including: textural changes, gradual versus abrupt facies shifts, bed thickness changes, sedimentary and biotic structures, and differential weathering enhancing the overall facies stacking. In the La Loutre #1 core, similar tools were used but the recognition of stratigraphic facies motifs was more difficult due to the fresh unweathered nature of the core material compared to the coastal outcrops. In general, we identify a repetitive facies pattern at two scales: at the metre scale (<2 m) and at multi-metre to decametre scale (4-10 m). These two imbricated orders are present in the whole studied succession defining Transgressive-Regressive (T-R) cycles. An individual TR cycle is delimited by Maximum Regressive Surface or zones (MRS) and divided by a Maximum Flooding Surface or zone (MFS) into a lower Transgressive System Tract (TST) and an upper Regressive System Tract (RST). A TST is characterized by fining- and bed thickening-upward trends while the RST displays the inverse trend. The metre and decametre cycles are typically asymmetrical with the RSTs relatively thicker than the TSTs.

Field observations and interpretation

In coastal outcrops, stratigraphic cycles (Fig. 5.17) were described at the following locations: i) Baie des Nabots for the Lower Becscie strata, ii) at Baie des Sarcelles for the Middle Becscie strata and iii) at the mouth of the Becscie River for the Upper Becscie strata. In the Becscie Formation, both metre- and decametre-scale cycles are present and display an overall shallowing upward at the formation scale (Fig. 5.17). Stratigraphic cycles are dominated by finer grained facies (Facies 1 and 2) at the base of the Becscie Formation (Fig. 5.14) while coarser grained facies capped by symmetrical wave ripples (Facies 3) are more common in the middle Becscie Formation (Fig. 5.15). The upper Becscie Formation (Fig. 5.16) is mainly characterized by amalgamated HSC grainstone

beds (Facies 3) with intraclast or coral-rich channels capped by asymmetrical sand ripples (Facies 5 and 6). The overall shallowing upward nature present in the Becscie Formation is interpreted as high frequency sea level changes superimposed on a long-term regression that captured progressively shallower ramp cycles. The key stratigraphic surfaces (MRZ in red, MFZ in blue) at each studied coastal outcrops are located (see Appendices 1 to 3). The recessive nature of the Merrimack Formation, however, prevents us to map stratigraphic cycles in the younger units (see Appendix 4).

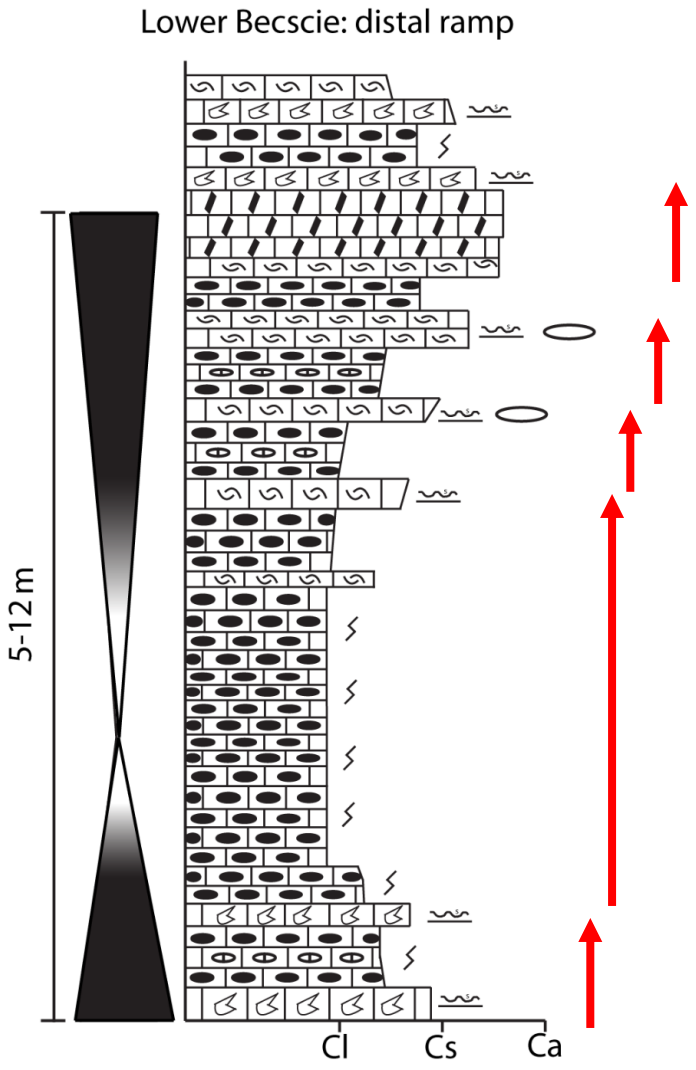

Figure 5.14 (Previous page). Schematic diagram showing the multi-meter to decameter scale cycles in the Lower Becscie where the TR cycles are displayed by textural gradients; black is for the MRS or MRZ and white is for the MFS or MFZ. Also, the meter-scale cycles (~5) are represented by the red arrows. See Fig 5.17 for facies legend.

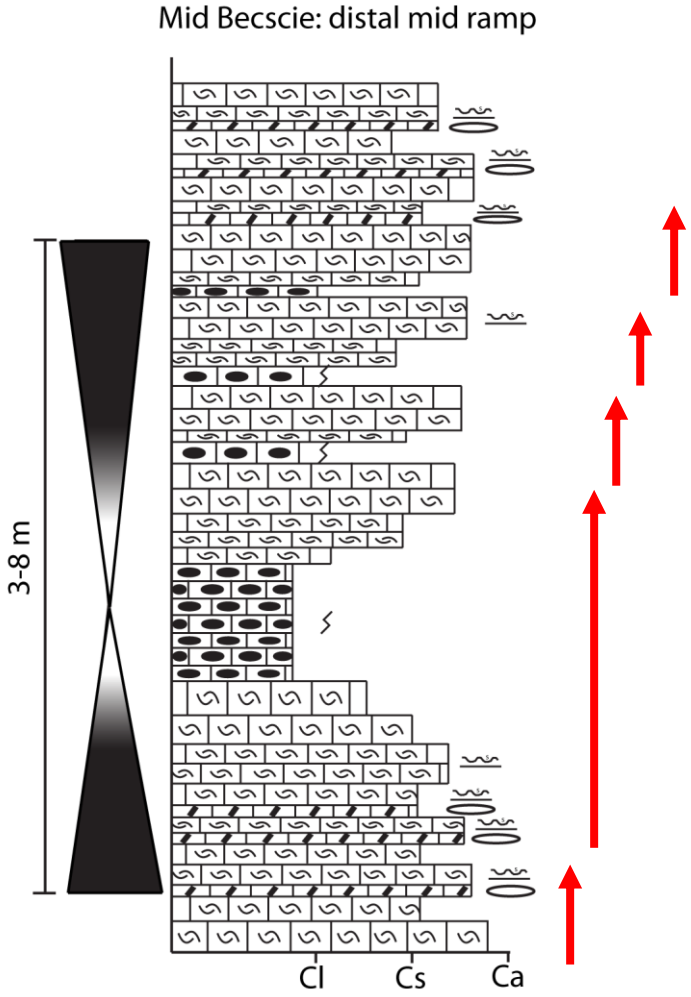

Figure 5.15. Schematic diagram showing the multi-meter to decameter scale cycles in the Mid-Becscie where the TR cycles are displayed by textural gradients; black is for the MRS or MRZ and white is for the MFS or MFZ. Also, the meter-scale cycles (~5) are represented by the red arrows. See Fig 5.17 for facies legend.

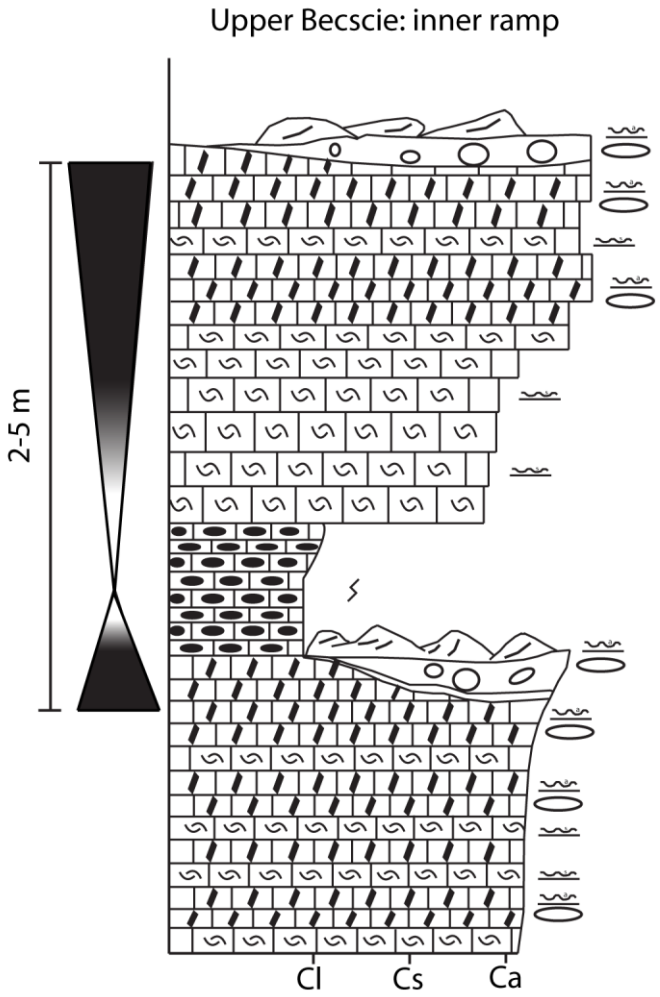

Figure 5.16. Schematic diagram showing the multi-meter scale cycles in the Upper Becscie where the TR cycles are displayed by textural gradients; black is for the MRS or MRZ and white is for the MFS or MFZ. Also, the meter-scale cycles are not represented because they are amalgamated and henceforth more difficult to depict. Symmetrical ripples separating facies 3 and 5 likely defines more minor stratigraphic cycles. See Fig 5.17 for facies legend.

Figure 5.17 (see next page). Schematic diagram showing typical low-order multi-metre to decametre-scale TR cycles present in the Becscie Formation. These TR cycles are progressively composed by more proximal facies in the upper Becscie Formation.

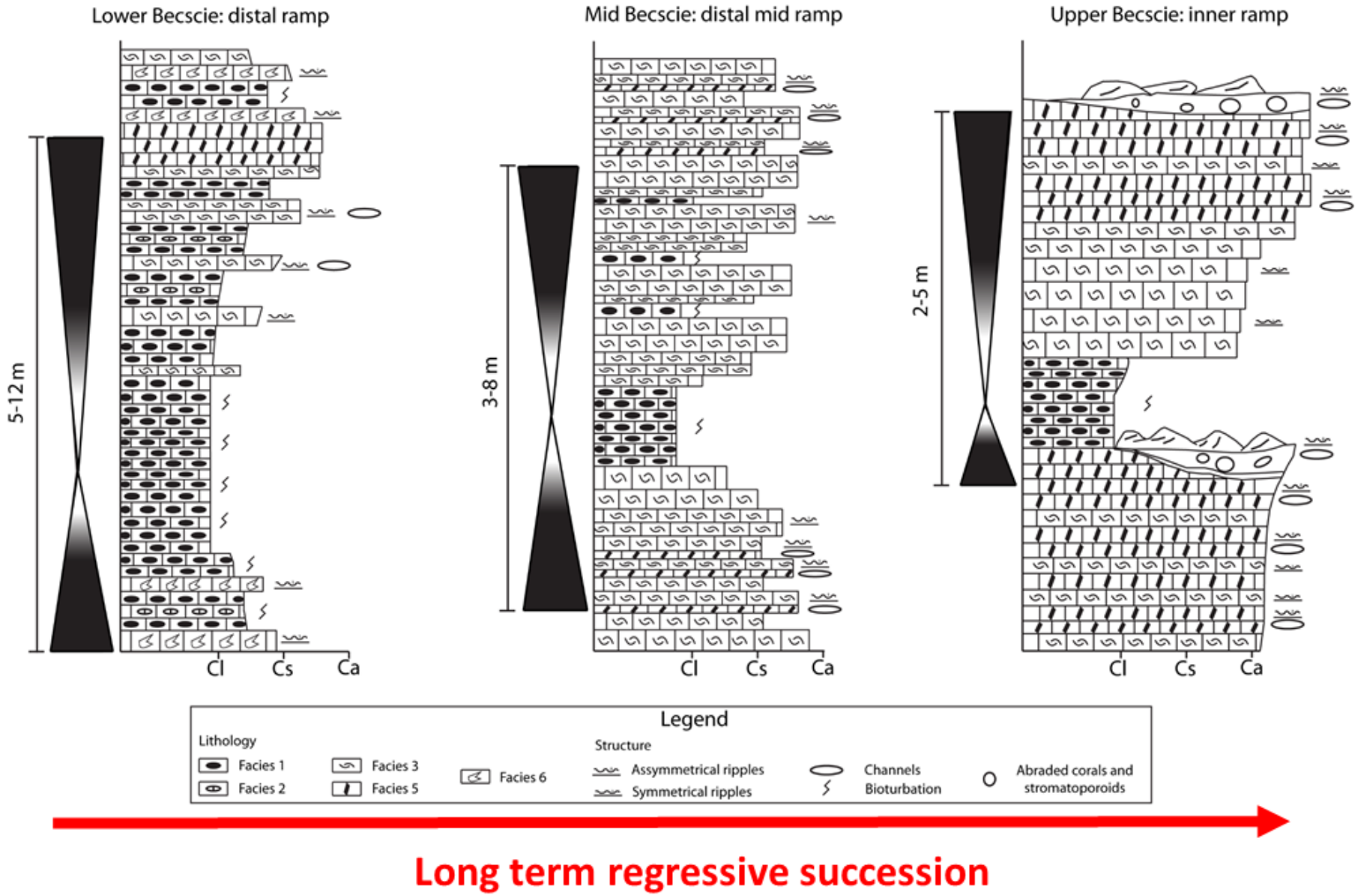
Lower Becscie: distal ramp
Mid Becscie: distal mid ramp
Upper Becscie: inner ramp
5-12 m
3-8 m
2-5 m
Cl
Cs
Ca
Legend
Lithology
Facies 1
Facies 2
Facies 3
Facies 5
Facies 6
Structure
Assymmetrical ripples
Symmetrical ripples
Channels
Bioturbation
Abraded corals and stromatoporoids
Long term regressive succession

Core observations and interpretation

Like the coastal outcrops, we were able to recognize a repetitive facies pattern in La Loutre #1 core and extend our stratigraphic architecture analysis to the whole studied succession (Fig. 5.18). The TR cycles are determined by the same processes as the surface TR cycles. Approximately 20 relatively symmetrical multi-meter to decametre-scale TR cycles are present from the upper Ellis Bay Formation to the middle Gun River Formation. The main TR cycles recognized in the subsurface are dominated by finer grained facies at their MFS or MFZ and coarser grained, commonly bed amalgamated, facies at their MRS or MRZ. Numerous smaller scale TR cycles, typically 3 to 5, are present within the former cycles but are more difficult to recognize than in the field and are not illustrated in Fig. 5.15. In the upper part of the La Loutre #1 core, the Gun River cycles are more proximal and amalgamated; thus are not illustrated in Fig. 5.18.

Figure 5.18 (see next page). Composite log of the La Loutre #1 showing the whole studied succession with the intermediate TR cycles shown on the right. The TR cycles are displayed by textural gradients; black is for the MRS or MRZ and white is for the MFS or MFZ.

Ordovician
Silurian
Hirnantian
Rhuddanian
Ellis Bay
Becscie
145
150
155
160
165
170
175
180
185
190
195
200
205
210
215
220
225
230
235
240
245
250
255
260
265
270
275
280
285

Silurian
Rhuddanian
Becscie
Aeronian
Merrimack
Gun River
10
15
20
25
30
35
40
45
50
55
60
65
70
75
80
85
90
95
100
105
110
115
120
125
130
135
140
145
Amalgamated
Proximal Cycles

5.3 Chemostratigraphy

We are presenting below our high resolution $\delta^{13}C$ and $\delta^{18}O$ study and trace element geochemistry for the entire studied succession ranging from the Late Hirnantian Ellis Bay Formation to the Aeronian Gun River Formation. The results of this section are from La Loutre #1 core.

Stable Isotope Geochemistry

Our high resolution $\delta^{13}C$ and $\delta^{18}O$ curves comprise 295 data points for a total ~260 m. Both curves are shown with a moving average (n=3) in Figs. 5.19 and 5.20. The $\delta^{13}C$ curve displays two distinct positive isotopic carbon excursions above the background value at 0‰ (Fig. 5.19). The first positive isotopic carbon excursion termed the Upper Hirnantian isotopic carbon excursion or Upper HICE, reaches up to +5‰ and extends from 220 and 250 m below the surface. The second positive isotopic carbon excursion, termed Lower Aeronian isotopic carbon excursion or Lower AICE, is sustained over a long stratigraphic interval from 15 to 100 m and reaches a +2‰. The Lower AICE is centred around the Rhuddanian-Aeronian stage boundary as defined by the brachiopod fauna (Copper and Jin, 2014). High-frequency variations (1‰ or less) in $\delta^{13}C$ values are also present. The $\delta^{13}C$ dataset fits well with the running average curve but more noise in clearly present in the Merrimack and Gun River formations.

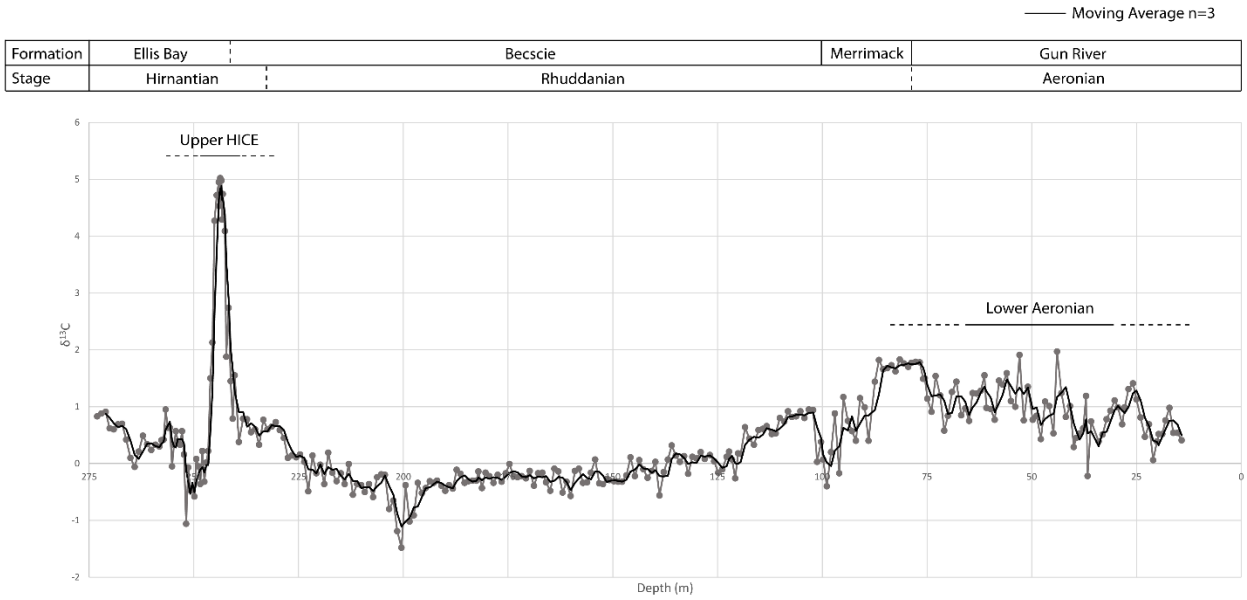

Figure 5.19. (See previous page) $\delta^{13}C$ curve (solid line is a 3-point running average) of the Upper Hirnantian Ellis Bay Formation to the Lower Aeronian Gun River Formation.

The $\delta^{18}O$ curve displays a long-term decline from -3‰ in the Ellis Bay Formation to -6‰ in the Gun River Formation (Fig. 5.20). High-frequency variations (1‰ or less) in $\delta^{18}O$ values are also present throughout the entire studied succession. A cross-plot of all the data in which $\delta^{18}O$ is plotted against $\delta^{13}C$ is given in Fig. 5.21. There is a weak correlation between these two isotope datasets (R^2 of 0.0054).

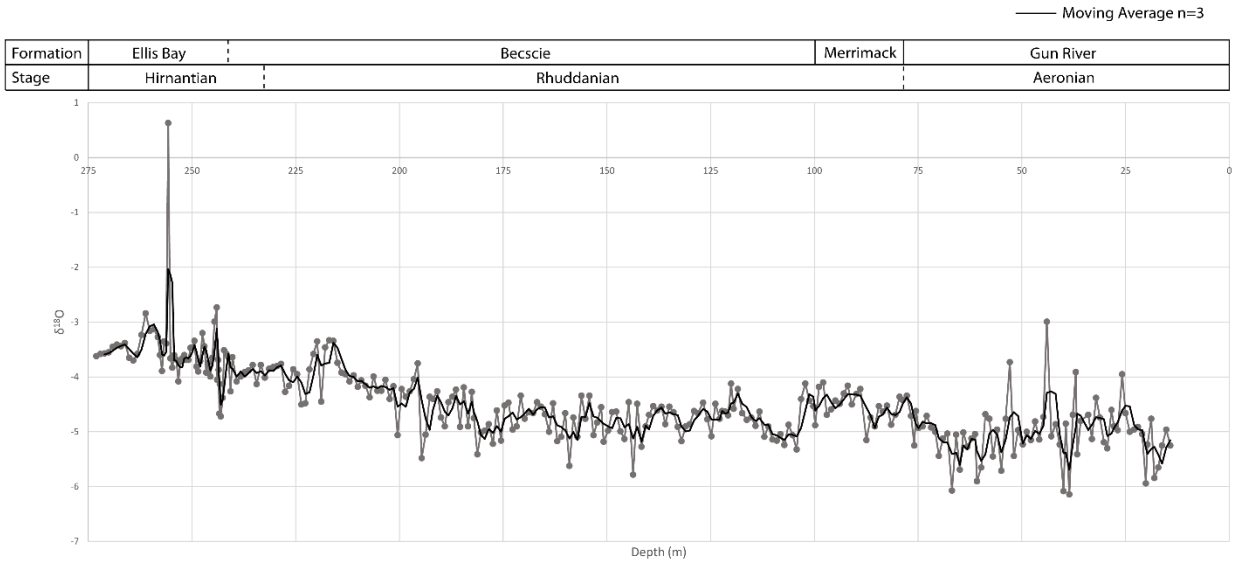

Figure 5.20. $\delta^{18}O$ curve (solid line is a 3-point running average) of the Upper Hirnantian Ellis Bay Formation to the Lower Aeronian Gun River Formation.

Figure 5.21 (see next page). Cross-plot of $\delta^{13}C$ and $\delta^{18}O$ for the entire dataset (Ellis Bay to the Gun River formations). The colours are Pink (Ellis Bay Formation), Yellow (Becscie Formation), Purple (Merrimack Formation) and Peach (Gun River Formation).

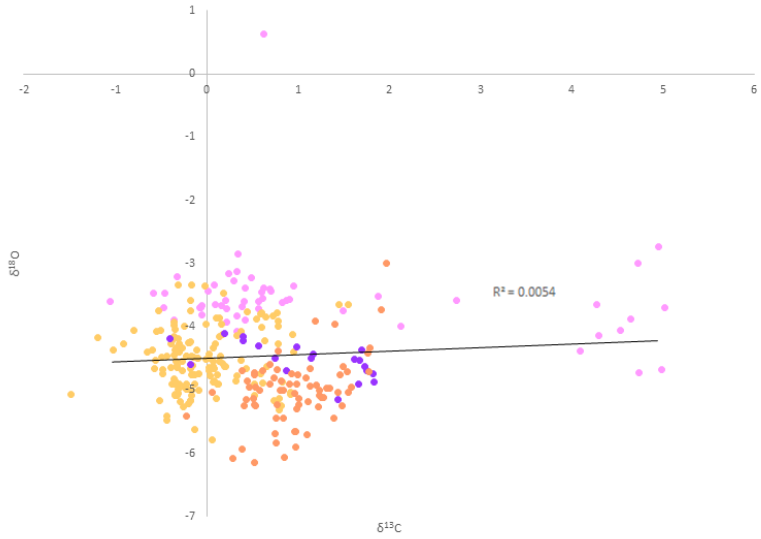

Trace Element Geochemistry

In total, trace element geochemistry was performed on representative samples (n=60 or 1 analysis for each 5 samples) of the entire studied succession (Appendix 12) for diagenetic screening. Cross-plots of key trace elements and stable isotopes (Sr/Mn, Mn/Sr vs $\delta^{13}C$ and Mn/Sr vs $\delta^{18}O$) are illustrated in Figs. 5.22 and 5.23. R^2 values for these cross-plots are 0.0157, 0.0709, and 0.0315 respectively. These R^2 values indicate an absence of correlation between the selected parameters.

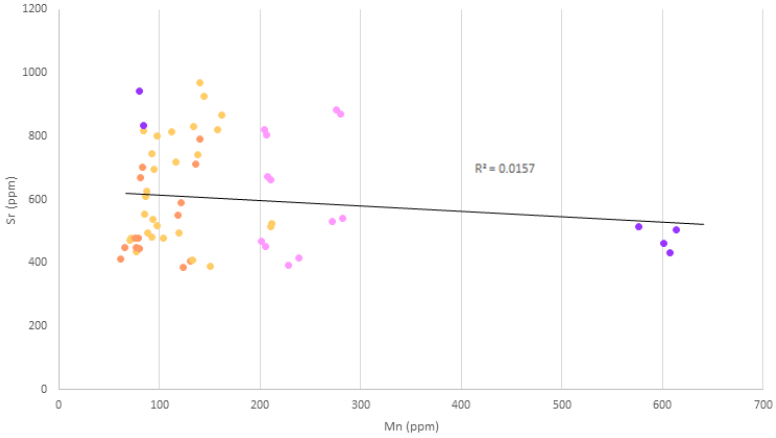

Figure 5.22. Cross-plot of Mn against Sr in ppm for the entire studied succession.

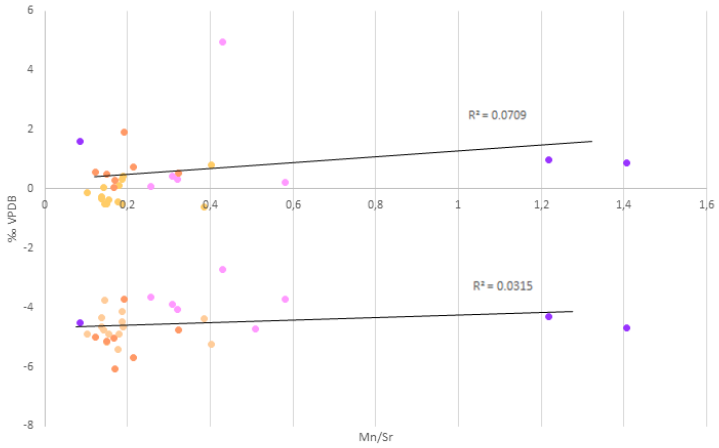

Figure 5.23. Cross-plot of Mn/Sr in ppm against both $\delta^{13}C$ (upper curve) and $\delta^{18}O$ (lower curve) for the entire studied succession.

6. Discussion

In this section, we will discuss the following topics: 1) the preservation of the primary isotopic signal, 2) the analysis and comparison of our newly high resolution $\delta^{13}C$ and $\delta^{18}O$ curves and 3) the post-Hirnantian glaciation in the context of a far-field record such as the Anticosti succession.

6.1 Primary signal preservation

Several components were analysed to show that both stable isotopes record a pristine signal ($\delta^{13}C$) and near-pristine signal ($\delta^{18}O$). First, the composition of the studied carbonate succession is a micrite-dominated matrix which was sampled for the geochemical analysis. The micrite-dominated matrix is composed of dense crystalline calcite and is negligibly dolomitized as shown on the different plates of photomicrographs, core and field pictures (Figs.5.1-5.11). Second, there are no evidence of aggrading neomorphic fabrics like microspar and neomorphic spar (James and Jones, 2016). Third, all thin sections were stained with Alizarin Red S and Potassium Ferrycianide to determine the content of calcite (pink) versus dolomite (blue). All thin sections stained pink suggesting little or no burial diagenesis affecting the succession (Dickson, 1966). Lastly, a subset of the $\delta^{13}C$ and $\delta^{18}O$ samples were analysed for trace metal geochemistry. We

looked at the Mn and Sr in particular. If there are any signs of covariance between these two elements, it would be attributed to diagenesis. But, as seen on Fig. 5.22, there is a lack of correlation between Mn and Sr values as shown by a R^2 value of 0.0157. It is the same with the Mn/Sr and $\delta^{13}C/\delta^{18}O$ cross-plot (Fig. 5.23) where the R^2 values are respectively 0.0709 and 0.0315. In addition, a strong correlation between $\delta^{13}C$ and $\delta^{18}O$ values is usually seen as a sign of diagenesis alteration in shallow neritic carbonates (Fig. 5.21; (Lohmann 1988; Marshall 1992).

In addition, the original sedimentary fabrics are well preserved as shown by the superb sedimentary structures and sparse bioturbation seen in the field and core samples. The material for all major fossil groups is also well preserved (Copper and Jin, 2014, Copper et al., 2012 and Delabroye et al., 2011). Furthermore, our $\delta^{13}C$ isotopic curve (Fig. 5.19) has similar geochemical patterns than older published low-resolution brachiopod $\delta^{13}C$ curves (Long, 1993; Brenchley et al., 1994, 2003; Bergström et al., 2006). Two major positive excursions are seen in our curve (Fig. 5.19) amongst many others which are similar to previously published curves ranging from the End-Ordovician to Early Silurian successions from numerous paleocontinents (Brenchley et al., 2003; Calner, 2008; Bergström et al., 2009; Cramer et al, 2011; Melchin et al., 2013; Mauviel and Desrochers, 2016).

In summary, the field, petrographic, and geochemical attributes of the studied succession suggest that the $\delta^{13}C$ signal recorded is pristine and well preserved. This conclusion also applies to $\delta^{18}O$ signal in spite of a noisier recorded signal than the $\delta^{13}C$ signal.

6.2 Lower Silurian Anticosti $\delta^{13}C$ signal

The Ordovician and Silurian $\delta^{13}C$ signals have been recorded worldwide creating multiple curves and displaying several positive excursions that can be used as stratigraphic tools to correlate numerous succession (Brenchley et al., 2003; Calner, 2008; Kaljo et al., 2008; Bergström et al., 2009; Bergström et al., 2011; Cramer et al., 2011; Melchin et al.,

2013, Mauviel and Desrochers, 2016). In the scope of the present study, two main isotopic carbon excursions will be discussed here: i) the Hirnantian Isotopic Carbon Excursion (HICE) and the Lower Aeronian Isotopic Carbon Excursion (Lower AICE). These excursions recorded in the Anticosti succession will be compared to the global Ordovician and Silurian isotopic carbon curves as illustrated in Figs. 6.1 and 6.2 respectively (Bergström et al., 2009; Cramer et al., 2011).

The global Ordovician isotopic carbon curve has been divided into isotopic stage slices (Bergstrom et al., 2009; Fig. 6.1). On this curve, the Hirnantian time interval is divided into two stage slices; the Hi1 and Hi2. The Hi1 stage extends from the base of the *Normalograptus extraordinarius* Graptolite Zone to the end of the global Hirnantian $\delta^{13}C$ excursion (HICE) during the early part of the *N. persculptus* Graptolite Zone (Bergstrom et al. (2009). This stage includes the lower and middle Hirnantian Stage and the lower and middle Gamachian Stage in North America. The Hi2 stage extends from the end of the Hirnantian $\delta^{13}C$ excursion (HICE) to the top of the Ordovician (base of the *Akidograptus ascensus* Graptolite Zone). This stage slice represents the upper part of the Hirnantian Stage and probably corresponds to the middle and upper parts of the *N. persculptus* Graptolite Zone as well as the upper part of the Gamachian Stage in North America. Recent high-resolution $\delta^{13}C$ curve from Anticosti (Mauviel and Desrochers, 2016; this study) captured both lower and an upper positive Hirnantian Isotope Carbon Excursion (HICE). The lower HICE corresponds to the isotopic Hi1 stage slice of Bergstrom et al. (2009). The ascending limb of the lower HICE starting from baseline values of +0.5‰ corresponds to the upper 20 m of the late Katian Vauréal Formation, $\delta^{13}C$ peak values of +2.5‰ occur in the Lower to Middle Hirnantian part of the Ellis Bay Formation. In spite of a $\delta^{13}C$ record segmented by a few stratigraphic hiatuses, the upper HICE, with its peak values of +5‰, is well recorded in the upper part of the Ellis Bay Formation. When compared with sections from around the globe, our $\delta^{13}C$ curve displays a distinct long-term trend with a long sustained lower HICE followed abruptly by the upper HICE and return to baseline values of +0.5‰ prior to the Rhuddanian. The continued descending isotopic trend well into the Becscie Formation suggests that the O–S boundary may occur at a higher stratigraphic level (up to 30 m) than previously interpreted. This descending isotopic trend corresponds to the isotopic Hi2 stage slice as originally defined by Bergstrom et al. (2009).

Relevant to the present discussion, the global Early Silurian isotopic carbon curve has been divided into five isotopic stage slices: the Rhuddanian Rh1, Rh2, and Rh3 stage slices and the Aeronian Ae1 and Ae2 stage slices (Cramer et al., 2011; Fig. 6.2). The Rh1 stage slice extends from the base of the Silurian and roughly covers the lower half of the Rhuddanian Stage. The end of the Hirnantian $\delta^{13}C$ excursion is well within the Hirnantian and baseline values persist throughout this stage slice. The Rh2 stage slice is covering the middle of the Rhuddanian Stage. A distinct negative excursion near the top of this stage slice is known from the eastern Baltic but the global presence and precise chronostratigraphic position of this excursion has not been demonstrated. This negative excursion may correspond to one of two weak negative excursions present in this interval in Arctic Canada (Melchin & Holmden 2006) but it has yet to be studied in detail elsewhere. The Rh3 stage slice represents the upper part of the Rhuddanian Stage. The Ae1 stage slice roughly corresponds to the lower third of the Aeronian Stage. There is a positive $\delta^{13}C$carb excursion recorded in strata from this interval in the East Baltic (Poldvere 2003), which was also observed in lower Aeronian strata from Arctic Canada by Melchin & Holmden (2006), but this has yet to be recognized elsewhere. The Ae2 stage slice is non-excursion or 'baseline' $\delta^{13}C$ values. The Rh stage slices, defined by Cramer et al. (2011) can be recognized in our new high-resolution $\delta^{13}C$ curve. Following the declining limb of the Upper HICE, the $\delta^{13}C$ signal returns to its pre-Hirnantian baseline values around –0.5‰ from 125 to 225 m in Fig. 5.16. This corresponds to the Rh1 stage slice (Cramer et al. (2011). A small negative excursion is present around 200 m but its global significance has not yet been demonstrated. The distinct negative carbon excursion (~-1‰) associated with the Rh2 stage slice (Cramer et al. 2011) is recorded at 100 m in Fig. 5.16. The Rh3 and Ae1 stage slices correspond to the rising limb and peak values associated with a positive isotopic carbon excursion (called Lower Aeronian on Fig. 5.16) present in the Merrimack and basal Gun River formations. The return to non-excursion or 'baseline' $\delta^{13}C$ values or the Ae2 stage slice have not been documented in our study.

In summary, the stage slices of the global Ordovician and Silurian isotopic carbon curves (Bergström et al., 2009; Cramer et al., 2011) are commonly recognized in our high resolution $\delta^{13}C$ curve (Fig. 6.3). The high-resolution nature of our dataset, however, should be help to fine-tune such global curves, especially the Hirnantian segment.

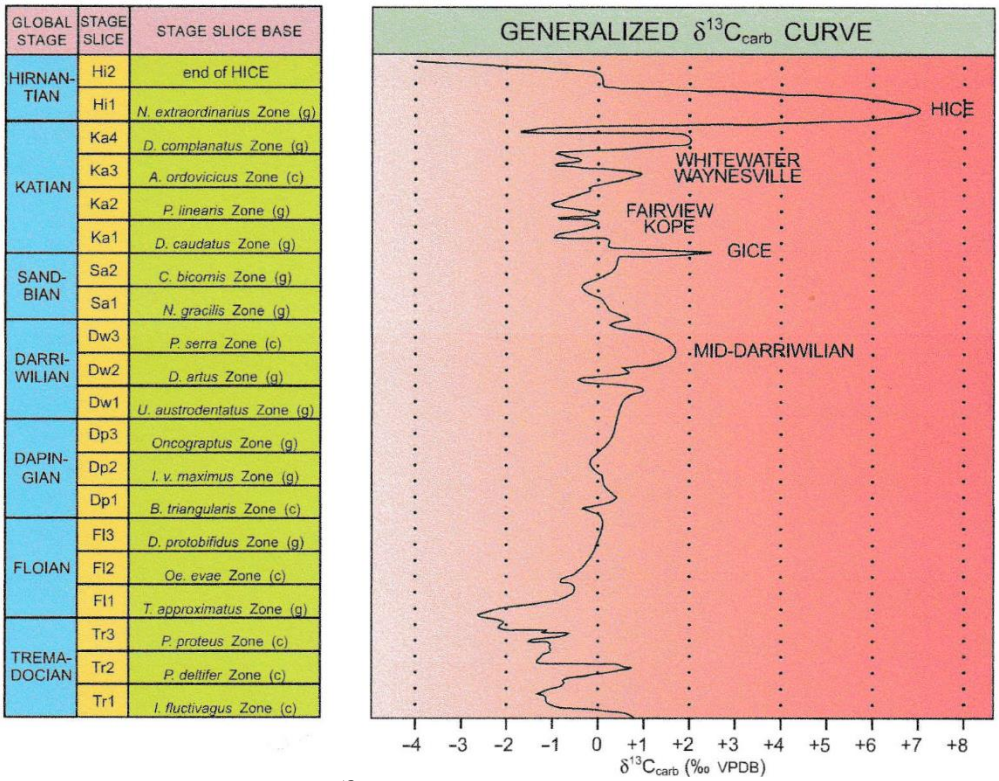

Figure 6.1. General Ordovician $\delta^{13}C$ curve (Bergström et al., 2009).

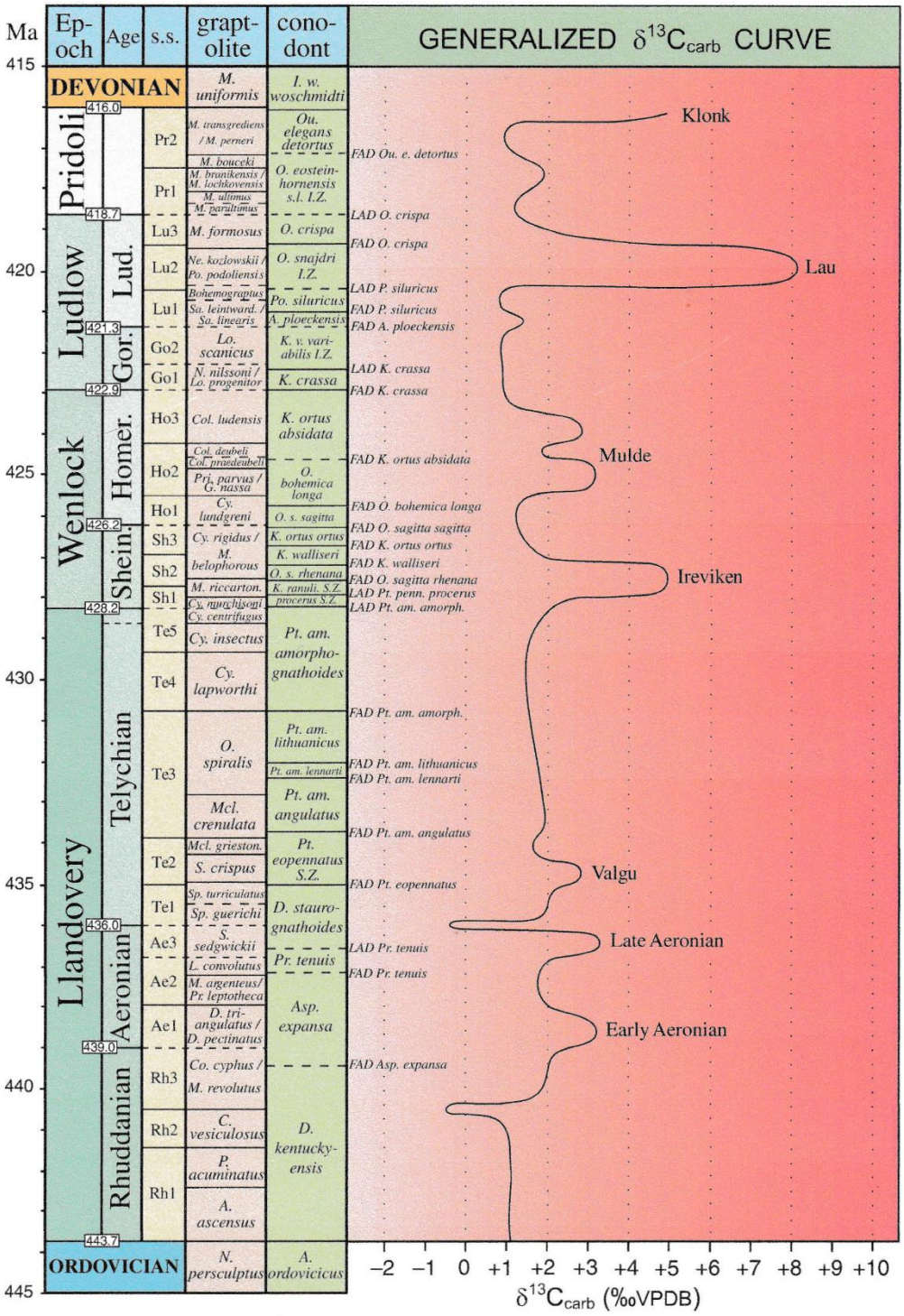

Figure 6.2. General Silurian $\delta^{13}C$ curve (Cramer et al., 2011).

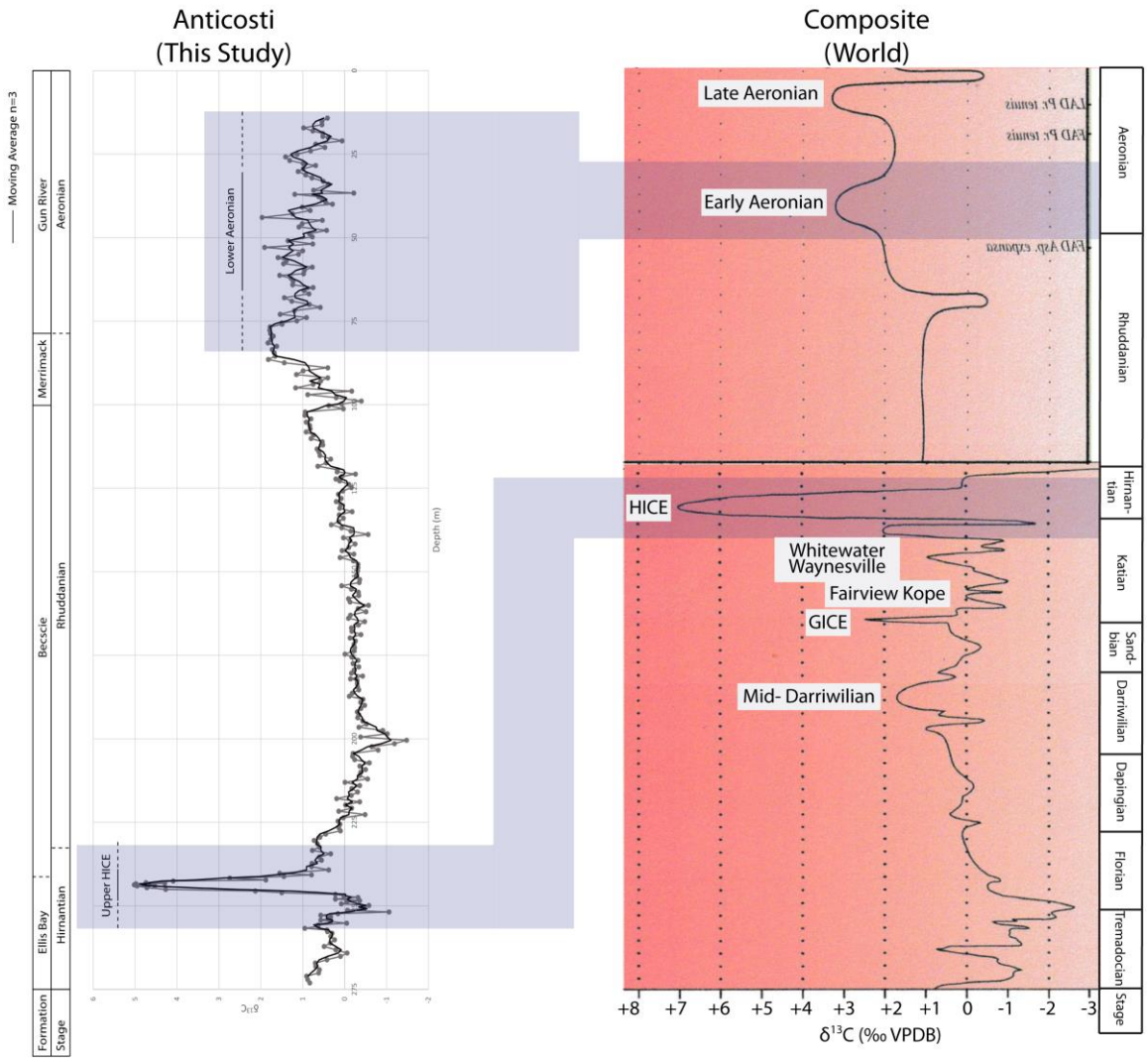

Figure 6.3. Local $\delta^{13}C$ curve (left curve) against the composite world curve (Modified from Cramer et al., 2011). Both curves have the upper HICE in common as shown in blue.

6.3 Lower Silurian Anticosti $\delta^{18}O$ signal

The secular variations of the $\delta^{18}O$ signal in deep geological time have been a subject of discussion because this signal measured from either fossil or bulk-rock material can be more easily modified by diagenesis than the $\delta^{13}C$ (Munnecke et al., 2010). Our diagenetic screening, however, suggests that the $\delta^{18}O$ signal of the Anticosti succession is little or not affected by diagenesis; thus this signal is nearly pristine (see section 6.1). Several $\delta^{18}O$ curves have been published for the upper Katian, Hirnantian and earliest Rhuddanian parts of the Anticosti succession (Long, 1993; Brenchley, 1994; Carden, 1995; Munnecke et al.,

2010; Melchin et al., 2013; Mauviel and Desrochers, 2016). Our $\delta^{18}O$ curve, however, is the first high-resolution study to cover the whole Rhuddanian and early Aeronian parts of the Anticosti succession. The global Ordovician and Silurian $\delta^{18}O$ curves (Munnecke et al., 2010) are illustrated in Figs. 6.4. and 6.5 (Munnecke et al., 2010). Our $\delta^{18}O$ curve when put against the world composite $\delta^{18}O$ curve (Munnecke et al., 2010) shows some similarities (Fig. 6.6). One of the well-recorded Paleozoic $\delta^{18}O$ event is the latest Ordovician oxygen acme (Bond et Grasby, 2017), which shows an increase from roughly -5‰ in the pre-Hirnantian to -3‰ in the Hirnantian before returning to pre-shift values at the end of the Rhuddanian. This latest Ordovician oxygen acme event of not more than a million years duration has been recognized in samples from Estonia, Sweden, North America and Argentina, and coincides with the glacial Hirnantian climax (Brenchley et al., 1995; Marshall et al., 1997). Our high resolution $\delta^{18}O$ curve (Fig. 5.17), based on well-preserved micrite samples, perfectly displays the overall long-term decline in $\delta^{18}O$ values following the Hirnantian peak between 60 and 260 m in the La Loutre #1 core. A minor positive oxygen isotope in the early Aeronian (see Fig. 6.4 from Munnecke et al., 2010; Fig. 6.6) is also present in our dataset. Higher frequency variations in our $\delta^{18}O$ signal will be separately discussed below.

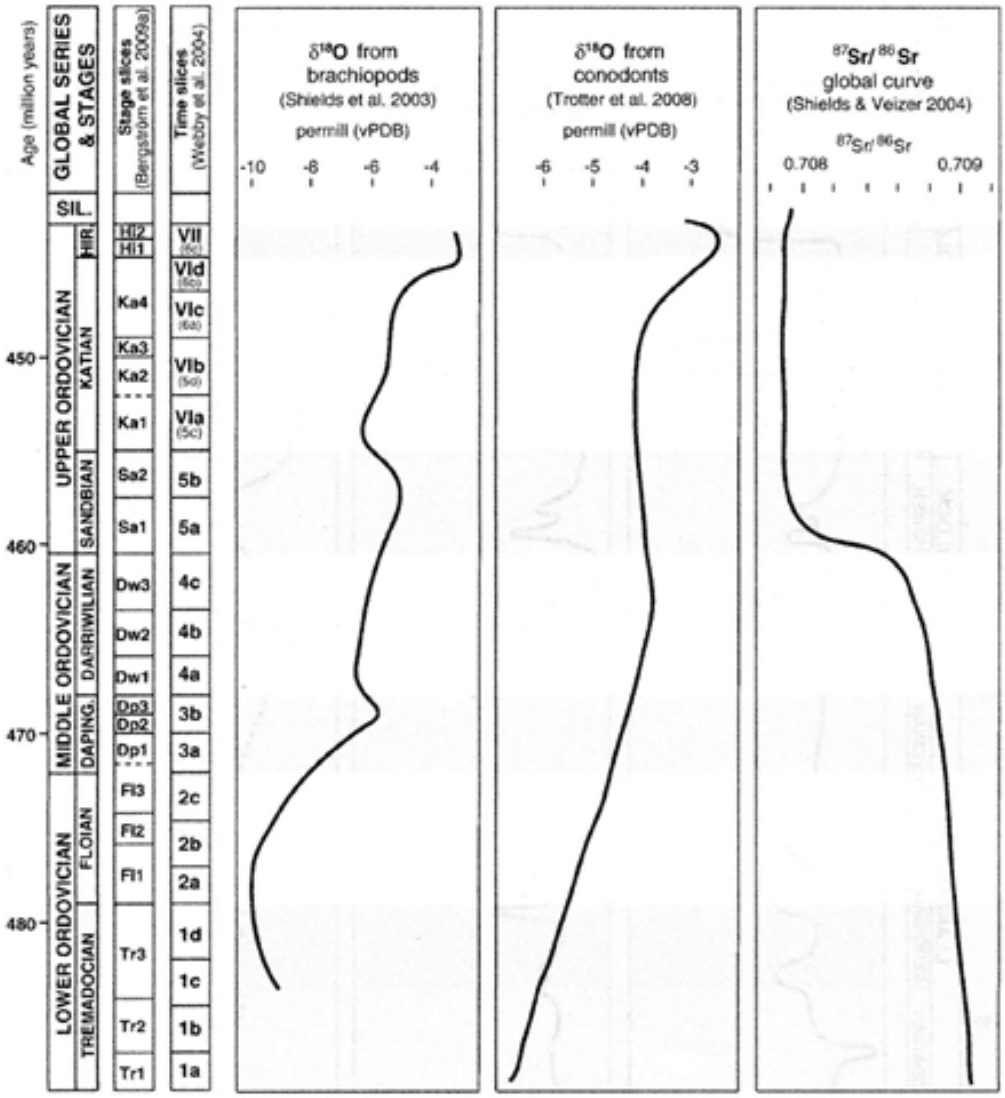

Figure 6.4. General $\delta^{18}O$ curves from brachiopod calcite and conodont apatite for the Ordovician modified from Munnecke et al. (2010).

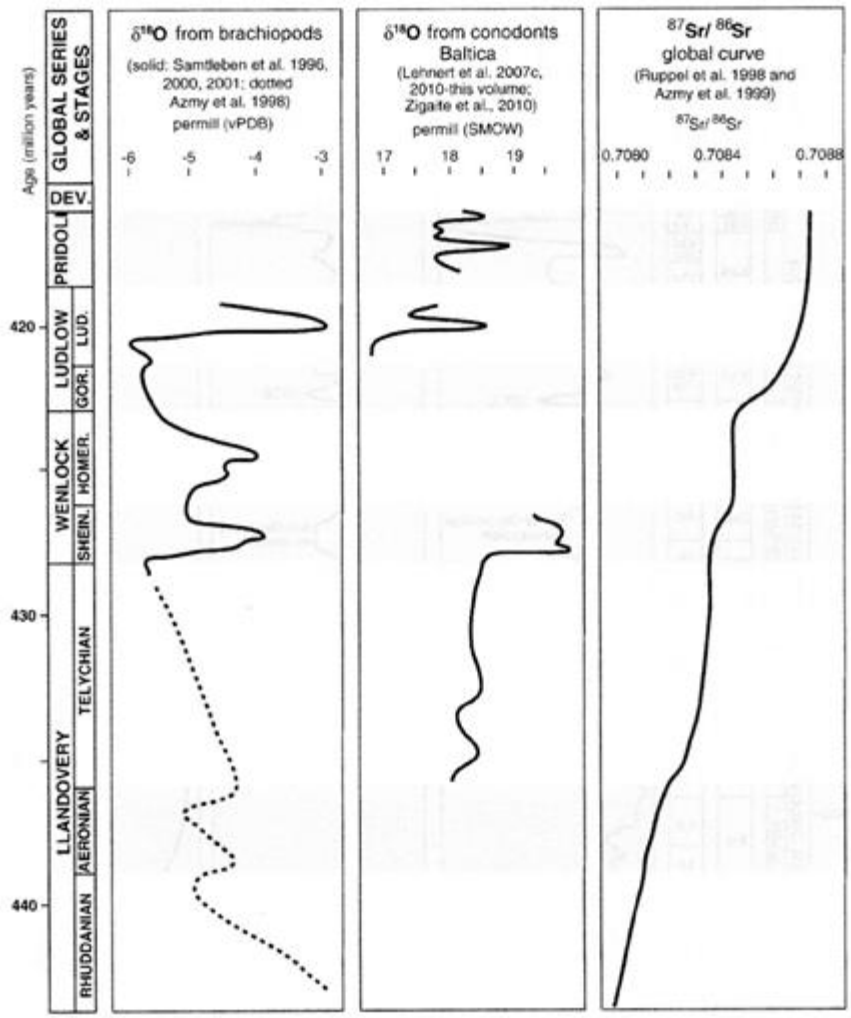

Figure 6.5. General $\delta^{18}O$ curves from brachiopod calcite and conodont apatite for the Silurian modified from Munnecke et al. (2010).

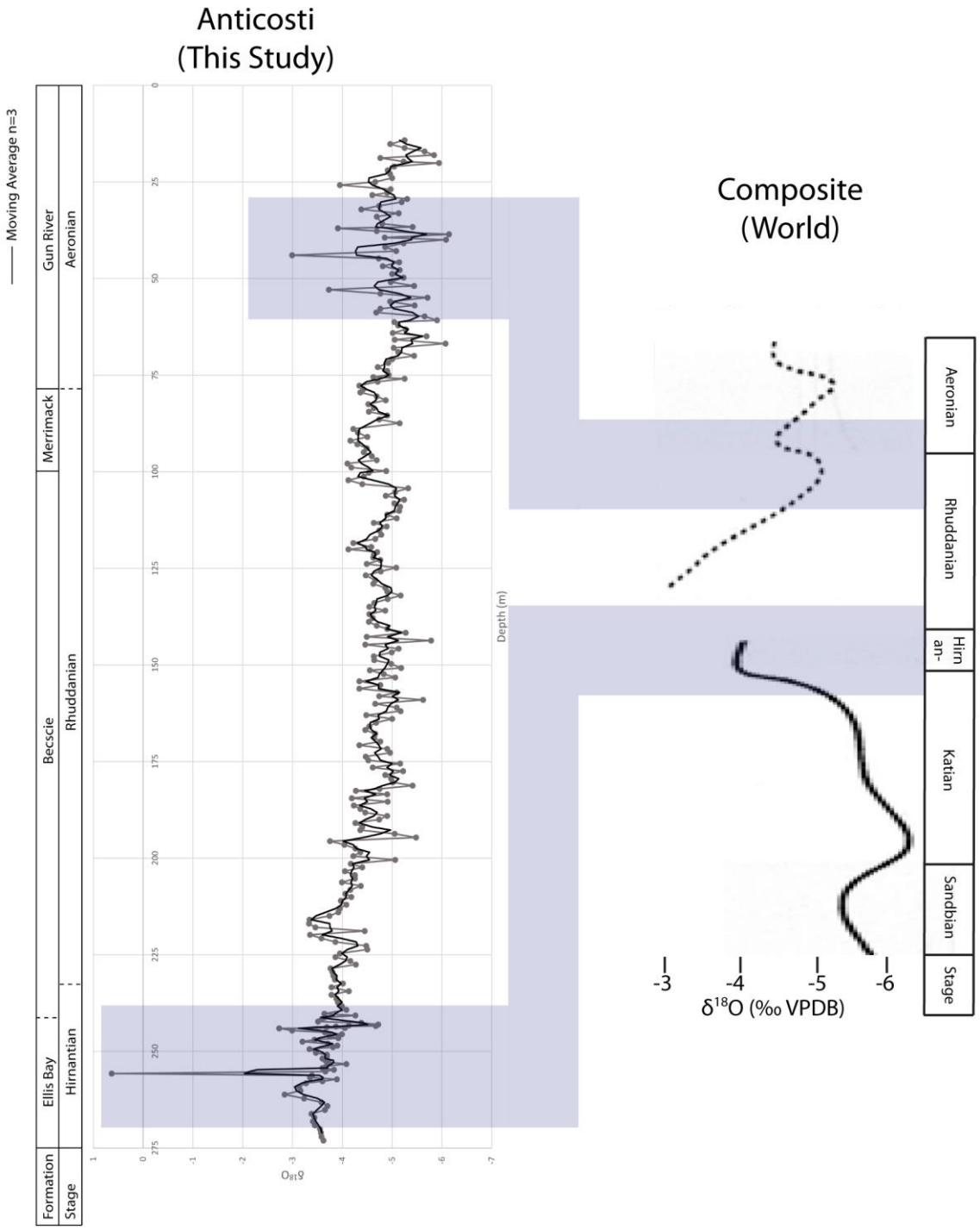

Figure 6.6. Our $\delta^{18}O$ curve against the composite world curve (Modified from Munnecke et al., 2010). Both curves have main positive excursions in common as shown in blue.

6.4 A Rhuddanian Glacio-eustatic Signal

In this section, we discuss the short-term variations present in our $\delta^{18}O$ signal (Fig. 5.20) in association with both metre- and decametre-scale TR cycles (see above). Our new

Late Hirnantian-Early Aeronian $\delta^{18}O$ curve (Fig. 5.20) rectifies some problems with the previously published curves. This curve was constructed from continuous subsurface data and a high-resolution sample interval. Our studied succession is significantly thicker than age equivalent sections from Estonia, Sweden, North America and Argentina (Munnecke et al., 2010). Calcitic lime mud was the primary inorganic marine calcium carbonate precipitate at the time of the deposition; a time of calcite sea (Stanley and Hardie 1998). Changes in $\delta^{18}O$ values from well-preserved micrite samples are, however, not easy to interpret since they usually indicate a combination of changes in temperature, salinity, and ice volume (Elrick et al., 2013). During time of glaciation, isotopic values within a given cycle are expected to be at their lowest at, or near, the deeper water facies while their highest values are at, or near, the shallowest water facies, caused by preferential evaporation and stocking of the lighter ^{16}O in growing ice sheets at higher latitudes. The long-term $\delta^{18}O$ changes of the entire succession (Fig. 5.20) support a protracted deglaciation event following the Hirnantian glacial maxima (see section above). The superimposed higher frequency variations in our $\delta^{18}O$ signal (Fig. 5.20) suggest that distinct glacial-interglacial episodes were still present during the Early Silurian. The relationship between the Lower Silurian Anticosti $\delta^{18}O$ signal and the imbricated metre- and decametre-scale stratigraphic cycles is far from perfect; some cycles correspond well with the oxygen curve while others do not. The nature of the signal is chaotic to make significant correlations and the sample resolution is too small to properly capture the smaller metre-scale TR cycles. Local environmental factors could also contribute to the background noise of our data, complicating interpretation at that level. $\delta^{18}O$ variations in metre-scale TR cycles are typically around 0.5‰–1‰ within the entire studied succession. The $\delta^{18}O$ variations in decametre-scale TR cycles, however, appear to correlate better than those at the metre-scale. Within a given decametre-scale TR cycles, $\delta^{18}O$ values are rapidly decreasing in their thinner TST portions while the $\delta^{18}O$ values are slowly increasing in their thickest RST portions. $\delta^{18}O$ variations in decametre-scale cycles are similar in scale to those present in the metre-scale cycles (i.e. 0.5‰–1‰). Thus, the frequency and amplitude $\delta^{18}O$ variations within the metre- and decametre-scale cycles show a striking similitude with those seen in astronomically tuned, glacioeustatic influenced $\delta^{18}O$ curves during the Pleistocene (Lisiecki and Raymo, 2005).

In summary, our $\delta^{18}O$ data (Fig. 5.20) are in accordance with sea-level reconstructions based on our sedimentological and stratigraphic interpretation and support our hypothesis that glacio-eustasy was the dominant control on water-depth changes during the Early Silurian on shallow water tropical carbonate platforms. Our data show a two tier stratigraphic framework with imbricated meter-scale and multi-metre-decameter cycles. We cautiously interpret based on the age of the studied formations (Copper & Jin, 2014) that the decameter-scale cycles likely represent a 100 ka eccentricity signal whereas the smaller meter-scale are a mixed obliquity and precession signal. A time-series analysis performed on the older Vaureal and Ellis Bay formations indicates that their architecture is largely controlled by Milankovitch-related climate drivers (Sinnesael et al., 2016). Several Llandovery glacial deposits are known from the South American Gondwana (Munnecke et al., 2010), but interestingly none has been yet reported from the Rhuddanian.

7. Conclusions

This study represents the first high resolution continuous chemostratigraphic data set of Lower Silurian paleotropical neritic carbonates from the subsurface of Anticosti Island, Eastern Canada. Two distinct positive carbon isotope excursions are present in the late Hirnantian part of the Ellis Bay Formation (+5‰) and in the lower Aeronian part of the Gun River Formation (+2‰). These positive isotopic carbon excursions provide a distinctive chemostratigraphic signature for regional and global correlations with other O/S sections.

In total, eight storm-influenced carbonate ramp facies in the upper Ellis Bay, Becscie, Merrimack and lower Gun River formations were recognized and organized into a multi-order stratigraphic cycles. Like the Quaternary $\delta^{18}O$ marine signal, our $\delta^{18}O$ record (Fig. 5.20) is largely coupled with multi-order cyclic facies changes. This study demonstrates the importance of glacio-eustasy following the End-Ordovician glacial maxima as one of the primary factors controlling the stratigraphic architecture of paleotropical neritic carbonates during the Early Silurian.

References

Achab, A., and Paris, F., 2007. The Ordovician chitinozoan biodiversification and its leading factors. Palaeogeography, Palaeoclimatology, Palaeoecology, **245**, p. 5–19.

Achab, A., Asselin, E., Desrochers, A., Riva, J.F., and Farley, C. 2011. Chitinozoan biostratigraphy of a new Upper Ordovician stratigraphic framework for Anticosti Island, Canada. Geological Society of America Bulletin, **123**, p. 186-205.

Achab, A., Asselin, E., Desrochers, A and Riva, J., F. 2012. The end-Ordovician chitinozoan zones of Anticosti Island, Québec: Definition and stratigraphic position, Review of Palaeobotany and Palynology, p. 1-18. http://dx.doi.org/10.1016/j.revpalbo.2012.07.019.

Achab, A., Asselin, E., Desrochers, A., and Riva, J.F. 2013. The end-Ordovician chitinozoan zones of Anticosti Island, Québec: Definition and stratigraphic position. Review of Palaeobotany and Palynology, **198**, p. 92-109.

Aigner, T. 1985. Dynamic stratigraphy of the Upper Muschelkalk, South-German Basin. Sedimentary and evolutionary cycles, Springer, p. 324-346.

Allen, J.S., Thomas, W.A., and Lavoie, D. 2009. Stratigraphy and structure of the Laurentian rifted margin in the northern Appalachians: A low-angle detachment rift system. The Geological Society of America, **37**, p. 335-338.

Azmy, K., Veizer, J., Bassett, M.G., and Copper, P. 1998. Oxygen and carbon isotopic composition of Silurian brachiopods: Implication for coeval seawater and glaciations. Geological Society of America Bulletin, **110**, p. 1499-1512.

Bassetti, M.A., Jouet, G., Dufois, F., Berné, S., Rabineau, M., and Taviani, M. 2006. Sand bodies at the shelf edge in the Gulf of Lions (Western Mediterranean): Deglacial history and modern processes. **234**, p. 93–109.

Bergström, S.M., Saltzman, M.M., and Schmitz, B. 2006. First record of the Hirnantian (Upper Ordovician) $\delta^{13}C$ excursion in the North American Midcontinent and its regional implications. Geological Magazine, **143**, p. 657-678.

Bergström, S.M., Xu, C., Gutiérrez-Marco, J.C., and Dronov, A. 2009. The new

chronostratigraphic classification of the Ordovician System and its relations to major regional series and stages and to $\delta^{13}C$ chemostratigraphy. Lethaia, **42**, p. 97-107.

Bergström, S.M., Kleffner, M., Schmitz, B., and Cramer, B.D. 2011. Revision of the position of the Ordovician-Silurian boundary in southern Ontario: regional chronostratigraphic implications of $\delta^{13}C$ chemostratigraphy of the Manitoulin Formation and associated strata. Canadian Journal of Earth Sciences, **48**, p. 1447-1470.

Bond, D., P., G., and Grasby, S., E. 2017. On the causes of mass extinctions. Palaeogeography, Palaeoclimatology, Palaeoecology **478**, p. 3–29.

Brenchley, P.J., Marshall, J.D., Carden, G.A.F., Robertson, D.B.R., Long, D.G.F., Meidla, T., Hints, L., and Anderson, T.F. 1994. Bathymetric and isotopic evidence for a short-lived Late Ordovician glaciation in a greenhouse period. Geology, **22**, p. 295-298.

Brenchley, P.J., Carden, G.A., Hints, L., Kaljo, D., Marshall, J.D., Martma, T., Meidla, T., and Nõlvak, J. 2003. High-resolution stable isotope stratigraphy of the Upper Ordovician sequences: Constraints on the timing of bioevents and environmental changes associated with mass extinction and glaciation. Geological Society of America Bulletin, **115**, p. 89-104.

Calner, M. 2008. Silurian global events – at the tipping point of climate change. In: Ashraf M.T. Elewa (ed.): *Mass extinctions,* p. 21-58. Springer-Verlag. Berlin and Heidelberg.

Carden, G. A. F. 1995. Stable isotopic changes across the Ordovician-Silurian boundary. Unpublished Ph.D. thesis, University of Liverpool, UK.

Cocks, L., R., M. and Torsvik, T., H., 2004. Earth geography from 400 to 250 Ma: a paleomagnetic, faunal and facies review. Journal of the geological society, **161**, p. 555-572.

Copper, P. and Long, D., G., F. 1989. Stratigraphic revisions for a key Ordovician Silurian boundary section, Anticosti-Island, Canada. Newsletters on stratigraphy, vol. **21**, iss: 1, p. 59-73.

Copper, P., Long, D., G., F. and Jin, J., 2012. The Early Silurian Gun River Formation of

Anticosti Island, eastern Canada: A key section for the mid-Llandovery of North America. Newsletters on Stratigraphy, **45**, p. 263-280.

Copper, P., Jin, J. and Desrochers, A., 2013. The Ordovician-Silurian boundary (late Katian-Hirnantian) of western Anticosti Island: revised stratigraphy and benthic megafaunal correlations. Stratigraphy, vol. **10**, no. 4, p. 1-15.

Copper, P., and Jin, J., 2014. The revised Lower Silurian (Rhuddanian) Becscie Formation, Anticosti Island, eastern Canada records the tropical marine faunal recovery from the end-Ordovician Mass Extinction. Newsletters on Stratigraphy, **47**, p. 61-83.

Copper, P. and Jin, J., 2015. Tracking the early Silurian post-extinction faunal recovery in the Jupiter Formation of Anticosti Island, eastern Canada: A stratigraphic revision. Newsletters on Stratigraphy, **48**, p. 221-240.

Cramer, B.D. & Saltzman, M.R. 2005: Sequestration of 12C in the deep ocean during the early Wenlock (Silurian) positive carbon isotope excursion. Palaeogeography, Palaeoclimatology, Palaeoecology **219**, p. 333–349.

Cramer, B.D., Brett, C.E., Melchin, M.J., Männik, P., Kleffner, M.A., McLaughlin, P.I., Loydell, D.K., Munnecke, A., Jeppsson, L., Corradini, C., Brunton, F.R. & Saltzman, M.R. 2011: Revised correlation of Silurian Provincial Series of North America with global and regional chronostratigraphic units and d13Ccarb chemostratigraphy. Lethaia, Vol. **44**, p. 185–202.

Delabroye, A., Munnecke, A., Vecoli, M., Copper, P., Tribovillard, N., Joachimski, M.M., Desrochers, A., and Servais, T. 2011. Phytoplankton dynamics across the Ordovician/Silurian boundary at low palaeolatitudes: Correlations with carbon isotopic and glacial events. Palaeogeography, Palaeoclimatology, Palaeoecology, **312**, p. 79-97.

Desrochers, A., James, N. P., 1988. Early Paleozoic surface and subsurface paleokarst: Middle Ordovician Carbonates, Mingan Islands, Quebec. In: James, N. P. and Choquette, P. W. (eds). Paleokarst, Springer-Verlag, New York, p. 183–210.

Desrochers, A., 2006. Rocky shoreline deposits in the Lower Silurian (upper Llandovery, Telychian) Chicotte Formation, Anticosti Island, Québec. Canadian Journal of Earth Sciences, **43**, p. 1205–1214.

Desrochers, A., Farley, C., Achab, A. & Asselin, E. 2008. A high-resolution stratigraphic model to resolve the longstanding issues relative to the correlation and interpretation of the O/S boundary on Anticosti Island. In Palaeozoic Climates, Abstracts (Kröger, B. & Servais, T., eds), p. 32A. International Congress, August 22-31, 2008, Lille, France.

Desrochers, A., Gauthier, É.L., 2009. Carte géologique de l'île d'Anticosti (1/250 000). Ministère des Ressources naturelles et de la Faune du Québec, DV 2009-03.

Desrochers, A., Farley, C., Achab, A., Asselin, E., and Riva, J.F., 2010. A far field record of the end Ordovician glaciation: The Ellis Bay Formation, Anticosti Island, Eastern Canada. Palaeogeography, Palaeoclimatology, Palaeoecology, **296**, p. 248-263.

Dickson, J.A.D. 1966. Carbonate identification and genesis as revealed by staining. Journal of Sedimentary Petrology, **36**, p. 491–505.

Díaz-Martínez, E. and Grahn, Y. 2007. Early Silurian glaciation along the western margin of Gondwana (Peru, Bolivia and northern Argentina): palaeogeographic and geodynamic setting. Palaeogeography, Palaeoclimatology, Palaeoecology, **245**, p. 62-81.

Dumas, S., and Arnott, R.W.C. 2006. Origin of hummocky and swaley cross stratification – The controlling influence of unidirectional current strength and aggradation rate. Geology, **34**, p. 1073-1076.

Embry, A. 2009. Crockerland - The source area for the Triassic to Middle Jurassic strata of the northern Axel Heiberg Island, Canadian Arctic Islands. Canadian Petroleum Geology Bulletin, **57**, p. 129-140.

Elrick, M., Reardon D., Labor, W., Martin, J., Desrochers. A., and Pope, M. 2013. Orbital-scale climate change and glacioeustasy during the early Late Ordovician (pre Hirnantian) determined from δ18O values in marine apatite. Geology, **41**, p. 775-778.

Farley, C. 2008. Sediment dynamics and stratigraphic architecture of a mixed carbonate-siliciclastic ramp: the Upper Ordovician (Hirnantian) Ellis Bay Formation, Anticosti Island, Québec, Canada. University of Ottawa, Unpublished M.Sc. thesis.

Ghienne, J.F., Desrochers, A., Vandenbroucke, T.R.A., Achab, A., Asselin, E., Dabard,

M.P., Farley, C., Loi, A., Paris, F., Wickson, S., and Veizer, J. 2014. A Cenozoic-style scenario for the end-Ordovician glaciation. Nature Communications, 5:4485. doi:10.1038/ncomms5485.

Ghienne, J., F., Moreau, J., Degermann, L., and Rubino, J., L., 2015. Lower Paleozoic unconformities in an intracratonic platform setting: glacial erosion versus tectonics in the eastern Murzuq Basin (southern Libya). International Journal of Earth Sciences: Geologische Rundschau, **102**, p. 455-482.

Grahn, Y. and Caputo, M. V. 1992. Early Silurian glaciations in Brazil. Palaeogeography, Palaeoclimatology, Palaeoecology, **99**, p. 9-15.

Hambrey, M.J. 1984. The Late Ordovician-Early Silurian glacial period. Palaeogeography, Palaeoclimatology, Palaeoecology, **51**, p. 273-289.

Harper, D., A., T., Hammarlund, E., U., Rasmussen, C., M., Ø., 2014. End Ordovician extinctions: A coincidence of causes. Gondwana Research, **25**, p. 1294-1307.

Herrmann, A.D., Haupt, B.J., Patzkowski, M.E., Seidov, D., Slingerland, R.L., 2004b. Response of Late Ordovician paleoceanography to changes in sea level, continental drift, and atmospheric pCO2: potential causes for long-term cooling and glaciation. Palaeogeography, Palaeoclimatology, Palaeoecology, **210**, p. 385–401.

James, N.P., Desrochers, A., and Kyser, T.K. 2015. Polygenetic (Polyphase) Karsted Hardground Omission Surfaces in Lower Silurian Neritic Limestones: Anticosti Island, Eastern Canada. Journal of Sedimentary Research, **85,** p. 1138–1154. doi:10.2110/jsr.2015.71.

James, N. and Jones, B 2016. Origin of carbonate sedimentary rocks. In: Wiley (ed.), p. 278-281. AGU: American Geophysical Union.

Jeppsson, L., 1990. An oceanic model for lithological and faunal changes tested on the Silurian record. Journal of the Geological Society, London **147**, p. 663–674.

Jin, J., Harper, D.A.T., Cocks, L.R.M., McCausland, P.J.A., Rasmussen, C.M.Ø. and Sheehan, P.M. 2013. Precisely locating the Ordovician equator in Laurentia. Geology, **41**, p. 107–110.

Jones, D.S., Fike, D.A., Finnegan, S., Fischer, W.W., Schrag, D.P., and McCay, D.

2011. Terminal Ordovician carbon isotope stratigraphy and glacioeustatic sea-level change across Anticosti Island (Québec, Canada). Geological Society of America Bulletin, **123** p. 1645-1664.

Kaljo, D., Martma, T., Männik, P., Viira, V., 2003. Implications of Gondwana glaciations in the Baltic late Ordovician and Silurian and a carbon isotopic test of environmental cyclicity. Bulletin de la Société géologique de France **174**, p. 59–66.

Kaljo, D., Hints, L., Männik, P., and Nõlvak, J. 2008. The succesion of Hirnation events based on data from Baltica: brachiopods, chitinozoans, conodonts, and carbon isotopes. Estonian Journal of Earth Sciences, **57**, p. 197-218.

Lavoie, D., Burden, E., and Lebel, D. 2003. Stratigraphic framework for the Cambrian-Ordovician rift and passive margin successions from southern Quebec to western Newfoundland. Canadian Journal of Earth Sciences, **40**, p. 177–205.

Lavoie, D., 2008. Appalachian foreland basins of Canada. In: A.D. Miall (ed.). Sedimentary Basins of the World – USA and Canada. Elsevier Science, Ch. 3, p. 63–103.

Lisiecki, L., E., and M., E., Raymo (2005). A Pliocene-Pleistocene stack of 57 globally distributed benthic $\delta^{18}O$ records. Paleoceanography, 20, PA1003, doi: 10.1029/2004PA001071.

Lohmann, K.C. 1988. *In* Geochemical patterns of meteoric diagenetic systems and their application to studies of paleokarst, *Edited by* N.P. James and P.W. Choquette. Paleokarst: New York, Springer-Verlag, 58–80.

Long, D.G.F., and Copper, P. 1987. Stratigraphy of the Upper Ordovician upper Vauréal and Ellis Bay formations, eastern Anticosti Island, Quebec. Canadian Journal of Earth Sciences, **24**, p. 1807-1820.

Long, D.G.F., 1993. Oxygen and carbon isotopes and event stratigraphy near the Ordovician- Silurian boundary, Anticosti Island, Québec. Palaeogeography, Palaeoclimatology, Palaeoecology, **104**, p. 49-59.

Long, D.G.F. 2007. Tempestite frequency curves: a key to Late Ordovician and Early Silurian subsidence, sea-level change, and orbital forcing in the Anticosti foreland basin, Québec, Canada. Canadian Journal of Earth Sciences, **44**, p. 412-431.

Loydell, D., K. 2007. Early Silurian positive $\delta^{13}C$ excursions and their relationship to glaciations, sea-level changes and extinction events. Geological Journal, **42**, p. 531–546.

Macmahan, J.H., Thornton, E.B., and Reniers, A.J.H.M. 2006. Rip current review. **53** p. 191–208.

Marshall, J.D. 1992. Climatic and oceanographic isotopic signals from the carbonate rock recordand their preservation. Geological Magazine, **129**, 143–160.

Mauviel, A. 2016 Integrated high-resolution chemostratigraphic and cyclostratigraphic analysis of paleotropical carbonates spanning the Ordovician-Silurian boundary at the west-end of Anticosti Island, eastern Canada. University of Ottawa, Unpublished M.Sc. thesis.

Mauviel, A., and Desrochers, A. 2016. A high resolution, continuous $\delta^{13}C$ record spanning the O/S boundary on Anticosti Island, eastern Canada. Canadian Journal of Earth Sciences.

McLaughlin, P.I., and Brett, C.E., 2007. Signatures of sea-level rise on the carbonate margin of a Late Ordovician foreland basin: A case study from the Cincinnati Arch, USA. Palaios, **22**, p. 245-267

Melchin, M.J. and Holmden, C., 2006b, Carbon isotope chemostratigraphy of the Llandovery in Arctic Canada: Implications for global correlation and sea level change: GFF, v. **128**, p. 173–180.

Melchin, M.J. 2008. Restudy of some Ordovician-Silurian boundary graptolites from Anticosti Island, Canada, and their biostratigraphic significance. Lethaia, **41**, p. 155–162.

Melchin, M.J., Sadler, P.M., and Cramer, B.D. 2012. The Silurian Period. *In* The Geologic Time Scale 2012. *Edited by* F.M. Gradstein, J.G. Ogg, M. Schmitz and G. Ogg. Elsevier B.V. p. 525-558.

Melchin, M.J., Mitchell, C.E., Holmden, C., and Štorch, P. 2013. Environmental changes in the Late Ordovician-early Silurian: Review and new insights from black shales and nitrogen isotopes. Geological Society of America Bulletin, **125**: 1635-1670.

Munnecke, A., Samtleben, C., and Bickert, T. 2003. The Ireviken Event in the lower Silurian of Gotland , Sweden relation to similar Palaeozoic and Proterozoic events.

195. doi:10.1016/S0031-0182(03)00304-3.

Munnecke, A., Calner, M., Harper, D.A.T., and Servais, T. 2010. Ordovician and Silurian seawater chemistry, sea level, and climate: A synopsis. Palaeogeography, Palaeoclimatology, Palaeoecology, **296**, p. 389-413.

Ogg et al., 2016 Silurian 425.6. 2016. doi:10.1016/B978-0-444-59467-9.00007-8.

Pinet, N., Keating, P., Lavoie, D., Dietrich, J., Duchesne, M., Brake, V., 2012. Revisiting the Appalachian structural front and offshore Anticosti Basin (northern Gulf of St. Lawrence, Canada) by integrating old and new geophysical datasets. Marine and petroleum geology, **32**, p. 50-62.

Põldvere, A. 2003. General geological setting and stratigraphy. In Ruhnu (500) Drill Core (Põldvere, A., ed.), Estonian Geological Sections, 5, 6–12.

Robardet, M. and Doré, F. 1988. The Late Ordovician diamictic formations from Southwestern Europe: North-Gondwana glaciomarine deposits. Palaeogeography, Palaeoclimatology, Palaeoecology, **66**, p. 19-31.

Saltzman, M.R., 2001. Silurian δ13C stratigraphy: a view from North America. Geology **29**, p. 671–674.

Sami, T., and Desrochers, A. 1992. Episodic sedimentation an early Silurian, storm-dominated carbonate ramp, Becscie and Merrimack formations, Anticosti Island, Canada. Sedimentology, **39**, p. 355-381.

Samtleben, C., Munnecke, A., Bickert, T., Pätzold, J., 1996. The Silurian of Gotland (Sweden): facies interpretation based on stable isotopes in brachiopod shells. Geologische Rundschau, **85**, p. 278–292.

Sinnesael, M., Desrochers, A., McLaughlin, P., Mauviel, A., Vandenbroucke, T.R.A., and Claeys, P., 2016. Proceedings of the final IGCP 591 Annual Meeting, Ghent, Belgium. Program with abstracts.

Shields, G.A., Carden, G.A., Veizer, J., Meidla, T., Rong, J.-Y., and Li, R.-Y. 2003. Sr, C, and O isotope geochemistry of Ordovician brachiopods: a major isotopic event around the Middle-Late Ordovician transition. Geochimica et Cosmochimica Acta, **67**, p. 2005-2025.

Sloss, L.L. 1963. Sequences in the cratonic interior of North America. Bulletin of the Geological Society of America, **74**, p. 93–114.

Soufiane, A., Achab, A., 2000. Chitinozoan Zonation of the Late Ordovician and the Early Silurian of the Island of Anticosti, Québec, Canada. Review of Palaeobotany and Palynology, **109**, p. 85-111.

Stanley, S.T., and Hardie, L.A. 1998. Secular oscillations in the carbonate mineralogy of Reef building and sediment-producing organisms driven by tectonically forced shifts in seawater chemistry. Palaeogeography, Palaeoclimatology, Palaeoecology, **144**, p. 3-19.

Trotter, J.A., Williams, I.S., Barnes, C.R., Lécuyer, C., Nicoll, R.S., 2008. Did cooling oceans trigger Ordovician biodiversification? Evidence from conodont thermometry. Science **321**, p. 550–554.

Zazoun, R., S. and Mahdjoub, Y. 2011. Strain analysis of Late-Ordovician tectonic events in the In-Tahouite and Tamadjert Formations (Tassili-n-Ajjers area, Algeria). Journal of African earth sciences, **60**, p. 63-78.

Zhang, S., Barnes, C.R., 2002. Late Ordovician – Early Silurian (Ashgillian – Llandovery) Sea Level Curve Derived from Conodont Community Analysis, Anticosti Island, Québec. Palaeogeography, Palaeoclimatology, Palaeoecology, **180**, p. 5-32.

Zhang, S., Barnes, C.R., 2004. Conodont bio-events, cladistics and response to glacio-eustasy, Ordovician-Silurian boundary through Llandovery, Anticosti Basin, Québec Palaeogeography, Palaeoclimatology, Palaeoecology, **180**, p. 5-32.

Appendices

Appendix 1. Aerial photo (Google Map) showing the key stratigraphic surfaces (MRZ in red, MFZ in blue) associated with the meter-scale stratigraphic cycles in the Lower Becscie Formation, Baie des Nabots.

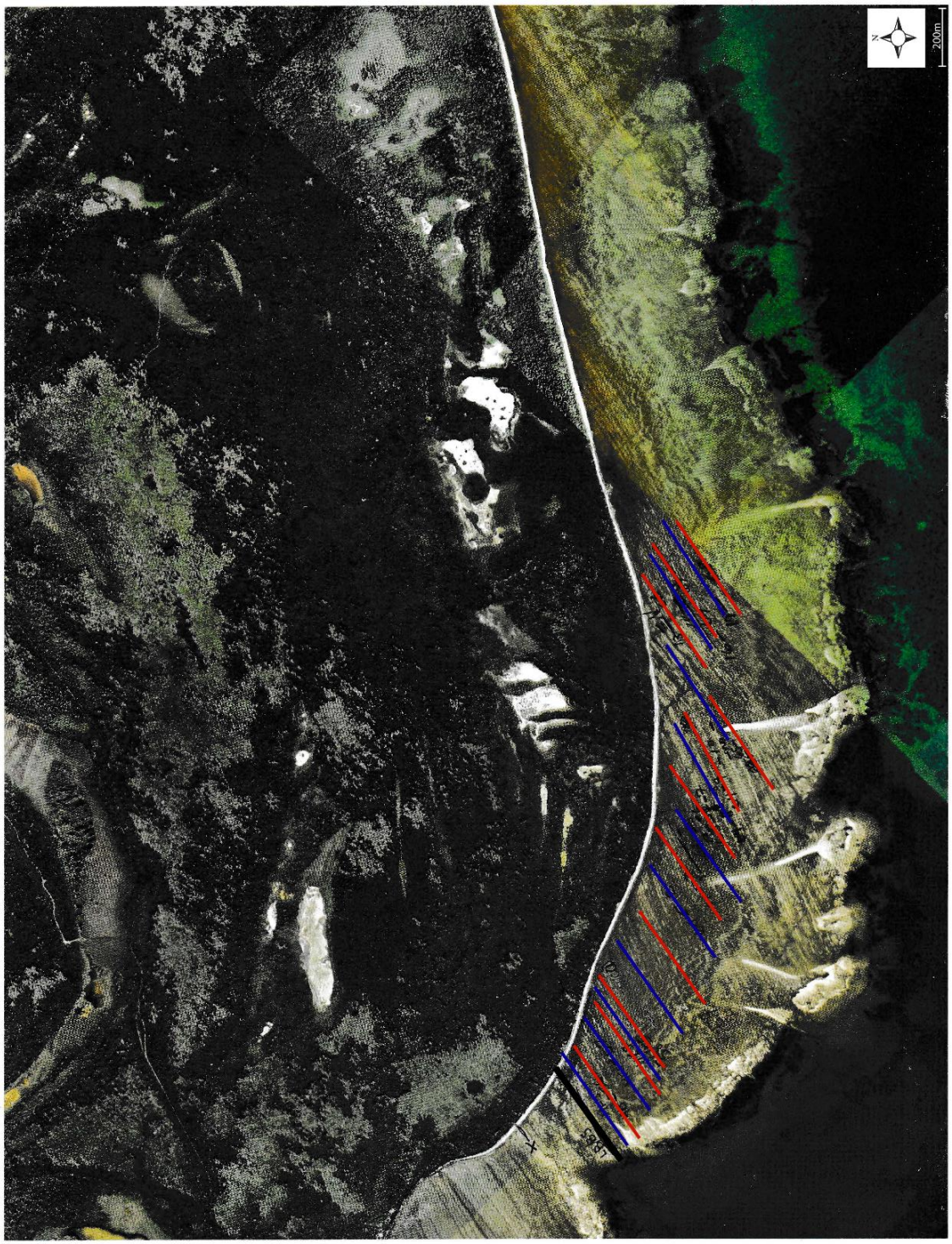

Appendix 2. Aerial photo (Google Map) showing the key stratigraphic surfaces (MRZ in red, MFZ in blue) associated with the meter-scale stratigraphic cycles in the middle Becscie Formation, Baie des Sarcelles.

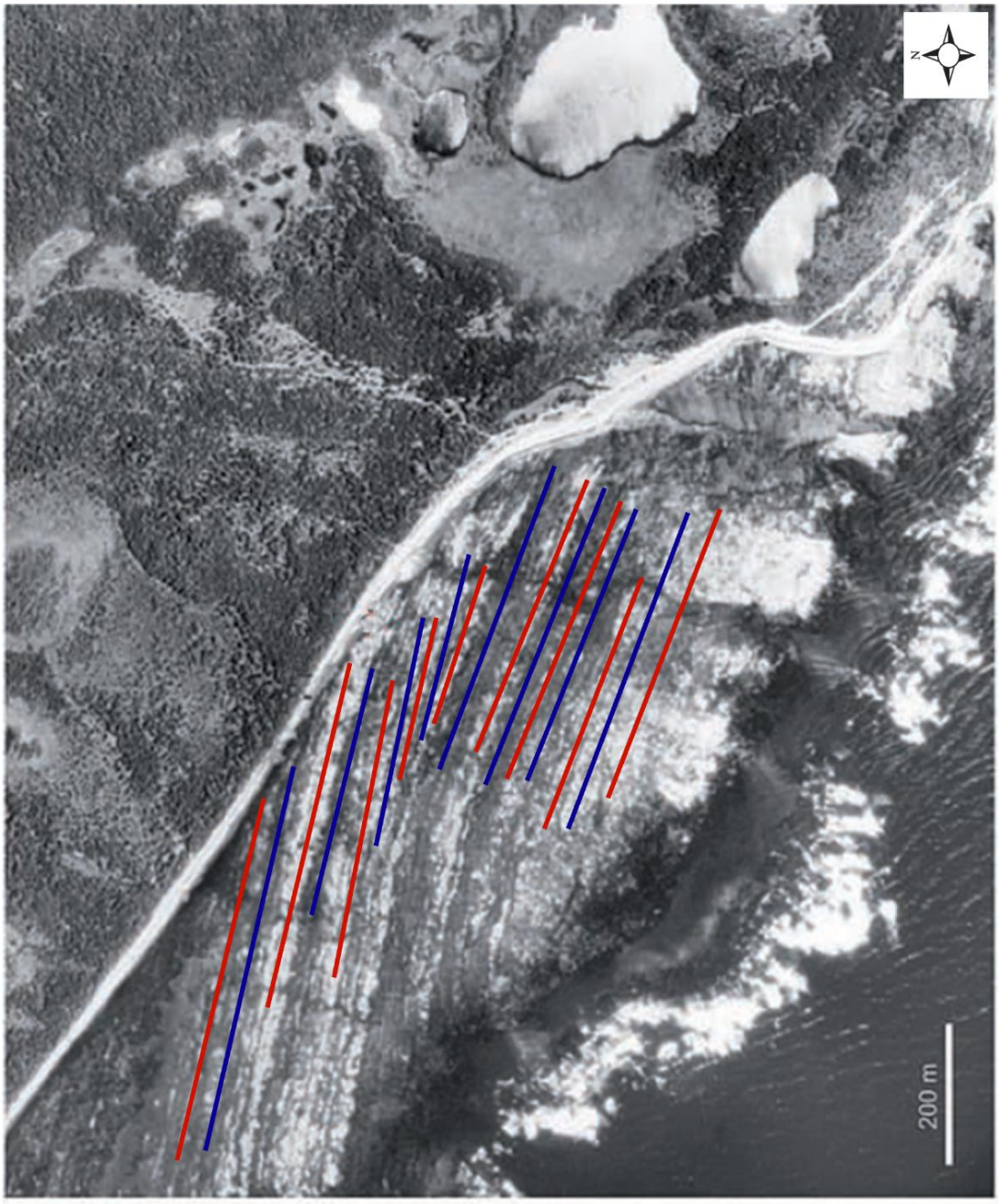

Appendix 3. Aerial photo (Google Map) showing the key stratigraphic surfaces (MRZ in red, MFZ in blue) associated with the meter-scale stratigraphic cycles in the upper Becscie Formation, east of the mouth of the Becscie River.

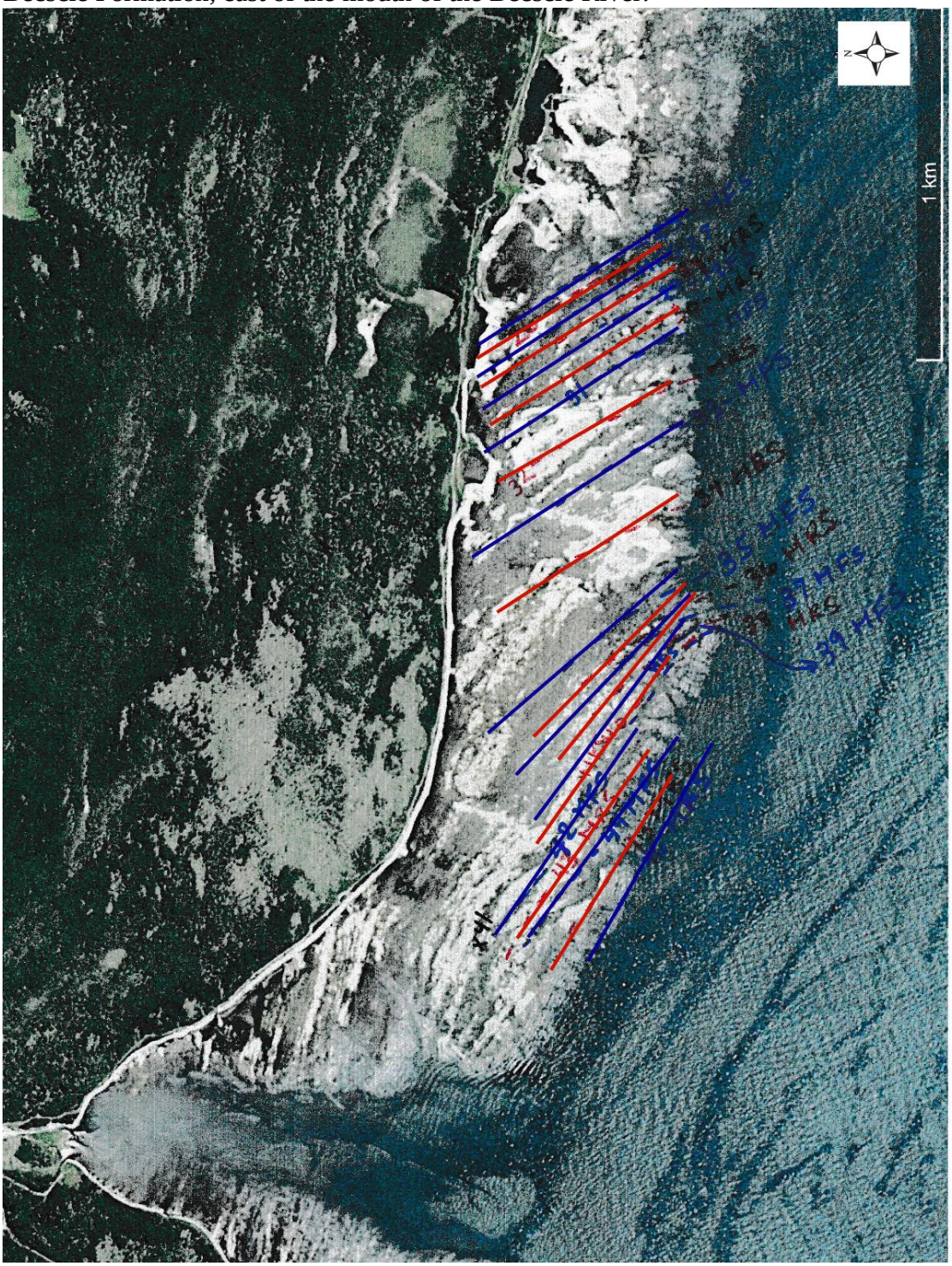

Appendix 4. Aerial photo (Google Map) showing the poorly exposed recessive Merrimack Formation at the mouth of the rivière Ste-Marie.

Appendix 5. Paleocurrent measurements in the Lower Becscie Formation.

N	Facies	Structure	Direction	Location
1	Facies 3	Symmetrical ripple	120	Baie des Nabots
2	Facies 3	Symmetrical ripple	110	Baie des Nabots
3	Facies 3	Symmetrical ripple	100	Baie des Nabots
4	Facies 3	Symmetrical ripple	110	Baie des Nabots
5	Facies 3	Channel	200	Baie des Nabots
6	Facies 3	Channel	200	Baie des Nabots
7	Facies 3	Symmetrical ripple	100	Baie des Nabots
8	Facies 3	Channel	200	Baie des Nabots
9	Facies 3	Symmetrical ripple	100	Baie des Nabots

Appendix 6. Paleocurrent measurements in the Middle Becscie Formation.

N	Facies	Structure	Direction	Location
1	Facies 5	Channel	210	Baie des Sarcelles
2	Facies 5	Channel	215	Baie des Sarcelles
3	Facies 5	Channel	220	Baie des Sarcelles
4	Facies 5	Channel	210	Baie des Sarcelles
5	Facies 5	Channel	200	Baie des Sarcelles
6	Facies 5	Channel	205	Baie des Sarcelles
7	Facies 5	Channel	205	Baie des Sarcelles
8	Facies 5	Channel	180	Baie des Sarcelles
9	Facies 5	Channel	200	Baie des Sarcelles
10	Facies 5	Channel	200	Baie des Sarcelles
11	Facies 5	Channel	205	Baie des Sarcelles
12	Facies 5	Channel	205	Baie des Sarcelles
13	Facies 5	Channel	210	Baie des Sarcelles
14	Facies 3	Symmetrical ripple	110	Baie des Sarcelles
15	Facies 3	Symmetrical ripple	110	Baie des Sarcelles
16	Facies 5	Channel	195	Baie des Sarcelles
17	Facies 3	Symmetrical ripple	115	Baie des Sarcelles
18	Facies 3	Symmetrical ripple	110	Baie des Sarcelles
19	Facies 5	Channel	200	Baie des Sarcelles
20	Facies 5	Channel	200	Baie des Sarcelles
21	Facies 5	Channel	210	Baie des Sarcelles
22	Facies 5	Channel	200	Baie des Sarcelles
23	Facies 5	Channel	205	Baie des Sarcelles
24	Facies 5	Channel	210	Baie des Sarcelles
25	Facies 5	asymmetrical ripple	190	Baie des Sarcelles
26	Facies 6	Wave-ripple	20	Baie des Sarcelles
27	Facies 6	Wave-ripple	30	Baie des Sarcelles
28	Facies 6	Wave-ripple	30	Baie des Sarcelles
29	Facies 6	Wave-ripple	25	Baie des Sarcelles
30	Facies 6	Wave-ripple	25	Baie des Sarcelles
31	Facies 6	Wave-ripple	20	Baie des Sarcelles
32	Facies 6	Wave-ripple	30	Baie des Sarcelles

Appendix 7. Paleocurrent measurements in the Upper Becscie Formation.

N	Facies	Structure	Direction	Location
1	Facies 3	Symmetrical ripple	100	Ste-Marie
2	Facies 3	Symmetrical ripple	110	Ste-Marie
3	Facies 5	Asymmetrical ripple	200	Ste-Marie
4	Facies 3	Symmetrical ripple	100	Ste-Marie
5	Facies 5	Asymmetrical ripple	200	Ste-Marie
6	Facies 5	Channel	200	Ste-Marie
7	Facies 5	Channel	200	Ste-Marie
8	Facies 5	Asymmetrical ripple	200	Ste-Marie
9	Facies 5	Channel	200	Ste-Marie
10	Facies 3	Symmetrical ripple	100	Ste-Marie
11	Facies 5	Asymmetrical ripple	200	Ste-Marie
12	Facies 3	Symmetrical ripple	100	Ste-Marie
13	Facies 3	Symmetrical ripple	100	Ste-Marie
14	Facies 5	Symmetrical ripple	100	Ste-Marie
15	Facies 5	Symmetrical ripple	100	Ste-Marie
16	Facies 3	Asymmetrical ripple	200	Ste-Marie
17	Facies 3	Symmetrical ripple	100	Ste-Marie
18	Facies 5	Symmetrical ripple	100	Ste-Marie
19	Facies 5	Channel	200	Ste-Marie
20	Facies 5	Channel	200	Ste-Marie
21	Facies 5	Channel	200	Ste-Marie
22	Facies 3	Asymmetrical ripple	210	Ste-Marie
23	Facies 5	dunes sym	100	Ste-Marie
24	Facies 5	Channel	200	Ste-Marie
25	Facies 5	Channel	205	Ste-Marie
26	Facies 5	Channel	200	Ste-Marie
27	Facies 5	Channel	200	Ste-Marie
28	Facies 5	Channel	200	Ste-Marie
29	Facies 5	Channel	200	Ste-Marie

Appendix 8. Stable Isotope Geochemistry of the Ellis Bay Formation

# Sample	Depth (m)	# Box	Formation	Weight (mg)	$\delta^{13}C$ (‰)	$\delta^{18}O$ (‰)
196	273.07	92	Ellis Bay	0.68	0.83	-3.62
197	272.08	92	Ellis Bay	0.69	0.88	-3.58
198	271.07	92	Ellis Bay	0.6	0.91	-3.57
199	270.11	91	Ellis Bay	0.58	0.62	-3.55
200	269.12	91	Ellis Bay	0.55	0.6	-3.45
201	268.11	91	Ellis Bay	0.58	0.69	-3.41
202	267.12	90	Ellis Bay	0.67	0.7	-3.44
203	266.16	90	Ellis Bay	0.68	0.42	-3.38
204	265.15	90	Ellis Bay	0.65	0.1	-3.65
205	264.14	89	Ellis Bay	0.55	-0.06	-3.7
206	263.18	89	Ellis Bay	0.66	0.21	-3.58
207	262.18	89	Ellis Bay	0.65	0.49	-3.23
208	261.17	88	Ellis Bay	0.68	0.34	-2.84
209	260.16	88	Ellis Bay	0.55	0.24	-3.16
210	259.17	88	Ellis Bay	0.48	0.33	-3.13
211	258.22	88	Ellis Bay	0.5	0.3	-3.27
212	257.73	87	Ellis Bay	0.66	0.41	-3.6
213	257.22	87	Ellis Bay	0.65	0.42	-3.89
214	256.73	87	Ellis Bay	0.65	0.95	-3.35
215	256.23	87	Ellis Bay	0.66	0.63	-3.39
216	255.74	87	Ellis Bay	0.67	0.63	0.63
217	255.22	87	Ellis Bay	0.55	-0.05	-3.66
218	254.76	86	Ellis Bay	0.64	0.33	-3.83
219	254.28	86	Ellis Bay	0.63	0.57	-3.6
220	253.82	86	Ellis Bay	0.69	0.39	-3.68
221	253.30	86	Ellis Bay	0.51	0.33	-4.08
222	252.81	86	Ellis Bay	0.66	0.57	-3.72
223	252.35	86	Ellis Bay	0.63	0.16	-3.66
224	251.84	85	Ellis Bay	0.61	-1.06	-3.6
225	251.36	85	Ellis Bay	0.48	-0.07	-3.69
226	250.86	85	Ellis Bay	0.61	-0.47	-3.69
227	250.36	85	Ellis Bay	0.53	-0.46	-3.47
228	249.88	85	Ellis Bay	0.53	-0.58	-3.46
229	249.42	85	Ellis Bay	0.66	0.08	-3.34
230	248.92	85	Ellis Bay	0.55	-0.05	-3.81
231	248.48	84	Ellis Bay	0.61	-0.36	-3.9
232	248.00	84	Ellis Bay	0.64	0.22	-3.71
233	247.48	84	Ellis Bay	0.6	-0.32	-3.2
234	247.01	84	Ellis Bay	0.63	0.02	-3.44
235	246.57	84	Ellis Bay	0.66	0.22	-3.92
236	246.07	84	Ellis Bay	0.68	1.5	-3.74
237	245.57	83	Ellis Bay	0.52	2.13	-3.99

238	245.09	83	Ellis Bay	0.58	4.27	-3.65
239	244.57	83	Ellis Bay	0.59	4.72	-2.99
240	244.02	83	Ellis Bay	0.6	4.95	-2.73
241	243.92	83	Ellis Bay	0.53	4.53	-4.05
242	243.72	82	Ellis Bay	0.66	5.02	-3.69
243	243.57	82	Ellis Bay	0.63	4.65	-3.87
244	243.42	82	Ellis Bay	0.47	4.98	-4.67
245	243.27	82	Ellis Bay	0.49	4.29	-4.13
246	243.07	82	Ellis Bay	0.65	4.74	-4.72
247	242.60	82	Ellis Bay	0.49	4.09	-4.38
248	242.27	81	Ellis Bay	0.6	1.88	-3.51
249	241.70	81	Ellis Bay	0.5	2.74	-3.58

Appendix 9. Stable Isotope Geochemistry of the Becscie Formation

# Sample	Depth (m)	# Box	Formation	Weight (mg)	$\delta^{13}C$ (‰)	$\delta^{18}O$ (‰)
250	241.22	81	Becscie	0.61	1.45	-3.64
251	240.72	81	Becscie	0.53	0.79	-4.26
252	240.25	81	Becscie	0.63	1.55	-3.64
253	239.25	80	Becscie	0.55	0.38	-4.08
254	238.26	80	Becscie	0.53	0.79	-3.99
255	237.30	80	Becscie	0.6	0.78	-3.91
256	236.35	79	Becscie	0.54	0.55	-3.88
257	235.38	79	Becscie	0.5	0.6	-3.78
258	234.41	79	Becscie	0.64	0.33	-4.13
259	233.40	78	Becscie	0.64	0.77	-3.78
260	232.43	78	Becscie	0.54	0.6	-4.01
261	231.43	78	Becscie	0.66	0.65	-3.85
262	230.44	77	Becscie	0.64	0.73	-3.82
263	229.48	77	Becscie	0.63	0.59	-3.8
264	228.51	77	Becscie	0.6	0.45	-3.76
265	227.55	76	Becscie	0.58	0.1	-4.27
266	226.60	76	Becscie	0.64	0.14	-4.16
267	225.58	76	Becscie	0.57	0.11	-3.86
268	224.64	75	Becscie	0.68	0.16	-3.95
269	223.65	75	Becscie	0.59	0.03	-4.5
270	222.70	75	Becscie	0.55	-0.49	-4.48
271	221.69	74	Becscie	0.62	0.14	-3.86
272	220.75	74	Becscie	0.56	-0.17	-3.58
273	219.81	74	Becscie	0.64	-0.02	-3.35
274	218.86	73	Becscie	0.56	-0.36	-4.45
275	217.91	73	Becscie	0.53	0.19	-3.46
276	216.93	73	Becscie	0.7	-0.16	-3.33
277	215.93	72	Becscie	0.67	-0.31	-3.34
278	214.93	72	Becscie	0.72	-0.17	-3.74
279	213.99	72	Becscie	0.56	-0.36	-3.92
280	213.01	71	Becscie	0.56	-0.01	-3.95
281	212.04	71	Becscie	0.66	-0.55	-4.08
282	211.03	71	Becscie	0.7	-0.36	-3.97
283	210.05	70	Becscie	0.62	-0.38	-4.18
284	209.19	70	Becscie	0.64	-0.5	-4.06
285	208.19	70	Becscie	0.53	-0.36	-4.16
286	207.19	69	Becscie	0.56	-0.59	-4.37
287	206.25	69	Becscie	0.54	-0.24	-3.99
288	205.28	69	Becscie	0.52	-0.19	-4.25
289	204.38	69	Becscie	0.54	-0.2	-4.25
290	203.38	68	Becscie	0.5	-0.8	-4.05
291	202.36	68	Becscie	0.58	-0.65	-4.4

292	201.45	68	Becscie	0.56	-1.19	-4.17
293	200.45	67	Becscie	0.51	-1.48	-5.06
294	199.45	67	Becscie	0.56	-0.38	-4.22
295	198.50	66	Becscie	0.68	-1.02	-4.36
296	197.51	66	Becscie	0.49	-0.91	-4.26
297	196.54	66	Becscie	0.55	-0.34	-4.04
298	195.57	65	Becscie	0.61	-0.52	-3.75
299	194.65	65	Becscie	0.65	-0.43	-5.48
300	193.68	65	Becscie	0.6	-0.31	-5.05
301	192.73	64	Becscie	0.54	-0.34	-4.36
302	191.93	64	Becscie	0.63	-0.3	-4.4
303	190.90	64	Becscie	0.5	-0.39	-4.26
304	189.99	63	Becscie	0.5	-0.48	-4.74
305	189.08	63	Becscie	0.58	-0.38	-4.9
306	188.19	63	Becscie	0.71	-0.44	-4.46
307	187.26	63	Becscie	0.58	-0.11	-4.36
308	186.35	62	Becscie	0.49	-0.18	-4.23
309	185.38	62	Becscie	0.5	-0.34	-4.91
310	184.46	62	Becscie	0.64	-0.31	-4.19
311	183.48	61	Becscie	0.58	-0.3	-4.9
312	182.56	61	Becscie	0.49	-0.3	-4.27
313	182.06	61	Becscie	0.7	-0.14	-4.75
314	181.23	60	Becscie	0.65	-0.43	-5.41
315	180.38	60	Becscie	0.72	-0.16	-5.01
316	179.45	60	Becscie	0.61	-0.22	-4.98
317	178.47	59	Becscie	0.51	-0.34	-4.86
318	177.47	59	Becscie	0.61	-0.2	-5.22
319	176.52	59	Becscie	0.71	-0.32	-4.61
320	175.53	58	Becscie	0.66	-0.17	-5.16
321	174.66	58	Becscie	0.58	-0.01	-4.52
322	173.71	58	Becscie	0.63	-0.22	-4.47
323	172.73	57	Becscie	0.6	-0.24	-4.96
324	171.75	57	Becscie	0.54	-0.22	-4.9
325	170.75	57	Becscie	0.49	-0.26	-4.34
326	169.82	56	Becscie	0.56	-0.13	-4.76
327	168.82	56	Becscie	0.7	-0.39	-4.64
328	167.81	56	Becscie	0.64	-0.17	-4.66
329	166.82	55	Becscie	0.66	-0.16	-4.46
330	165.92	55	Becscie	0.56	-0.33	-4.54
331	164.92	55	Becscie	0.68	-0.48	-4.68
332	163.94	54	Becscie	0.68	-0.09	-5
333	162.98	54	Becscie	0.55	-0.14	-4.48
334	161.98	54	Becscie	0.53	-0.51	-5.17
335	161.03	53	Becscie	0.68	-0.32	-5.09
336	160.04	53	Becscie	0.48	-0.57	-4.66

337	159.04	53	Becscie	0.63	-0.13	-5.62
338	158.08	53	Becscie	0.7	-0.09	-4.74
339	157.10	52	Becscie	0.56	-0.34	-5.09
340	156.12	52	Becscie	0.52	-0.33	-4.34
341	155.20	52	Becscie	0.59	-0.16	-4.76
342	154.21	51	Becscie	0.6	0.07	-4.34
343	153.23	51	Becscie	0.55	-0.35	-5.06
344	152.34	51	Becscie	0.54	-0.36	-4.83
345	151.39	50	Becscie	0.69	-0.27	-4.55
346	150.80	50	Becscie	0.56	-0.29	-5.18
347	149.73	50	Becscie	0.68	-0.31	-4.98
348	148.73	49	Becscie	0.67	-0.32	-4.64
349	147.75	49	Becscie	0.55	-0.32	-4.63
350	146.76	49	Becscie	0.59	-0.21	-4.99
351	145.77	48	Becscie	0.63	0.11	-5.13
352	144.72	48	Becscie	0.5	-0.22	-4.46
353	143.69	48	Becscie	0.7	0.06	-5.78
354	142.70	47	Becscie	0.53	-0.1	-4.49
355	141.67	47	Becscie	0.56	-0.25	-5.27
356	140.66	47	Becscie	0.56	-0.13	-4.9
357	139.83	46	Becscie	0.61	0.03	-4.69
358	138.84	46	Becscie	0.64	-0.56	-4.53
359	137.84	46	Becscie	0.49	-0.15	-4.61
360	136.85	45	Becscie	0.49	0.07	-4.54
361	135.93	45	Becscie	0.56	0.32	-4.86
362	134.94	45	Becscie	0.62	0.14	-4.54
363	133.96	44	Becscie	0.58	0.03	-4.64
364	132.95	44	Becscie	0.69	0.13	-4.91
365	132.01	43	Becscie	0.62	-0.18	-5.17
366	131.01	43	Becscie	0.56	0.12	-4.9
367	130.03	43	Becscie	0.71	0.09	-4.86
368	129.00	43	Becscie	0.52	0.2	-4.62
369	128.07	42	Becscie	0.63	0.08	-4.66
370	126.82	42	Becscie	0.62	0.15	-4.47
371	125.81	42	Becscie	0.64	0.04	-4.77
372	124.82	41	Becscie	0.5	-0.16	-5.08
373	123.83	41	Becscie	0.63	-0.1	-4.49
374	122.83	41	Becscie	0.58	0.12	-4.76
375	122.23	40	Becscie	0.69	0.21	-4.62
376	121.53	40	Becscie	0.54	0.07	-4.63
377	120.78	40	Becscie	0.61	-0.26	-4.7
378	120.08	39	Becscie	0.53	0.18	-4.12
379	119.45	39	Becscie	0.58	0.17	-4.58
380	118.43	39	Becscie	0.6	0.64	-4.22
381.A	117.39	38	Becscie	0.62	0.44	-4.66

381.B	116.29	38	Becscie	0.56	0.33	-4.78
382	115.20	38	Becscie	0.54	0.59	-4.74
383	114.18	38	Becscie	0.54	0.61	-4.89
384	113.24	37	Becscie	0.62	0.66	-4.63
385	112.05	37	Becscie	0.68	0.52	-5.09
386	111.11	36	Becscie	0.63	0.53	-4.9
387	110.11	36	Becscie	0.55	0.8	-5.14
388	109.07	36	Becscie	0.61	0.74	-5.16
389	108.16	35	Becscie	0.64	0.92	-5.04
390	107.22	35	Becscie	0.64	0.82	-5.24
391	106.23	35	Becscie	0.53	0.83	-4.87
392	105.23	34	Becscie	0.53	0.92	-5.06
393	104.25	34	Becscie	0.71	0.8	-5.32
394	103.20	34	Becscie	0.68	0.95	-4.4
395	102.19	33	Becscie	0.59	0.94	-4.12
396	101.23	33	Becscie	0.69	0.03	-4.43
397	100.27	33	Becscie	0.52	0.38	-4.53
398	99.80	32	Becscie	0.65	0.07	-4.88

Appendix 10. Stable Isotope Geochemistry of the Merrimack Formation

# Sample	Depth (m)	# Box	Formation	Weight (mg)	$\delta^{13}C$ (‰)	$\delta^{18}O$ (‰)
399	98.90	32	Merrimack	0.63	-0.4	-4.18
400	97.88	32	Merrimack	0.62	0.2	-4.1
401	96.99	31	Merrimack	0.69	0.88	-4.69
402	95.95	31	Merrimack	0.57	-0.17	-4.59
403	94.94	31	Merrimack	0.57	1.17	-4.43
404	93.89	30	Merrimack	0.64	0.75	-4.49
405	92.90	30	Merrimack	0.62	0.57	-4.3
406	91.95	30	Merrimack	0.65	0.4	-4.16
407	90.97	29	Merrimack	0.59	1.15	-4.5
408	89.87	29	Merrimack	0.7	0.99	-4.31
409	88.93	29	Merrimack	0.59	0.4	-4.22
410	87.45	28	Merrimack	0.57	1.44	-5.15
411	86.45	28	Merrimack	0.58	1.82	-4.74
412	85.44	28	Merrimack	0.65	1.66	-4.9
413	84.47	27	Merrimack	0.55	1.68	-4.53
414	83.50	27	Merrimack	0.6	1.73	-4.63
415	82.50	27	Merrimack	0.5	1.62	-4.52
416	81.48	26	Merrimack	0.58	1.83	-4.87
417	80.49	26	Merrimack	0.66	1.76	-4.69
418	79.48	26	Merrimack	0.66	1.7	-4.36

Appendix 11. Stable Isotope Geochemistry of the Gun River Formation

# Sample	Depth (m)	# Box	Formation	Weight (mg)	$\delta^{13}C$ (‰)	$\delta^{18}O$ (‰)
419	78.70	25	Gun River	0.56	1.77	-4.42
420	77.71	25	Gun River	0.6	1.79	-4.34
421	76.71	25	Gun River	0.68	1.78	-4.71
422	75.91	25	Gun River	0.56	1.49	-5.25
423	75.5	24	Gun River	0.66	1.5	-4.62
424	74.9	24	Gun River	0.58	1.14	-4.93
425	73.9	23	Gun River	0.55	0.91	-4.9
426	72.93	23	Gun River	0.63	1.54	-4.71
427	71.86	23	Gun River	0.61	1.2	-4.92
428	70.86	22	Gun River	0.55	0.58	-5
429	70	22	Gun River	0.63	0.84	-5.44
430	69	22	Gun River	0.61	1.26	-5.12
431	67.95	21	Gun River	0.6	1.44	-5.03
432	66.83	21	Gun River	0.67	0.85	-6.07
433	65.83	21	Gun River	0.7	0.97	-5.05
434	64.93	20	Gun River	0.7	0.75	-5.69
435	64.09	20	Gun River	0.63	1.24	-5.01
436	63.15	20	Gun River	0.58	1.23	-5.27
437	62.15	19	Gun River	0.71	1.28	-5.12
438	61.25	19	Gun River	0.54	1.55	-5.04
439	60.8	19	Gun River	0.64	0.98	-5.9
440	59.8	19	Gun River	0.6	0.96	-5.65
441	58.8	18	Gun River	0.6	0.77	-4.68
442	57.8	18	Gun River	0.66	1.46	-4.76
443	56.95	18	Gun River	0.7	1.39	-5.45
444	55.95	17	Gun River	0.53	1.59	-4.96
445	54.95	17	Gun River	0.6	1.1	-5.71
446	53.9	16	Gun River	0.5	1	-4.76
447	52.9	16	Gun River	0.64	1.91	-3.73
448	51.9	16	Gun River	0.63	0.76	-5.44
449	50.9	15	Gun River	0.6	1.35	-4.97
450	49.75	15	Gun River	0.69	0.77	-5.23
451	48.8	15	Gun River	0.7	0.84	-5
452	47.8	14	Gun River	0.55	0.43	-5.15
453	46.8	14	Gun River	0.57	1.09	-4.81
454	45.8	14	Gun River	0.6	1.01	-5.14
455	44.8	13	Gun River	0.64	0.53	-4.73
456	43.95	13	Gun River	0.68	1.97	-2.99
457	42.9	13	Gun River	0.5	1.24	-5.08
458	41.85	12	Gun River	0.55	0.82	-4.86
459	40.85	12	Gun River	0.67	1.01	-5.23
460	39.95	12	Gun River	0.6	0.29	-6.08

461	39.4	11	Gun River	0.52	0.45	-4.85
462	38.55	11	Gun River	0.62	0.53	-6.14
463.A	37.7	11	Gun River	0.5	0.62	-4.69
463.B	37	10	Gun River	0.54	1.19	-3.91
464	36.65	10	Gun River	0.7	-0.22	-5.41
465	35.8	10	Gun River	0.63	0.74	-4.8
466	34	9	Gun River	0.54	0.39	-4.69
467	33.1	9	Gun River	0.53	0.51	-5.13
468	32.1	9	Gun River	0.58	0.78	-4.38
469	31.2	8	Gun River	0.6	0.93	-4.74
470	30.2	8	Gun River	0.66	1.11	-5.19
471	29.4	8	Gun River	0.63	0.99	-5.3
472	28.4	7	Gun River	0.59	0.69	-4.6
473	27.8	7	Gun River	0.66	0.99	-4.9
474	26.9	7	Gun River	0.57	1.31	-4.97
475	25.8	7	Gun River	0.67	1.41	-3.95
476	25	6	Gun River	0.66	1.13	-4.66
477	24	6	Gun River	0.5	0.81	-5
478	22.95	6	Gun River	0.52	0.47	-4.96
479	22	5	Gun River	0.7	0.69	-4.91
480	21	5	Gun River	0.61	0.06	-5.04
481	20.1	5	Gun River	0.68	0.39	-5.94
482	19.71	4	Gun River	0.5	0.52	-5.23
483	18.8	4	Gun River	0.54	0.52	-4.76
484	18.05	4	Gun River	0.56	0.76	-5.84
485	17.1	3	Gun River	0.69	0.98	-5.65
486	16.2	3	Gun River	0.51	0.54	-5.25
487	15.2	3	Gun River	0.64	0.54	-4.96
488	14.2	2	Gun River	0.6	0.41	-5.25

Appendix 12. Trace Element Geochemistry.

Formation	Samples	Sr	Sr (ppm)	Mn	Mn (ppm)
Ellis Bay	204 A	0.0804	803.8792714	0.0206	206.025964
Ellis Bay	213 A	0.0674	673.7476442	0.0208	207.756798
Ellis Bay	221 A	0.0870	870.446479	0.0280	280.136409
Ellis Bay	232 A	0.0394	393.6975	0.0228	228.4132
Ellis Bay	240 A	0.0468	467.7051	0.0201	201.3883
Ellis Bay	246 A	0.0532	532.3509	0.0271	271.1308
Becscie	258 A	0.0866	866.0998	0.0162	162.1199
Becscie	270 A	0.0740	740.4960	0.0138	138.3539
Becscie	286 A	0.0390	389.8457	0.0150	150.2813
Becscie	298 A	0.0968	968.0155	0.0140	139.6023
Becscie	305 A	0.0555	555.2865	0.0086	85.5480
Becscie	314 A	0.0436	436.4716	0.0077	77.2154
Becscie	325 A	0.0813	813.2217	0.0112	112.1812
Becscie	334 A	0.0473	472.7876	0.0071	70.7020
Becscie	348 A	0.0694	693.9349	0.0094	94.4038
Becscie	356 A	0.0816	815.8459	0.0084	84.2117
Becscie	366 A	0.0495	495.0600	0.0089	88.6263
Becscie	371 A	0.0609	609.3131	0.0086	86.2994
Becscie	381.B A	0.0517	516.8069	0.0098	97.9393
Becscie	390 A	0.0526	525.6032	0.0211	211.2078
Merrimack	401 A	0.0431	431.4140	0.0607	607.0209
Merrimack	408 A	0.0504	504.3742	0.0614	613.9081
Merrimack	415 A	0.0944	943.6536	0.0080	79.7731
Gun River	428 A	0.0669	669.0768	0.0081	81.4045
Gun River	434 A	0.0552	551.8758	0.0119	118.5800
Gun River	447 A	0.0713	713.4238	0.0136	135.9417
Gun River	460 A	0.0450	449.5130	0.0077	76.5947
Gun River	467 A	0.0412	411.9093	0.0062	61.7450
Gun River	480 A	0.0478	477.5043	0.0079	79.3371
Gun River	483 A	0.0404	404.3811	0.0131	130.9486
Ellis Bay	204 B	0.0820	819.5054	0.0204	203.8723
Ellis Bay	213 B	0.0662	661.9300	0.0211	210.7028
Ellis Bay	221 B	0.0883	882.5160	0.0276	275.9218
Ellis Bay	232 B	0.0415	414.6798	0.0239	238.9440
Ellis Bay	240 B	0.0451	451.1969	0.0205	205.4909
Ellis Bay	246 B	0.0539	539.4574	0.0281	281.4961
Becscie	258 B	0.0821	821.3147	0.0158	157.5505
Becscie	270 B	0.0830	830.1120	0.0134	133.5118
Becscie	286 B	0.0408	408.2309	0.0133	133.0779
Becscie	298 B	0.0925	924.6814	0.0144	144.4061
Becscie	305 B	0.0537	536.5589	0.0094	93.6497
Becscie	314 B	0.0494	493.9383	0.0119	119.2446
Becscie	325 B	0.0718	717.6239	0.0116	115.9173

Becscie	334 B	0.0479	478.6142	0.0072	71.5098
Becscie	348 B	0.0746	746.4034	0.0092	92.3164
Becscie	356 B	0.0801	801.2835	0.0098	97.5515
Becscie	366 B	0.0482	482.0917	0.0093	92.5230
Becscie	371 B	0.0625	625.2031	0.0087	86.8669
Becscie	381.B B	0.0479	479.3055	0.0104	103.7615
Becscie	390 B	0.0513	513.3584	0.0210	210.0098
Merrimack	401 B	0.0461	460.9255	0.0601	601.4635
Merrimack	408 B	0.0515	514.5700	0.0576	576.4946
Merrimack	415 B	0.0835	835.2518	0.0084	84.1154
Gun River	428 B	0.0702	702.4920	0.0083	83.3299
Gun River	434 B	0.0591	590.9843	0.0121	121.3316
Gun River	447 B	0.0792	791.6060	0.0141	140.5079
Gun River	460 B	0.0446	446.0077	0.0080	80.1898
Gun River	467 B	0.0448	447.7029	0.0065	65.4091
Gun River	480 B	0.0479	478.7675	0.0076	75.7098
Gun River	483 B	0.0387	386.9961	0.0124	123.8314